

UNIVERSITY OF OKLAHOMA

GRADUATE COLLEGE

IMPACT OF MOISTURE CHANGES IN UNSATURATED SOIL ENGINEERING APPLICATIONS

A DISSERTATION

SUBMITTED TO THE GRADUATE FACULTY

in partial fulfillment of the requirements for the

Degree of

DOCTOR OF PHILOSOPHY

By

ARASH HASSANIKHAH

Norman, Oklahoma

2016

IMPACT OF MOISTURE CHANGES IN UNSATURATED SOIL ENGINEERING APPLICATIONS

A DISSERTATION APPROVED FOR THE
SCHOOL OF CIVIL ENGINEERING AND ENVIRONMENTAL SCIENCE

BY

Dr. Gerald A. Miller, Chair

Dr. Kianoosh Hatami, Co-Chair

Dr. Kanthasamy K. Muraleetharan

Dr. Musharraf Zaman

Dr. James D. Baldwin

*Dedicated to My Beloved Wife, Maryam Varsei, and
My Adorable Son, Bornah*

Acknowledgments

I would like to express my sincere gratitude to my advisor Professor Gerald A. Miller, for his support, immense knowledge, precious guidance and his continuous encouragement.

I would like to appreciate my co-advisor Professor Kianoosh Hatami for his support and for giving me the chance to work under his supervision.

I acknowledge Professors: Dr. Musharraf Zaman, Dr. Kanthasamy K. Muraleetharan, Dr. James Baldwin and Dr. Amy B. Cerato for participating on my Ph.D. committee and for their contribution to my dissertation.

I would like to thank Mr. Michael Schmitz for his technical support and collaboration in fabrication of the desiccation box.

I am thankful to the staff members of the civil engineering department particularly Ms. Susan Williams who has always been kind and helpful.

I would also like to thank my colleagues and friends especially Dr. Rodney Collins and Dr. Danial Esmaili, for their help and support.

I am grateful to my dear mother, father and the rest of my beloved family for their constant love and encouragement to pursue my dreams.

I would like to express my gratitude to my father-in-law Dr. Ali Asghar Varsei for being such a great inspiration throughout my academic journey.

I would like to extend my most heartfelt appreciation to my wife, my best friend and my love, Maryam, for believing in me, for her love, encouragement, understanding and unconditional support.

Table of Contents

Acknowledgments	iv
Table of Contents	v
List of Tables	ix
List of Figures	x
Abstract	xv
CHAPTER 1: Introduction	1
1.1 Overview Part 1: Development and impact of desiccation cracks on unsaturated soils	1
1.2 Overview Part 2: Interface behavior between unsaturated soil and geomembranes	2
1.3 Overview Part 3: Modeling lateral load behavior of piles in unsaturated soil due to seasonal moisture content changes	3
1.4 Summary of research contributions	4
1.5 Objectives and Scopes of Research	5
1.6 Outline of dissertation	7
CHAPTER 2: Development and impact of desiccation cracks on unsaturated soils	8
2.1 Background	8
2.2 Modeling and predicting desiccation crack depth in unsaturated soil	13
2.2.1 Analytical model for predicting crack depth	13
2.2.2 Numerical model for predicting crack depth	15
2.2.3 Tensile strength of a compacted soil	17
2.2.4 Comparison of analytical and numerical results with experimental data	21
2.5 Modeling the impact of desiccation cracks on unsaturated seepage of soil layer	31
2.5.1 Modeling discrete cracks	32
2.5.2 Modeling using the equivalent hydraulic conductivity approach	37
2.5.3 Comparison of discrete crack and equivalent layer modeling results	39
2.6 Impact of desiccation cracks on unsaturated seepage and stability of slope	47
2.6.1 Site selection and soil physical properties	47
2.6.2 Mechanical and hydraulic properties of soil	47

2.6.3 Unsaturated seepage analysis considering a cracked layer	49
2.6.4 Unsaturated slope stability analysis considering a cracked layer	54
CHAPTER 3: Interface behavior between unsaturated soil and geomembranes	60
3.1 Background	60
3.2 Unsaturated Geomembrane-Soil Interface testing	67
3.2.1 Material and Sample Preparation	67
3.2.2 Unsaturated geomembrane and soil interface testing procedure	70
3.3 Saturated geomembrane-soil interface testing.....	73
3.3.1 Material and sample preparation.....	73
3.3.2 Saturated geomembrane-soil interface testing procedure	73
3.4 Saturated and unsaturated soil-soil interface testing	74
3.5 Results of unsaturated geomembrane-soil interface tests	74
3.5.1 Effect of net normal stress	75
3.6 Effect of shear displacement rate.....	80
3.6.1 Effect of rate of shear displacement on textured interface behavior	80
3.6.2 Effect of rate of displacement on smooth interface behavior	82
3.7 Effect of suction	84
3.7.1 Effect of suction on textured interface behavior	85
3.7.2 Effect of suction on smooth interface behavior.....	86
3.8 Results of saturated interface behavior	88
3.8.1 Effect of normal stress on saturated textured interface behavior	88
3.8.2 Effect of normal stress on saturated smooth interface behavior	89
3.9 Unsaturated/saturated soil direct shear test results	91
3.9.1 Unsaturated soil direct shear test results	91
3.9.2 Saturated soil direct shear test results.....	92
3.10 Interface strength model for unsaturated conditions.....	93
3.10.1 Extended Mohr-Coulomb criterion of unsaturated soil and interfaces.....	94
3.10.2 General elastoplastic constitutive model.....	99
3.10.3 Application of the constitutive model to the unsaturated soil-textured geomembrane interface test results	107

3.10.4 Application of the constitutive model to the unsaturated soil-smooth geomembrane interface test results	112
CHAPTER 4: Modeling lateral load behavior of piles in unsaturated soil due to seasonal moisture content changes	116
4.1 Background	116
4.2 Historical and future weather data collection	121
4.3 Predicting soil moisture changes using unsaturated seepage modeling	125
4.4 Results and calibration of soil moisture prediction models	132
4.5 Numerical modeling of pile-soil interaction considering the soil moisture changes	140
4.5.1 Finite difference method	140
4.5.2 Comparison of pile response using Evans and Duncan (1982) and Mokwa et al. (2000) p-y curve methods	143
4.6 Parametric study of pile-soil interaction in IAB	147
4.6.1 Abutment pile type and orientation	148
4.6.2 Type of soil surrounding the abutment piles	150
4.6.3 Type of backfill material	151
CHAPTER 5: Conclusions and recommendations	153
5.1 Summary: Impact of desiccation cracks on unsaturated soils	153
5.2 Conclusions: Impact of desiccation cracks on unsaturated soils	154
5.3 Recommendations: Impact of desiccation cracks on unsaturated soils	158
5.4 Summary: Unsaturated interface behavior between smooth or textured geomembranes and clayey soil	159
5.5 Conclusions: Unsaturated interface behavior between smooth or textured geomembranes and clayey soil	159
5.6 Recommendations: Unsaturated interface behavior between smooth or textured geomembranes and clayey soil	161
5.7 Summary: Modeling lateral load behavior of piles in unsaturated soil due to seasonal moisture content changes	162
5.8 Conclusions: Modeling lateral load behavior of piles in unsaturated soil due to seasonal moisture content changes	162
5.9 Recommendations: Modeling lateral load behavior of piles in unsaturated soil due to seasonal moisture content changes	163
References	165

Appendix A: Crack depth estimation for Chickasha slope 173

List of Tables

Table 2.1. Analytical parameters and assumptions	24
Table 2.2. Numerical parameters and assumptions.....	28
Table 2.3. Summary of saturated hydraulic conductivity values	49
Table 2.4. Summary of slope stability analysis.....	59
Table 3.1. Properties of the smooth and textured geomembranes used in the interface shear tests	70
Table 3.2. Test matrix of unsaturated geomembrane-soil interface tests	72
Table 3.3. Test matrix of saturated soil-geomembrane interface tests.....	73
Table 3.4. Test matrix of saturated and unsaturated soil-soil direct shear tests	74
Table 3.5. Unsaturated shear strength parameters (c , ϕ' , ϕ^b) for soil	98
Table 3.6. Unsaturated interface shear strength parameters (c'' , δ' , δ^b) for soil-geomembrane interface.....	99
Table 3.7. Model Parameters for the unsaturated textured geomembrane-soil Interface	108
Table 3.8. Model Parameters for the unsaturated textured geomembrane-soil Interface	112
Table 4.1. Properties of typical soli layers.....	141
Table 4.2. Properties of typical abutment piles	148
Table A.1. Analytical parameters and assumptions for Chickasha soil	173
Table A.2. Numerical parameters and assumptions for Chickasha soil	173

List of Figures

Figure 2.1. Newly developed desiccation box (a) and test set-up (b) (from Varsei et al. 2016).....	19
Figure 2.2. Tensile force changes during desiccation process	20
Figure 2.3. Uniaxial tensile strength (σ_{tu}) values at different initial water contents.....	20
Figure 2.4. Tensile strength for uniaxial and isotropic loading defined relative to Mohr-Coulomb failure envelope	21
Figure 2.5. Schematic drawing of desiccation test box for crack depth prediction showing approximate location of moisture sensors	23
Figure 2.6. Preparation process of sample for crack depth prediction (a) empty box, (b) compaction process, and (c) completed stage before desiccation process	23
Figure 2.7. Volume water content changes during desiccation in the desiccation box (a), suction changes of test soil (b) and Soil Water Characteristic Curve (SWCC) of test soil (c)	27
Figure 2.8. Suction changes versus depth of cracking according to equation 2.3	28
Figure 2.9. Suction changes versus depth of cracking according to equation 2.4	28
Figure 2.10. Calibrated suction changes through the depth of test soil using the numerical model, 0-12 MPa (a), 0-400 kPa, (b) color contours (c)	29
Figure 2.11. Desiccation crack depth measurement in the desiccation box, top view (a) side view (b).....	30
Figure 2.12. Tensile stress distribution curve (a) and color contours along soil profile using the numerical model (b)	31
Figure 2.13. Soil Water Characteristic Curve (SWCC) for single crack and intact soil....	34
Figure 2.14. Hydraulic conductivity function for single crack and intact soil	34
Figure 2.15. Geometry of a cracked soil considering single cracks with a ratio of crack spacing to crack height equal to (a) 1, (b) 0.5, (c) 0.25	37
Figure 2.16. Hydraulic conductivity function for a cracked layer.....	38
Figure 2.17. Geometry of a cracked soil considering equivalent layer	39
Figure 2.18. Pore water pressure distribution within cracked and intact layers (ratio of crack spacing to crack depth=1) for Discrete crack model (a), Equivalent layer model (b), and both models (c).....	42
Figure 2.19. Pore water pressure distribution within cracked and intact layers (ratio of crack spacing to crack depth=0.5) for Discrete crack model (a), Equivalent layer model (b), and both models (c)	43
Figure 2.20. Pore water pressure distribution within cracked and intact layers (ratio of crack spacing to crack depth=0.25) for Discrete crack model (a), Equivalent layer model (b), and both models (c)	44
Figure 2.21. Effect of crack width on flow of water at interface between cracked and intact layers	45
Figure 2.22. Effect of ratio of single crack to intact soil permeability on pore water pressures at a point located at 10 cm below the interface at different elapsed time ..	45

Figure 2.23. Effect of ratio of equivalent cracked layer to intact soil permeability on pore water pressures at a point located at 10 cm below the interface between cracked and intact layers at different elapsed time	46
Figure 2.24. Shear strength evolution under different net normal stresses and matric suctions.....	48
Figure 2.25. Shear strength evolution under different matric suctions and net normal stresses	48
Figure 2.26. Initial volumetric moisture content distribution and geometry of Chickasha slope	52
Figure 2.27. Rainfall data for Chickasha slope.....	52
Figure 2.28. Evaporation data from Aug. 2012 to Jun. 2014, (a) relative humidity, (b) average air temperature, (c) total solar radiation, (d) wind speed	53
Figure 2.29. Measured and Predicted Soil Moisture Changes for Intact and Cracked Slope at Three Different Depths (a) 0.3 m, (b) 0.90 m, and (c) 1.80 m.....	54
Figure 2.30. Geometry and mechanical properties of Chickasha embankment (slope)	56
Figure 2.31. Factor of Safety for intact slope, slope with discrete cracks, and slope with an equivalent cracked layer.....	57
Figure 2.32. Critical Factor of Safety using circular slip surface for intact slope	58
Figure 2.33. Critical Factor of Safety using circular slip surface for cracked slope (discrete crack model)	58
Figure 2.34. Critical Factor of Safety using circular slip surface for cracked slope (equivalent layer model)	59
Figure 3.1. Textured geomembrane cut and rolled (a) and smooth geomembrane cut and rolled (b)	68
Figure 3.2. Schematic cross section of the test chamber and shear box (from Khoury et al. 2011)	71
Figure 3.3. Shear stress changes during shearing at different net normal stresses for a matric suction of 200 kPa for textured geomembrane interface	76
Figure 3.4. Vertical displacement versus horizontal displacement at different net normal stresses for a matric suction of 200 kPa for textured geomembrane interface	77
Figure 3.5. Water volume change versus horizontal displacement at different net normal stresses for textured geomembrane interface	77
Figure 3.6. Shear stress changes during shearing at different net normal stresses for a matric suction of 200 kPa for smooth geomembrane interface.....	79
Figure 3.7. Vertical displacement versus horizontal displacement at different net normal stresses for a matric suction of 200 kPa for smooth geomembrane interface	79
Figure 3.8. Water volume change versus horizontal displacement at different net normal stresses for a matric suction of 200 kPa for smooth geomembrane interface	80
Figure 3.9. Shear stress changes during shearing at different strain rates for textured geomembrane-soil interface for a matric suction of 200 kPa.....	81
Figure 3.10. Vertical displacement versus horizontal displacement at different strain rates for textured geomembrane-soil interface	82

Figure 3.11. Extended Mohr-Coulomb envelope during a constant suction test at different displacement rates for textured geomembrane-soil interface for a matric suction of 200 kPa	82
Figure 3.12. Shear stress changes during shearing at different strain rates for smooth geomembrane-soil interface for a matric suction of 200 kPa.....	83
Figure 3.13. Vertical displacement versus horizontal displacement at different strain rates for smooth geomembrane-soil interface for a matric suction of 200 kPa.....	84
Figure 3.14. Extended Mohr-Coulomb envelope during a constant suction test at different displacement rates for smooth geomembrane-soil interface for a matric suction of 200 kPa	84
Figure 3.15. Shear stress changes during shearing at different suction for textured geomembrane-soil interface at net normal stress of 50 kPa.....	85
Figure 3.16. Vertical displacement versus horizontal displacement at different suction for textured geomembrane-soil interface at net normal stress of 50 kPa	86
Figure 3.17. Shear stress changes during shearing at different suction for smooth geomembrane-soil interface for a net normal stress of 50 kPa	87
Figure 3.18. Vertical displacement versus horizontal displacement at different suction for textured geomembrane-soil interface.....	87
Figure 3.19. Shear stress changes during shearing at different normal stresses for textured geomembrane-soil interface under saturated conditions	88
Figure 3.20. Vertical displacement versus horizontal displacement at different normal stresses for textured geomembrane-soil interface under saturated conditions.....	89
Figure 3.21. Shear stress changes during shearing at different normal stresses for smooth geomembrane-soil interface under saturated conditions.....	90
Figure 3.22. Vertical displacement versus horizontal displacement at different normal stresses for smooth geomembrane-soil interface under saturated conditions	90
Figure 3.23. Shear stress changes during shearing at different net normal stresses and suction=200 kPa for soil direct shear tests.....	91
Figure 3.24. Vertical displacement versus horizontal displacement at different net normal stresses and suction=200 kPa for soil direct shear tests	92
Figure 3.25. Shear stress changes during shearing at different net normal stresses and under saturated condition for soil direct shear tests.....	93
Figure 3.26. Vertical displacement versus horizontal displacement at different net normal stresses and under saturated condition for soil direct shear tests	93
Figure 3.27. Failure envelope projections of unsaturated textured geomembrane-soil interface on suction-shear strength plane	96
Figure 3.28. Failure envelope projections of unsaturated textured geomembrane-soil interface on net normal stress-shear strength plane	96
Figure 3.29. Failure envelope projections of unsaturated smooth geomembrane-soil interface on suction-shear strength plane	97
Figure 3.30. Failure envelope projections of unsaturated smooth geomembrane-soil interface on net normal stress-shear strength plane	97
Figure 3.31. Failure envelope projections of for unsaturated soil on suction-shear strength plane	98

Figure 3.32. Failure envelope projections of unsaturated soil on net normal stress-shear strength plane	98
Figure 3.33. Typical plot for determination of factors for ultimate parameter	103
Figure 3.34. Typical plot for determination of factor λ^* for bonding stress	104
Figure 3.35. Typical plot for determination of factors λ_1 and λ_2 for bonding stress ..	104
Figure 3.36. Typical Plot for determination of factors for hardening parameter from the experimental results.....	105
Figure 3.37. Typical plot for determination of “a” and “b” as hardening parameters from rough interface test results	106
Figure 3.38. Typical plot for determination of κ for suction of 200 kPa for rough interface	106
Figure 3.39. Typical plot for determination of residual parameters.....	107
Figure 3.40. A Comparison of Experimental and Predicted Results for Textured geomembrane and soil Interface Shear Test at Suction=200 kPa	110
Figure 3.41. A comparison of experimental and predicted results for textured geomembrane and soil interface shear test at net normal stress=50 kPa	111
Figure 3.42. A comparison of experimental and predicted results for smooth geomembrane and soil interface shear test at suction=200 kPa.....	114
Figure 3.43. A comparison of experimental and predicted results for smooth geomembrane and soil interface shear test at net normal stress=50 kPa	115
Figure 4.1. A sketch of Integral Abutment Bridge (IAB) (from Muraleetharan and Miller 2015).....	117
Figure 4.2. A sketch of Winkler springs (p-y curves) for pile-soil interaction models .	119
Figure 4.3. Average air temperature from 1950-2099 available in Comanche county, OK (data obtained from USGS via the National Climate Change Viewer)	122
Figure 4.4. Average precipitation from 1950-2099 available in Comanche county, OK (data obtained from USGS via the National Climate Change Viewer)	123
Figure 4.5. Geometry and initial condition of south abutment of I-44 Bridge	127
Figure 4.6. Soil Water Characteristic curve (SWCC) for clayey soil	128
Figure 4.7. Daily Precipitation data from 1994 to 2001 (from Oklahoma Mesonet Station Medicine Park).....	129
Figure 4.8. Daily Evaporation data from 1994 to 2001, (a) relative humidity, (b) average air temperature, (c) total solar radiation, (d) wind speed (from Oklahoma Mesonet Station Medicine Park)	130
Figure 4.9. Daily Transpiration data from 1994 to 2001, (a) leaf area index, (b) plant limiting function, (c) potential root uptake.....	131
Figure 4.10. Thornthwaite potential evapotranspiration and Penman potential evapotranspiration from 1994-2001.....	133
Figure 4.11. Calibration factor for monthly Thornthwaite potential evapotranspiration (m/month) from (a) January to (f) June	134
Figure 4.12. Calibration factor for monthly Thornthwaite potential evapotranspiration (m/month) from (g) July to (l) December.....	135

Figure 4.13. Calibrated Thornthwaite potential evapotranspiration and Penman potential evapotranspiration from 1994-2001	136
Figure 4.14. Leaf Area Index at different trials.....	136
Figure 4.15. Calibrated Thornthwaite actual evapotranspiration and Penman actual evapotranspiration from 1994-2001.....	137
Figure 4.16. Pore water pressure change around soil surrounding pile head from 1994-2001	137
Figure 4.17. (a) Suction predictions from 1950 until 2099 around soil surrounding pile head (b) Maximum suction profile in clayey soil layer.....	139
Figure 4.18. P-y curves obtained from Evans and Duncan (1982) equation.....	142
Figure 4.19. P-y curves obtained from Mokwa et al. (2000) equation	142
Figure 4.20. (a) Bending moment changes and (b) lateral deflection in the given abutment and pile using p-y curves from Evans and Duncan (1982)	145
Figure 4.21. (a) Bending moment changes and (b) lateral deflection in the given abutment and pile using p-y curves from Mokwa et al. (2000).....	146
Figure 4.22. Bending moment variations in the given pile using (a) Evans and Duncan (1982) equation (b) Mokwa et al. (2000) equation.....	147
Figure 4.23. Lateral deflection variations in the given pile using (a) Evans and Duncan (1982) equation (b) Mokwa et al. (2000) equation.....	147
Figure 4.24. Bending moment variations for different pile configurations (a) in abutment pile (b) in pile surrounded by clay soil.....	149
Figure 4.25. Variation in bending moments (a) in pile and abutment (b) in pile for different types of soil stiffness	151
Figure 4.26. Variation in bending moments for different types of backfill materials (a) in abutment and pile (b) in pile surrounded by clayey soil.....	152
Figure A.1. (a) Analytical results (b) numerical results for desiccation crack depth	174

Abstract

The behavioral change of soil, either mechanical or hydraulic, can be attributed to moisture changes. The soil layer above the groundwater table is often subjected to moisture variations due to weather changes or water table fluctuations. The soil moisture content associated with the degree of saturation are used to categorize the soil mechanics and hydraulics into saturated and unsaturated conditions. While common, considering soil to be saturated as a simplifying assumption in the design of many important geotechnical applications involving unsaturated soils is often not appropriate. In some geotechnical challenges, such as slope stability, soil-geosynthetic material interfaces, and soil-pile interaction, the application of unsaturated soil mechanics and hydraulics increases understanding of the problem and enhances our ability due to address moisture changes over the service life. In this study, three distinct moisture-dependent geotechnical subjects were investigated to enhance understanding of moisture variations in unsaturated soil engineering applications. The subjects include: 1) development and impact of desiccation cracks on unsaturated seepage and stability of slopes, 2) interface behavior between unsaturated soil and geomembranes, 3) and lateral load behavior of piles in unsaturated soil.

The stability of slopes has been widely studied using a variety of methods to evaluate the slope performance during and after construction. However, limited research has been conducted to employ unsaturated seepage analysis considering desiccation cracks in the evaluation of slope stability. In this research, a slope located in Chickasha, Oklahoma was instrumented to monitor local weather data and soil moisture

changes over time. Laboratory testing was conducted to determine unsaturated and saturated soil shear strength, soil water characteristic curves, tensile strength of soil and moisture flow properties. Two newly developed apparatuses: one for measuring the soil tensile strength during desiccation and one to examine formation of crack depths during desiccation were employed. A simple analytical model was developed for predicting desiccation crack depth and compared with the results of a numerical model using a finite element program. The results of tensile strength measurements were used for the analytical and numerical predictions of desiccation crack depth. The observations of desiccation crack depth developed in the proposed experimental set-up were used to verify the analytical and numerical results. Following verification, slope stability analysis was conducted using results of unsaturated seepage analysis considering a cracked layer. The results of slope stability analyses showed that the increase of permeability in a cracked layer and the loss of soil suction and cohesion during wetting were important triggering mechanisms for shallow slope failures.

Saturated interface shear strength variables between soil and geosynthetics have been extensively measured experimentally and predicted numerically using simplified constitutive models, but limited investigations were carried out to capture the clayey soil-geosynthetics material interface behavior under unsaturated conditions. Research in Part 2 was conducted to investigate the shearing behavior and develop a preliminary constitutive model for unsaturated clayey soil-geomembrane interfaces. Interface shear tests were carried out on clayey soil-geomembrane interfaces involving two types of geomembranes, smooth and textured HDPE. A series of suction-controlled

direct shear tests and saturated direct shear tests were conducted on the clayey soil to compare with the interface test results. A constitutive model was used to simulate the mechanical behavior observed in the experimental results. The experimental results showed that the unsaturated shear strength of soil-geomembrane interfaces was lower than the soil shear strength and lowest for the smooth geomembrane-soil interface. The constitutive models modified in this study were able to capture the experimental results through the back calculated parameters.

The design of piles in Integral Abutment Bridges (IABs) without considering the moisture changes of soil interacting with piles may adversely impact the bridge performance. In Part 3, the impact of variable soil saturation on the lateral load behavior of integral abutment piles was explored. Prediction of the soil moisture variations was conducted using a 2-D unsaturated seepage model with an atmospheric boundary condition based on climate predictions through the end of the century. A calibration technique in order to forecast the future weather was developed using the historical weather data. Forecasted weather information was used in the unsaturated seepage modeling to predict future moisture content variations and the associated matric suction profiles surrounding abutment piles. A range of matric suction based on the predicted moisture content profiles was employed in a numerical model to study the lateral load behavior of abutment piles subjected to temperature changes. The results indicated that the performance of piles interacting with unsaturated soil can be problematic under certain conditions.

CHAPTER 1: Introduction

Moisture changes, due to climate conditions or ground water fluctuations in unsaturated soils, lead to changes in soil hydraulic and mechanical behavior. This behavioral variation not only affects the performance of soil in earth structures, such as embankments, and earth dams, but also impacts structures interacting with soil, such as geomembrane liners and piles in bridge approach embankments. Research reported in this dissertation focused on three important geotechnical problems related to moisture and suction change in unsaturated soil: Part 1) development and impact of desiccation cracks on unsaturated soils; Part 2) interface behavior between unsaturated soil and geomembranes and Part 3) lateral load behavior of piles in unsaturated soil. All three of the topics explore the impact of changing moisture and suction on the mechanical behavior of the soil. Parts 1 and 3 also examine the flow of moisture due to weather changes in unsaturated soil engineering applications.

1.1 Overview Part 1: Development and impact of desiccation cracks on unsaturated soils

Frequent occurrence of failures in natural and man-made roadway cuts and embankments such as those observed along roadways in Idabel and Chickasha, Oklahoma, is a major issue for the Oklahoma Department of Transportation (ODOT). This type of failure is often preceded by periods of drying and formation of desiccation cracks followed by significant precipitation events. Formation and propagation of desiccation cracks play a crucial role in the stability of slopes by impacting mechanical and hydraulic soil properties in upper layers of the slope. Desiccation cracks allow water

to rapidly infiltrate the soil layers, and lead to slope failure by changing the pore water pressures as well as shear strength.

In the majority of slopes located in Oklahoma, the soil mass is in an unsaturated state within the active zone; the active zone is defined as the depth of soil over which moisture content fluctuates due to seasonal weather. During periods of prolonged drying, soil suction can increase in the active zone and form desiccation cracks. The increased hydraulic conductivity of soil, due to the presence of desiccation cracks, allows water to penetrate the soil layers easily and quickly, reducing the soil suction and shear strength. It is thus important to consider the influence of desiccation cracks on the stability of slopes formed of unsaturated cohesive soil. Research in this dissertation has focused on a method for predicting desiccation crack depths in unsaturated soil, a method for modeling unsaturated seepage in soil with desiccation cracks, and recommendations for modeling slope stability in slopes with desiccation cracks.

1.2 Overview Part 2: Interface behavior between unsaturated soil and geomembranes

The stability of geomembrane-soil interfaces is important to consider in the design of liner systems subjected to shear forces. A composite geomembrane liner on a landfill slope can be an ideal example. The interface behavior between geomembrane and soil are influenced by type of geomembrane, soil type, shear displacement rate, soil moisture content, and soil density. Generally, the soil begins to interact with geomembrane in an unsaturated condition, implying that relevant interface strength models should consider soil suction. Over time, the soil in contact with the geomembrane may become saturated depending on the geologic setting and

characteristics of the containment system. Thus, research reported herein involved an experimental study of geomembrane-soil interface behavior using a direct shear device developed for unsaturated soils. The study examines interface behavior under unsaturated and saturated conditions as well as the influence of shearing rate.

1.3 Overview Part 3: Modeling lateral load behavior of piles in unsaturated soil due to seasonal moisture content changes

Piles that support Integral Abutment Bridges (IABs) experience significant lateral loading due to variations in daily and seasonal bridge temperatures. Bending stresses at the top of pile can be significant when the soil surrounding the pile is relatively stiff. The increase of such stresses can reduce the axial capacity of a pile by creating a plastic hinge. Thus, it is important to consider the system flexibility in modeling the pile response. The pile and surrounding soil stiffness are principal parameters that determine the system flexibility. Based on classical unsaturated soil mechanics, it is known that unsaturated soil, with less than 100% degree of saturation, has a stiffness more than soil with a fully saturated condition. Since soil surrounding abutment piles in embankments may experience changes in degree of saturation over time, it will experience variations in soil stiffness. Therefore, the long-term effect of moisture changes on soil-pile interaction needs to be further investigated considering expected weather conditions. Research presented in this dissertation builds on a previous study at the University of Oklahoma (OU) that examined performance of piles in Integral Abutment Bridges (IABs) under thermal loading (e.g. I-44 Bridge in Oklahoma). This study showed that bending moments at shallow depths may exceed the yielding bending moment of piles when the soil stiffness is excessive. This observation was analyzed and simulated numerically at

OU without considering the soil moisture changes. The current study utilizes projected weather parameters to predict expected moisture changes in soil surrounding piles using unsaturated seepage modeling, and then utilizes modified p-y curves for piles in unsaturated soils to examine the impact of variable moisture conditions on lateral load behavior.

1.4 Summary of research contributions

The research makes important contributions to the state of knowledge in the field of geotechnical engineering as follows:

1. A novel approach for predicting desiccation crack depth in compacted clayey soils is developed and partially validated. This novel approach utilizes a newly derived analytical equation that relates the suction change to tensile failure and cracking in soil. When combined with actual or expected variations in suction within the active zone of a soil profile, it is possible to predict the depth of desiccation cracking. Heretofore, no such model existed for predicting desiccation crack depths in unsaturated compacted soils. The model has numerous potential applications in unsaturated geotechnics, including those described subsequently.

2. A method for simulating the impact of desiccation cracks on unsaturated seepage was developed and partially validated. While some work has been done in this area, the author's approach is unique and offers a simple, yet powerful method for considering desiccation cracks in unsaturated seepage models for certain applications. The author's approach utilizes an equivalent permeability for the cracked layer, based

on comparisons of numerical modeling of unsaturated flow in cracked layers and non-cracked layers with equivalent permeability.

3. A method for analyzing stability of slopes with desiccation cracks is demonstrated and partially validated. This method builds on the contributions of 1 and 2 above, and offers a new approach to stability modeling considering the unsaturated character of slopes.

4. There is a dearth of experimental data involving suction-controlled interface testing with soil and geomembranes published in the literature. The experiments conducted during this research provide such data and recommendations for developing constitutive models for unsaturated soil-geomembrane behavior for both smooth and textured geomembranes.

5. A method for assembling weather data based on climate projections for a region was developed for input into unsaturated seepage modeling. Output from the unsaturated seepage modeling is being used to examine the variations in soil moisture content and suction over time, which is indirectly used to develop p-y curves for lateral loading analysis of abutment piles. In this way, the abutment pile behavior can be examined based on future climate scenarios. To the author's knowledge, such a study has not been undertaken. The importance of understanding unsaturated soil behavior in dealing with the abovementioned applications is illustrated in the following sections.

1.5 Objectives and Scopes of Research

Changes in hydraulic and mechanical behavior of soil in under the influence of weather conditions, can lead to instability of earth structures such as slopes. The presence of

cracks due to the desiccation process can exacerbate the instability of slopes. To better understand the impact of desiccation cracks on the slope stability the following scope of work was accomplished:

- Developed an analytical method to predict the desiccation crack depth for a compacted clay.
- Developed a methodology to quantify the water flow through a compacted clay layer having desiccation cracks using unsaturated seepage analysis.
- Analyzed the seepage and stability of a slope modeled with cracked and intact layers distinguished using the desiccation crack depth computation.

Variations in saturation of soil in the interface or contact zone between soil and geomembrane can lead to changes the shearing behavior of the interface. To study the influence of water on the interface behavior, which manifests as either positive or negative pore water pressure, the following scope of work was completed:

- Modified/developed a constitutive model to predict the unsaturated shearing and volume change behavior of the contact zone or interface between soil and geomembrane.
- Conducted experimental interface direct shear tests with suction control on unsaturated contact zone between soil and geomembrane, determined parameters required for the proposed models, and compared experimental and model results.

Lateral load behavior of piles in Integral Abutment Bridges (IABs) can change under unsaturated conditions of soil surrounding piles. To investigate the impact of changing moisture conditions on IABs, the following scope of work was completed:

- Developed a methodology to predict weather input parameters for future weather events based on historical weather data and climate prediction models.
- Predicted soil moisture changes numerically around an IAB pile based on historical and future climate changes.
- Evaluated the performance of an IAB pile, taking into account the soil moisture changes.

1.6 Outline of dissertation

The dissertation is divided into 5 chapters with three main subjects. In Chapter 1, the introduction and scope of the three main subjects was presented. In Chapter 2, the impact of desiccation cracks on the slope stability analysis as a first subject is discussed. Chapter 3 discusses the unsaturated and saturated shearing behavior of interfaces (textured geomembrane-clayey soil, smooth geomembrane-clayey soil, and clayey soil-soil interfaces) as the second subject. In Chapter 4, the third subject of the dissertation, which is the pile-soil interaction under temporal variations of temperature and moisture content, is presented. Finally, Chapter 5 presents the conclusions and recommendations relevant to all three subjects.

CHAPTER 2: Development and impact of desiccation cracks on unsaturated soils

2.1 Background

Dealing with desiccation cracks due to soil shrinkage creates substantial challenges in various types of geotechnical projects, such as landfills, earth-dams, slopes, liners, and pavements. Loss of water from a soil mass, due to evaporation, results in soil shrinkage. The internal or external restraints against the soil shrinkage create desiccation cracks and potential flow paths within soil mass.

In order to capture the desiccation cracking development, there are a variety of techniques from simple to advanced employed using image processing (e.g. Miller et al. 1998, Vogel et al. 2005(a) and (b)). Application of image processing techniques were shown to be efficient in detecting the geometric and morphologic parameters of cracks, such as crack width, length, area, angle, and their distribution characteristics.

The crack intensity factor (CIF) was introduced by Miller et al. (1998) as a descriptor of the extent of surficial cracking. CIF was defined as the time-variable ratio of the surface crack area to the total surface area of the clay. They analyzed soil moisture suction and crack propagation for three distinct periods of wetting and drying. The first period, termed compaction-dry, corresponds to the time between the completion of compaction to fully dry conditions. Rainfall was then applied to the dry soil. The period between the fully dry condition and infiltration of the ponded water from the simulated rainfall was termed the dry-wet period. The soil tank was sealed with a glass cover during the infiltration phase to prevent evaporation of moisture. The last period of a cycle was the wet-dry period. The cover was removed at the beginning of the wet-dry

period, which began with the end of the second period and terminated with the development of fully dry conditions. The observed maximum crack widths for the compaction-dry and wet-dry periods were 5.0 mm and 9.5 mm, respectively. The crack pattern during the wet-dry period was polygonal as opposed to the linear nature of the cracks that developed during the compaction-dry period.

Stirk (1954) studied the effect of cracking and increasing the rate of water entry into fine-grained soil. The results indicated that the effect of cracking on the soil hydraulic conductivity at a relatively high level of water content (the wilting point) was not considerable. Experimental study of desiccation cracking and development of a simple theory to explain development of desiccation cracks was conducted by Corte and Higashi (1964). The laboratory tests were carried out by using slurry and loosely compacted soils on a wooden plate with the length to width ratio of 1.4 and thickness of 70 mm. It was observed that the cracks were arranged in an orthogonal and sequential manner with the primary cracks forming several cells in the specimen. The tests conducted by them also illustrated that the mean cell area increases as the thickness increases and that lower soil density would lead to lower mean cell area.

The non-capillary flow through the continuous holes or cracks was modeled numerically by Edwards et al. (1979). They proposed a two-dimensional model which allows for vertical infiltration from the soil surface and for lateral infiltration from a vertical hole after excess precipitation on the surface runs into the opening. In the model, the effect of water capillarity on the infiltration into macro-pores was not taken into account. However, the geometry and number of cracks per unit surface area were

considered. They found that the macro-pores can lead to significantly different infiltration rates and patterns of soil moisture in the soil matrix when the heavy rainfall or irrigation occurs. Hoogmoed and Bouma (1980) simulated a two-dimensional infiltration into a cracked unsaturated clay soil considering the vertical infiltration on the upper soil surface, the downward flow into the crack, and the horizontal infiltration from the crack into the soil. The simulated results showed that the flow of free water along the macro-pores or cracks into the soil matrix with high moisture content was faster than that of soil with lower moisture content.

Morris et al. (1992) developed the mechanics of cracking after reviewing the morphology of cracks in the field. They proposed three different solutions based on the elastic theory, transition between tensile and shear strength, and linear elastic fracture mechanics. To develop all three solutions, they considered that the soil subjected to desiccation cracking is initially saturated and essentially normally consolidated, and that under unsaturated conditions the soil behavior is governed by two stress variables (i.e. matric suction and net normal stress variables). These initial conditions were consistent with the nature of mine tailing they were investigating. They concluded that in addition to soil suction, soil properties such as compression modulus, Poisson's ratio, shear strength, tensile strength, and specific surface energy are factors that affect desiccation crack development in soil. In addition, of the three solutions they proposed, they found that the methods based on the elastic theory and tension-shear strength gave the most favorable predictions of desiccation crack depth compared to their limited empirical observations.

Konrad and Ayad (1997) proposed a model to predict the average crack spacing for slurries, consolidated natural soil, and compacted clays undergoing desiccation based on linear elastic fracture mechanics theory. A trapezoidal distribution of total horizontal tensile stress with a maximum value equal to tensile strength at the ground surface and minimum value at the ultimate crack depth was assumed to model crack propagation. The model was verified by Ayad et al. (1997) using the field data and soil properties, such as soil-water characteristic curve, tensile strength, and the fracture toughness measured from the intact clay. Chertkov and Ravina (1999) proposed a model for analyzing the geometrical characteristics of vertical and horizontal shrinkage cracks based on the model of multiple cracking and fragmentation originally developed for rocks. The model was able to estimate the width and volume of vertical cracks in clay soils. Water table depth, thickness of intensive cracking layer, and linear shrinkage of soil were parameters required to predict the characteristics of vertical cracks.

Studies of desiccation cracks from lab scale to field scale have received attention from numerous researchers; however, a few studies have been conducted to explore the effect of desiccation cracks on the slope stability. For example, Zhang et al. (2012) employed a centrifuge model to examine the stability of cracked slopes under rainfall conditions. The effect of cracks on the failure of the slopes due to rainfall events was analyzed based on suction and deformation measurements of the slope, which were recorded during the tests. A vertical and inclined crack with a certain width and depth was determined to investigate the effect of different positions of cracks. They have concluded that the displacement of the slope had a direct relationship with the rainfall

penetration. It was shown that both horizontal and vertical displacements increased as the rainfall increased. The inclined crack induced a larger displacement of the slope than the vertical crack near the slope surface.

The cracked slope stability was also investigated by considering the effects of crack location and depth, and rainfall intensity in the study conducted by Wang et al., (2011). The properties of a single crack including the saturated and unsaturated hydraulic conductivity were taken into account as specific material properties. The Seep/W program was used in the pore water pressure analysis, and the Slope/W was employed in the slope stability analysis. A theoretical method proposed by Wang (2011) was used to produce the SWCC and permeability function for a rough crack having random aperture distributions. The shear strength of a crack was assumed to be zero and the volume change of the crack upon drying and wetting were not considered during the numerical analysis. The effect of crack location on the slope stability was studied by considering a deep crack located on the crest and the middle of the slope separately. It was observed that a crack located in the middle of the slope affects the slope stability analysis more than other crack locations.

To characterize the strength and time rate aspects of shallow slide failures, Aubeny and Lytton (2004) proposed two models of slope failure for high plasticity clays, a stability model and a moisture diffusion model, respectively. They concluded that a destabilizing hydraulic gradient in the slopes due to increase of pore water pressure over many years of infiltration is the reason for slope failure. Their field observations indicated that there are no large strains that result in a degradation of effective friction

angle from peak to residual value for the slopes. However, the destabilizing hydraulic gradient was sufficient to produce shear failure considering peak strengths for normally consolidated soil conditions.

2.2 Modeling and predicting desiccation crack depth in unsaturated soil

Development of a vertical desiccation crack in soil due to drying is a hydro-mechanical phenomenon. Hydraulic and mechanical properties of soil change while crack depth is developed gradually. In this section, an analytical model is presented. The model was developed by employing the theory of elasticity and incorporating mechanical characteristics of soil, including tensile strength, elastic properties and change in suction. This simple analytical model can be used to predict desiccation crack depth if changes in suction can be predicted for a given soil profile. For comparison, a numerical model considering both mechanical and hydraulic properties of soil is employed to predict the desiccation crack depth. Finally, an experimental test is used to verify the analytical and numerical models.

2.2.1 Analytical model for predicting crack depth

The author and his colleagues (Miller et al., 2015) have developed a model based on the elastic theory for prediction of a desiccation crack depth in unsaturated compacted soil. Morris et al. (1992) developed a simple approach for predicting desiccation crack depth in mine tailings, which essentially were modeled as initially saturated normally consolidated soil. The basic elastic equation for the incremental horizontal strain in an unsaturated soil is (Fredlund and Rahardjo, 1993):

$$\Delta \varepsilon_x = \frac{\Delta(\sigma_x - u_a)}{E} - \frac{\nu}{E} (\Delta \sigma_y + \Delta \sigma_z - 2\Delta u_a) + \frac{\Delta(u_a - u_w)}{H} \quad (2-1)$$

where, $\Delta \varepsilon_x$ = is taken as strain normal to the long axis of the crack prior to cracking;
 $\Delta(\sigma_x - u_a)$ is the change in net normal stress in the horizontal direction, u_a is the air pressure, u_w is water pressure, $\Delta(u_a - u_w)$ is the change in matric suction; and E and H are the elastic moduli with respect to net normal stress and suction, respectively. Incorporating the assumptions, $\Delta \varepsilon_x = 0$, $\Delta \sigma_x = \Delta \sigma_y$, and $u_a = 0$ the above equation is simplified to:

$$\Delta \sigma_x = \frac{\nu}{1-\nu} \Delta \sigma_z - \frac{E}{H(1-\nu)} \Delta(u_a - u_w) \quad (2-2)$$

The initial horizontal stress, σ_{x0} is equal to $K_o \sigma_{v0} = K_o \gamma z_c$, and the final horizontal stress, σ_{xf} , is assumed to be equal to the tensile strength of the soil, σ_t ; thus, $\Delta \sigma_x = \sigma_t - K_o \gamma z_c$. The initial vertical stress, σ_{z0} is equal to $\sigma_{v0} = \gamma z_c$, and the final vertical stress, σ_{zf} , can be assumed to be zero or equal to the initial one; thus, $\Delta \sigma_z = -\gamma z_c$, or zero. That is, there are two possible assumptions with respect to the change in vertical stress. If one assumes the crack formation occurs instantaneously, then the change in vertical stress is assumed to be zero at the point of crack initiation. However, if the crack is assumed to develop gradually, then the vertical stress at the bottom of the crack would be zero. Both assumptions are explored in this research.

The vertical total stress is σ_{v0} ; γ is the total unit weight; z_c is the depth of cracking; and K_o is the ratio of the horizontal to vertical total stress before desiccation.

Substituting these expressions into above equation leads to an expression for the change in suction:

$$\Delta(u_a - u_w) = \frac{z_c \gamma [v - K_o(1-v)] + (1-v)\sigma_t}{E/H} \quad \text{if} \quad \Delta\sigma_z = -\gamma z_c \quad (2-3)$$

$$\Delta(u_a - u_w) = \frac{z_c \gamma K_o(1-v) - (1-v)\sigma_t}{E/H} \quad \text{if} \quad \Delta\sigma_z = 0 \quad (2-4)$$

Using either of these equations, depending on the assumption employed regarding change in vertical stress at the point of cracking, one can predict the depth of cracking, z_c , associated with a given change in matric suction provided the other parameters can be reasonably estimated. Thus, if the variation in matric suction is known or can be predicted for an actual soil profile during drying, the depth of cracking can be predicted using the above equations.

2.2.2 Numerical model for predicting crack depth

Numerical modelling was used to predict depth of cracking in unsaturated soil based on tensile stress variations due to drying on the ground surface. Temporal variations of suction in a soil profile can be modeled using a hydro-mechanical finite element program called Code Bright (DIT-UPC, 2015). By manipulating the drying boundary conditions at the ground surface, the change of suction with time at different depths predicted by the model can be adjusted to match an actual suction profile obtained by field measurements or a laboratory bench scale model. Then the tensile stress variations predicted by the model are compared to the actual tensile strength of the soil and crack

depth is assumed to correspond to the depth where the predicted tensile stress exceeds the tensile strength.

For this research, suction changes with depth were obtained in the field based on moisture probe measurements at a test site located in Chickasha, Oklahoma. In addition, a laboratory desiccation model experiment was constructed to observe crack depths in a soil bed with moisture sensor measurements. As mentioned before, to form a crack in the soil bed, shrinkage needs to be restrained and tensile stress due to change of water content must exceed the tensile strength of the soil. Using Code Bright, a three-dimensional model resembling the experimental test was simulated with appropriate boundary conditions. Note, a 2-D model would be sufficient to model this problem assuming the soil in the box was under plane strain condition. However, for this test apparatus, the 3-D model was simple to develop within Code Bright and so was utilized. The bottom of the model was constrained in the vertical and the horizontal direction. The two sides of the model were just constrained in the horizontal direction. The top of model was subjected to suction changes without any prescribed displacement. For the simple elastic behavior modeled in this problem, the Code Bright program employs simple linear elastic equations that account for changes in mean net stress, suction and temperature. For example, the following equation is used to compute the volumetric strain as a function of mean net stress, suction, and temperature changes,

$$\Delta\varepsilon_v = \frac{\Delta P''}{K} + \frac{\Delta(P_g - P_l)}{K_s} + \frac{\Delta T}{K_T} \quad (2-5)$$

where: P'' is mean net stress; $(P_g - P_l)$ is suction; T is temperature and it is assumed that ΔT is equal to zero. K , K_s , and K_T are bulk moduli with respect to mean net stress, suction, and temperature changes, respectively.

Intrinsic permeability was calculated from the following equation,

$$\kappa = k \frac{\mu}{\rho g} \quad (2-6)$$

where: k is coefficient of permeability measured in the laboratory and μ , ρ , and g are dynamic viscosity of water, density of water, and acceleration due to gravity, respectively.

2.2.3 Tensile strength of a compacted soil

As mentioned in the previous sections, the tensile strength of soil is one of the substantial parameters to predict the crack depth of a compacted soil during desiccation for both the analytical and numerical methods. A series of tensile strength tests on the soil used for the crack depth prediction in the laboratory condition was conducted using a novel apparatus developed by Varsei et al. (2016) at OU to measure the tensile strength of compacted soil beds while drying. As shown in Figure 2.1(a), the desiccation test apparatus was a 25 cm \times 30 cm rectangular shaped box with two separate halves. One half was fixed and there were some ball bearings under the other half to reduce the friction between the box and the surface below it. There were two load cells attached to the box, where the two halves joined to measure the tensile force generated in the specimen while it was drying. The load cells have a range up to 445 N, a resolution of 0.044 N, and a full scale accuracy of 0.03 % (± 0.13 N). There was a small gap between

the two halves of the box, which allowed the tension in the soil to be transmitted to the load cells on either side. Screws were installed in the two end walls of the box perpendicular to the wide direction to provide a constraining condition for soil coupled with them. This condition prevented the soil at the boundaries from pulling away from the ends during shrinkage and caused the desiccation crack to form at the mid-section of the box, where the maximum tensile stress was expected to occur. Figure 2.1(b) shows a picture of the bench scale set-up including the desiccation box, overhead camera and a digital scale. The digital camera was able to monitor the formation of desiccation crack and loss of moisture measured using the digital scale at the given time intervals. The digital scale had a capacity of 8100 g, readability of 0.1 g, and accuracy of ± 0.3 g.

Unlike previous methods, the newly developed device presented and used in this study provides a condition to measure the tensile strength of soil during the desiccation process. This condition resembles the natural process in drying soil, where tensile stresses develop with decreasing water content, and cracks develop at a water content lower than the initial water content.

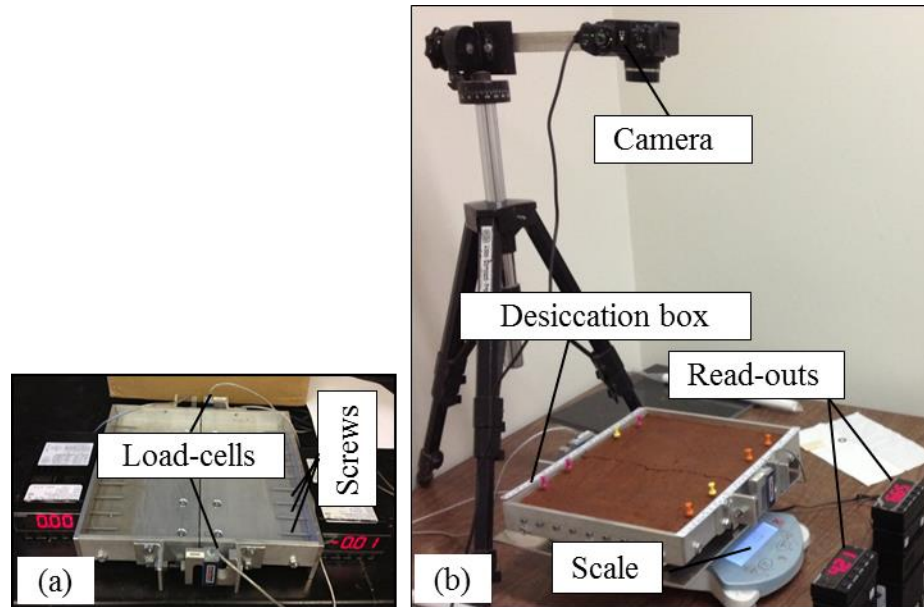


Figure 2.1. Newly developed desiccation box (a) and test set-up (b) (from Varsei et al. 2016)

The soil used for the tensile strength tests was from the CS2780 borrow source and had an optimum moisture content (OMC) of 14.9%, maximum dry unit weight of 18.8 kN/m^3 , liquid limit of 39%, plasticity index of 17%, and 95.2% of fines. The specimens were prepared at three initial conditions of moisture content including OMC, +2% wet of OMC, and -2% dry of OMC and placed in the moisture room for 24 hours to promote uniform distribution of water within the soil. The specimens were compacted at 95% maximum dry unit weight. The tensile force evolution during the desiccation process was recorded as shown in Figure 2.2. The tensile strength was calculated using the peak value of tensile force divided by the effective cross sectional area, which was assumed to be a product of the width of the box (25 cm) and the initial thickness of the specimen (1.25 cm). The tensile strength of the compacted soil at three different initial conditions is shown in Figure 2.3.

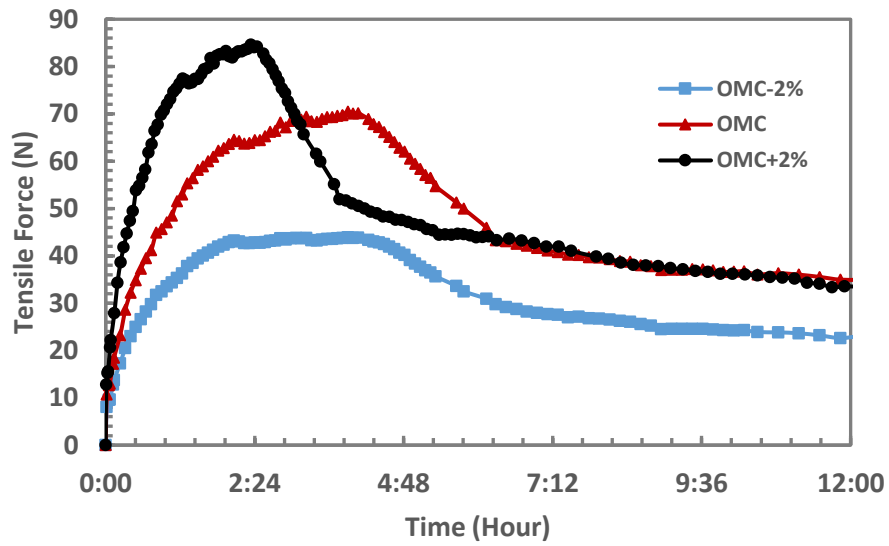


Figure 2.2. Tensile force changes during desiccation process

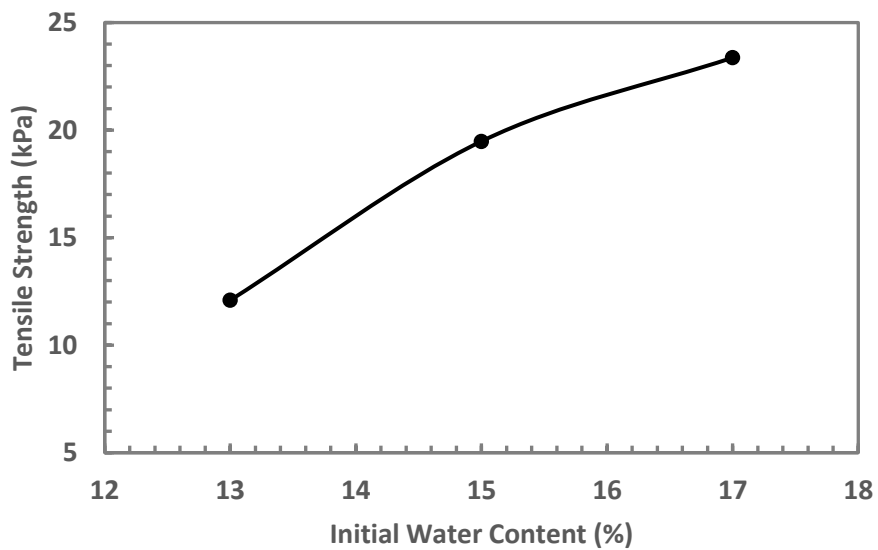


Figure 2.3. Uniaxial tensile strength (σ_{tu}) values at different initial water contents

Stress conditions in the soil bed approximate a uniaxial stress condition whereby the major principal total stress at failure is zero and the minor principal stress is equal to the uniaxial tensile strength (σ_{tu}), as shown in Figure 2.3. To estimate the tensile

strength corresponding to isotropic loading (σ_t), the expression shown in Figure 2.4 can be used if the effective stress friction angle of the soil (ϕ') is known, given as:

$$\sigma_t = \sigma_{tw} \frac{1 + \sin \phi'}{2 \tan \phi' \cos \phi'} \quad (2-7)$$

For estimating crack depth, the tensile strength corresponding to isotropic loading was computed using Equation 2-7.

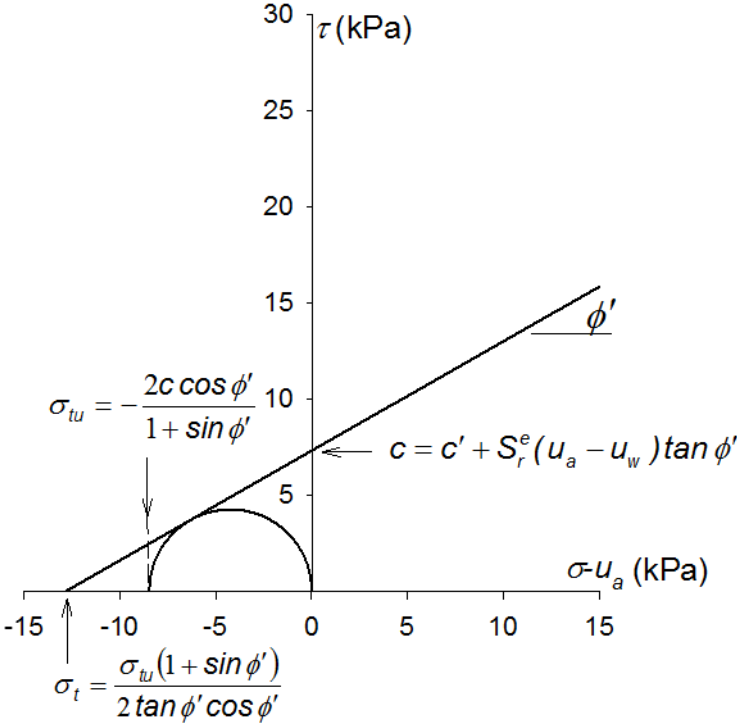


Figure 2.4. Tensile strength for uniaxial and isotropic loading defined relative to Mohr-Coulomb failure envelope

2.2.4 Comparison of analytical and numerical results with experimental data

The analytical model can be partially validated from comparison to the numerical model described above. The validation and calibration of the numerical approach can be

achieved by comparison to empirical data collected from actual experiments. For this purpose, an experimental test was designed in order to monitor and record the changes of suction associated with crack depth development in a clayey soil. A box with 570 x 895 x 100 mm length, height, and width was fabricated to monitor the desiccation crack depth. The material used for the front and back sheet of the box was made of plexiglass acrylic to observe the desiccation cracks propagation within the depth of the compacted soil. Two sides of the box were made of the wood. Wood screws were installed horizontally into the soil at regular vertical intervals along each side of the box to constrain the horizontal shrinkage. Five volumetric water content sensors (Decagon EC-5 soil moisture sensors) connected to a data logger and laptop were installed at different depths of soil to record moisture changes during drying. The EC-5 sensor measures volumetric water content through the dielectric constant of the media using the capacitance/frequency domain technology. A schematic set-up is shown in Figure 2.5. The test soil for this experiment was the same soil used for the tensile strength testing described previously. It was compacted at 95% maximum dry unit weight and 2% wet of optimum moisture content (+2% OMC). To avoid the moisture loss during the sample compaction, the prototype preparation was conducted in the moisture room as shown in Figures 2.6(a) and (b). Wood stiffeners and clips were employed to control the buckling deformation of plexiglass sheets during the compaction and desiccation process as shown in Figure 2.6(c). A summary of soil parameters and properties used for the analytical and numerical methods to compare with the experimental test is shown in Tables 2.1 and 2.2.

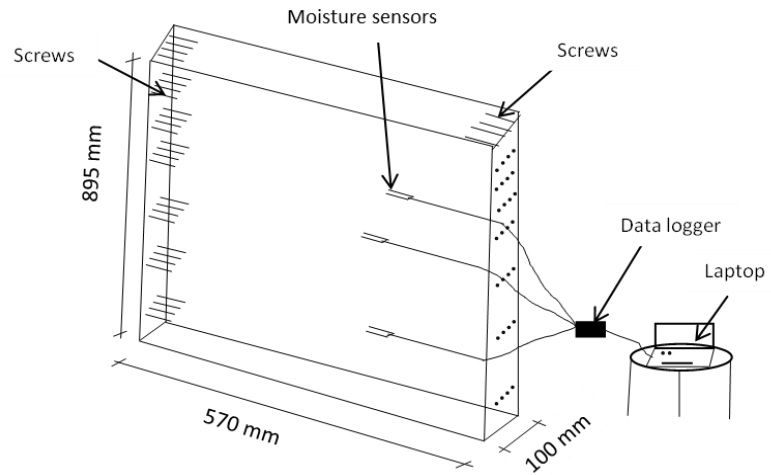


Figure 2.5. Schematic drawing of desiccation test box for crack depth prediction showing approximate location of moisture sensors

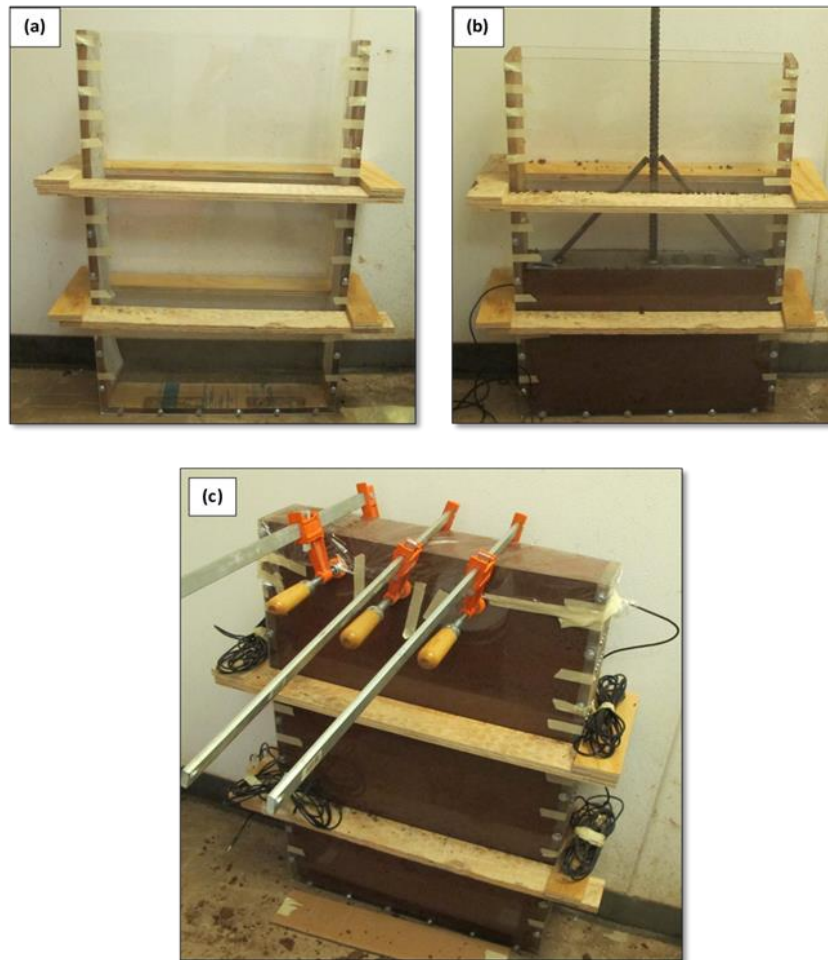


Figure 2.6. Preparation process of sample for crack depth prediction (a) empty box, (b) compaction process, and (c) completed stage before desiccation process

For the analytical method, Equations 2.3 and 2.4 indicate the dependency of crack depth on the suction change and soil properties. Upper and lower bound predictions of the crack depth and suction change were derived using the range of both estimated and measured parameters summarized in Table 2.1. The ranges for Poisson's ratio, the coefficient of earth pressure at rest, and the ratio of elastic moduli with respect to net normal stress and suction, were estimated using $\pm 25\%$ of the basic values used by Morris (1992) and suggested by Fredlund and Rahardjo (1993).

Table 2.1. Analytical parameters and assumptions

Parameter	Value	Determined by:
γ (kN/m ³)	20.9	measurement
ν	0.26-0.44	estimation
E/H	0.23-0.38	estimation
K_o	0.50-0.88	estimation
ϕ'	34	measurement
σ_i (kPa)	-33	measurement

To estimate the cracking depth using the analytical equations, Equation 2.3 or 2.4 is selected to calculate the suction that will produce cracking as a function of depth and this linear relationship is plotted as suction change (abscissa) versus depth (ordinate), as shown in Figures 2.8 and 2.9 for Equations 2.3 and 2.4 using the average parameters in Table 2.1. On top of this, the actual measured suction profile is plotted, also shown in Figures 2.8 and 2.9, and the intersection of the analytically predicted cracking suction with the actual measured suction profile represents the depth of cracking.

Using the analytical method, a range of cracking depths was calculated based on Equations 2.3 and 2.4 and the range of parameters shown in Table 2.1. The suction variation curve was derived from monitoring the volumetric water content change and

using the soil water characteristic curve (SWCC) as shown in Figures 2.7(a) to (c). The locations of sensors were 0.04, 0.22, 0.42, 0.59, and 0.84 m from top of the box, respectively. Figure 2.7(a) shows that the desiccation rate in upper layer was higher than other layers at early stages of desiccation and then leveled off at later stages. When the test was ended, essentially all of the sensors indicated a constant volumetric water content and this corresponded to the end of crack propagation. Thus, the suction profile at the end of the test is used to predict crack depth. The range of cracking suction predicted by Equations 2.3 and 2.4 is represented by the black lines and shaded area in Figures 2.8 and 2.9, respectively, for the desiccation box test. The intersection of the experimentally determined suction in the desiccation box indicated by the blue symbols and line with the analytically predicting cracking suction represents the estimated cracking depth. As shown in Figures 2.8 and 2.9, the predicted range of cracking depths are 55 to 62 cm and 53 to 59 cm for Equations 2.3 and 2.4, respectively. For comparison, the actual desiccation crack depths at the desiccation box was measured to be close to 42 cm depth as shown in Figure 2.11.

In the numerical method, the suction variations were based on the measured and estimated parameters in Table 2.2. The gray symbols and line indicated in Figures 2.8 and 2.9 are the predicted changes in suction based on the calibrated numerical model shown in Figure 2.10. The calibrated suction changes were obtained after applying a suction change of 12 MPa for 120 days on the boundary surface located on the top of the model. The calibrated suction values reasonably match the experimentally determined suction values below a depth of 0.4 m as shown in Figures 2.10 (a) & (b).

However, the predicted suction values above 0.4 m don't agree well with measured values. Since the critical cracking suction is relatively low and occurs at depths greater than 0.4 m, the objective was to produce the best match for the greater depths. More refinement in the approach to calibration may result in a better match for values above 0.4 m. The resulting tensile stress distribution predicted in the soil profile using the numerical model is shown in Figure 2.12. The crack depth can be estimated using the numerical modeling results by comparing predicted tensile stress to the measured tensile strength of soil as shown in Figure 2.12.

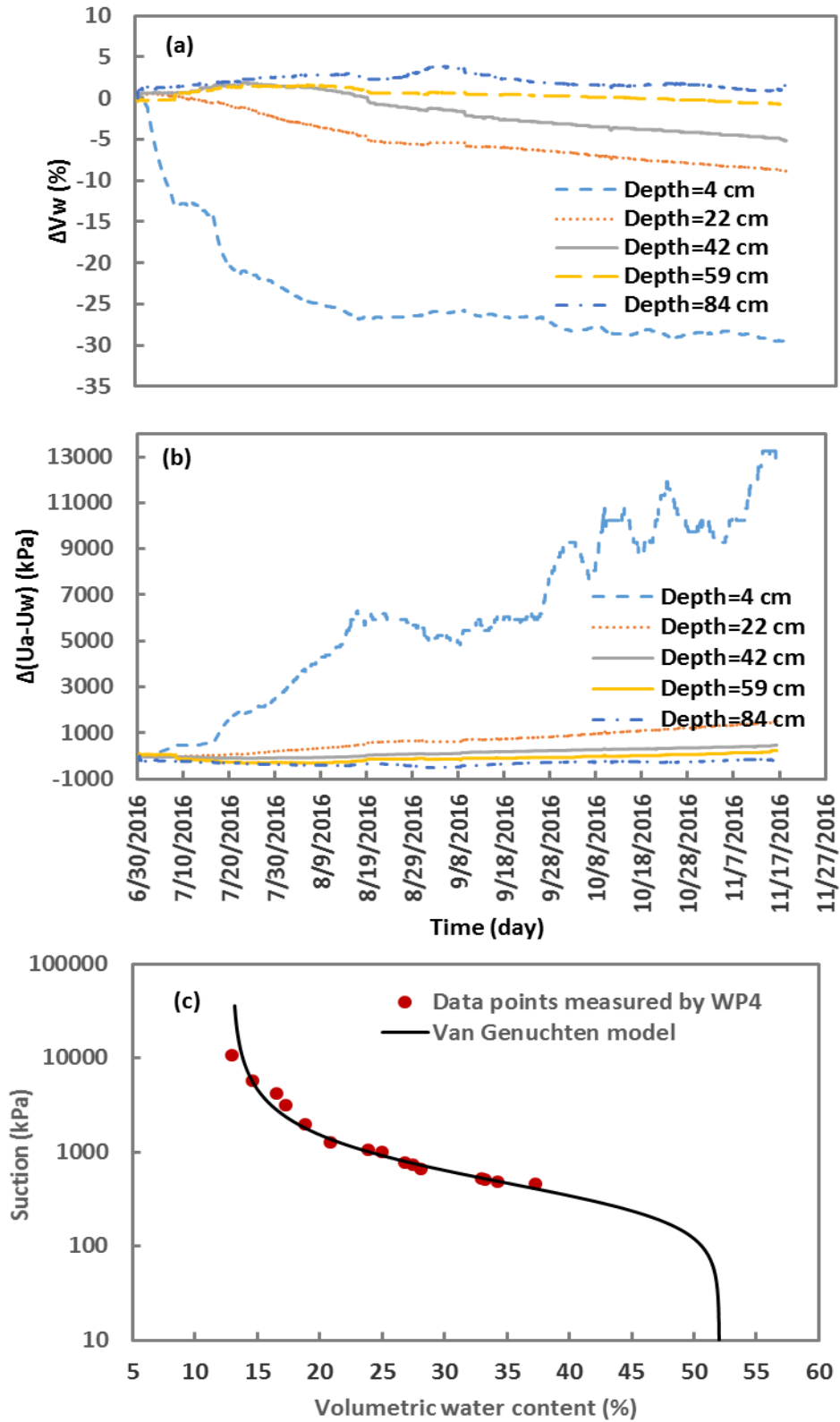


Figure 2.7. Volume water content changes during desiccation in the desiccation box (a), suction changes of test soil (b) and Soil Water Characteristic Curve (SWCC) of test soil (c)

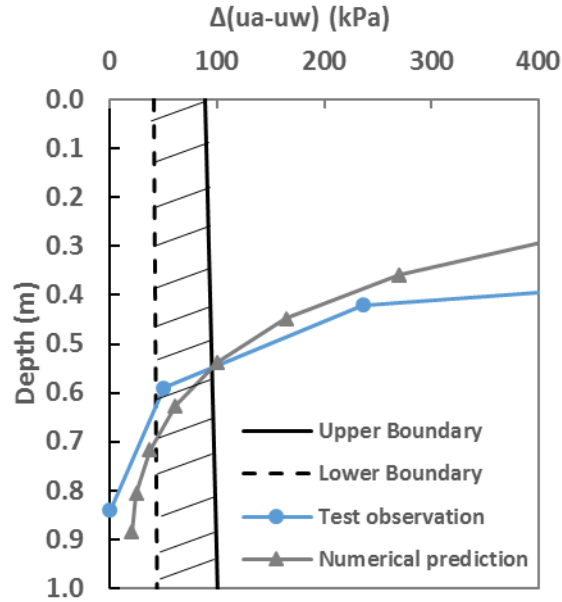


Figure 2.8. Suction changes versus depth of cracking according to equation 2.3

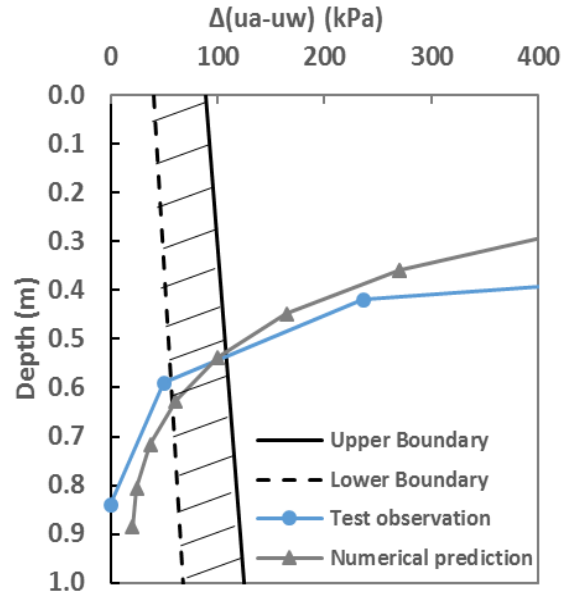


Figure 2.9. Suction changes versus depth of cracking according to equation 2.4

Table 2.2. Numerical parameters and assumptions

Parameter		Value	Determined by:
Young modulus (MPa)	E	10	measurement
Poisson's ratio	ν	0.35	estimation
Swelling coefficient for changes in suction (Mpa^{-1})	a_s	0.01	measurement
Porosity	n	0.35	measurement
Intrinsic permeability (m^2)	κ	$7.82\text{e-}15$	measurement

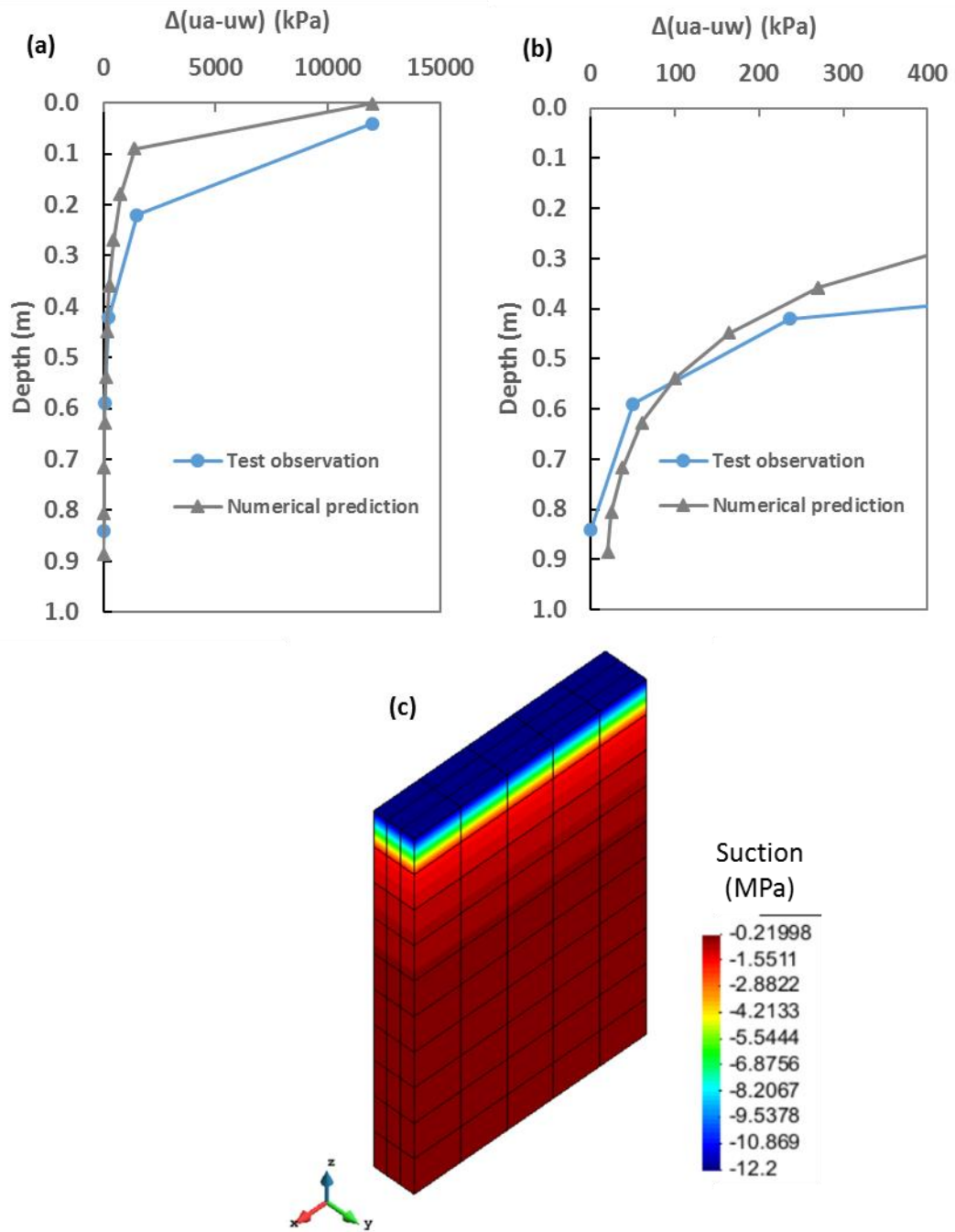


Figure 2.10. Calibrated suction changes through the depth of test soil using the numerical model, 0-12 MPa (a), 0-400 kPa, (b) color contours (c)



Figure 2.11. Desiccation crack depth measurement in the desiccation box, top view (a) side view (b)

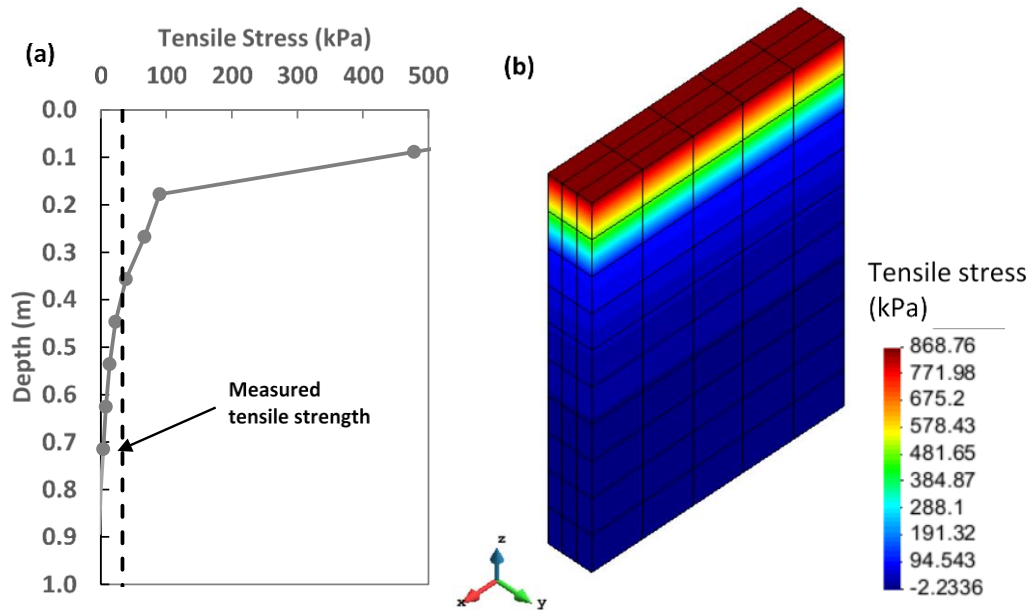


Figure 2.12. Tensile stress distribution curve (a) and color contours along soil profile using the numerical model (b)

The results of the numerical modeling suggest that the crack depth is around 40 cm based on the calibrated suction profile. For the same suction profile (gray line) in Figures 2.8 and 2.9, the analytical method indicates an average crack depth of about 57.5 cm as indicated by the intersection of the shaded boundary and gray trend line. Generally speaking, both the analytical and numerical model predictions of desiccation crack depth compared favorably to the observed crack depth in the desiccation box experiment.

2.5 Modeling the impact of desiccation cracks on unsaturated seepage of soil layer

The hydraulic behavior of a cracked soil is different from that of an intact soil. An unsaturated permeability function and water retention curve are required for the seepage analysis of an unsaturated soil mass. The discrete cracks model and the

equivalent permeability method for the cracked soil layer are employed to investigate the impact of desiccation cracks on unsaturated seepage analysis of a compacted clayey soil. Results of these two methods are compared and calibration procedures are suggested for using the equivalent permeability approach. The two methods are described below.

2.5.1 Modeling discrete cracks

To simulate a single crack or multiple cracks in a desiccated soil layer a finite element technique was proposed using the SVFLUX finite element program developed by Soil-Vision Systems Ltd. (2012). The proposed technique is based on the fragmentation of the finite element mesh (i.e. intact soil) and the insertion of additional elements (i.e. single cracks) between the finite element mesh. The intact soil properties in terms of the permeability function and water retention curve required for the seepage analysis are obtained based on the standard test methods and the relevant relationships. The soil water characteristic curve (SWCC) and the saturated permeability are the parameters required to form the unsaturated permeability function. The SWCC used for the seepage modeling was obtained from chilled mirror and axis translation methods. The permeability function and water retention curve required for the seepage analysis for the additional elements or single cracks were determined based on the procedure described below.

The SWCC for a single crack was estimated according to the air-entry value using the capillary theory as follows:

$$(u_a - u_w) = T_s \left(\frac{1}{R_1} + \frac{1}{R_2} \right) \quad (2-8)$$

where, T_s is surface tension of water, R_1 is the width of a single crack, and R_2 is assumed to be infinity. By knowing the air-entry value and assuming a nearly vertical slope from saturated volumetric water content to residual one (Wang and Narasimhan, 1985), SWCC of a single crack can be plotted as shown in Figure 2.13. The saturated permeability of a single crack was estimated from the following equation based on Barton's law.

$$k = e^2 \frac{\rho g}{12\mu} \quad (2-9)$$

where: e is the hydraulic width of the crack (the hydraulic aperture), μ , ρ , and g are dynamic viscosity of water, density of water, and acceleration due to gravity, respectively. The hydraulic aperture (e) has an experimental relationship with the mechanical aperture (E) and the joint roughness coefficient (JRC) as follows:

$$e = (JRC^{2.5}) / \left(\frac{E}{e}\right)^2 \quad (2-10)$$

Note that the equation is just valid for $E \geq e$ and the units for "E" and "e" are micrometer. JRC is a measure of surface roughness with ranges between zero to 20. The smooth planar surfaces have a JRC value of zero while apertures with the extremely rough surfaces have a JRC value of 20 (Barton et al. 1985). By assuming JRC equal to 5 and unity for the mechanical aperture to hydraulic aperture ratio (E/e), the saturated permeability coefficient for a single crack in this study was obtained equal to 2.6×10^{-4} m/s. The estimated single crack permeability appeared reasonable compared with that developed in another study (e.g. Khandelwal 2011). The saturated permeability for the intact soil was assumed to be 1.44×10^{-8} m/s, which was the average permeability

determined from lab testing for the soil used in the slope stability analysis. The Leong and Rahardjo (1997) and van Genuchten (1980) estimation methods available in SVFLUX were used to develop the permeability function based on the saturated permeability and SWCCs (Figure 2.13) for a single crack and intact soil, respectively, as shown in Figure 2.14.

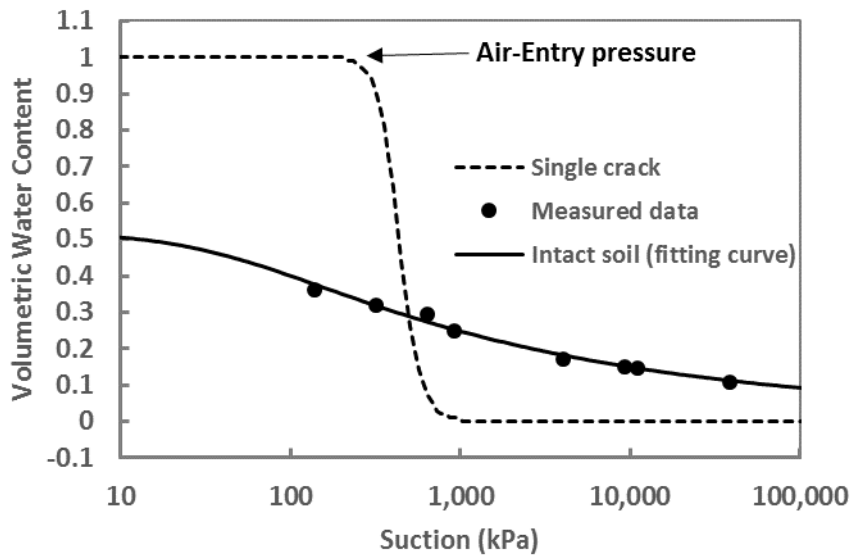


Figure 2.13. Soil Water Characteristic Curve (SWCC) for single crack and intact soil

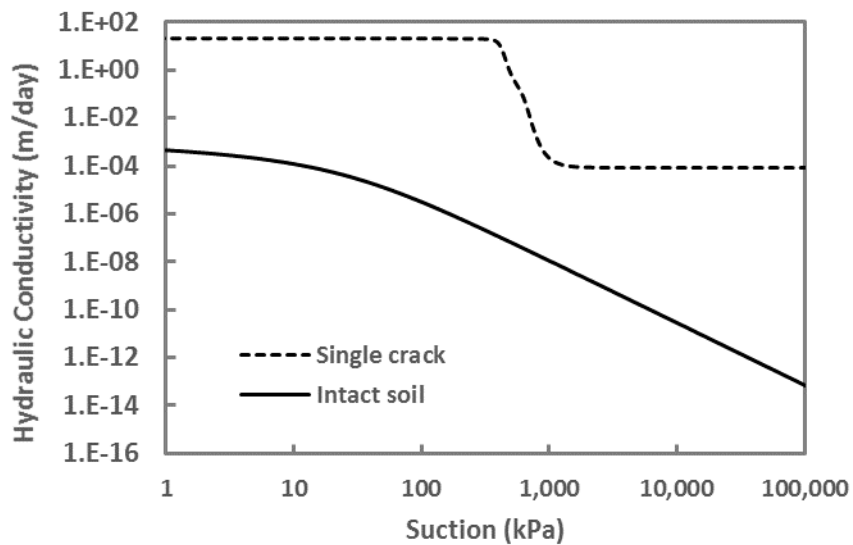
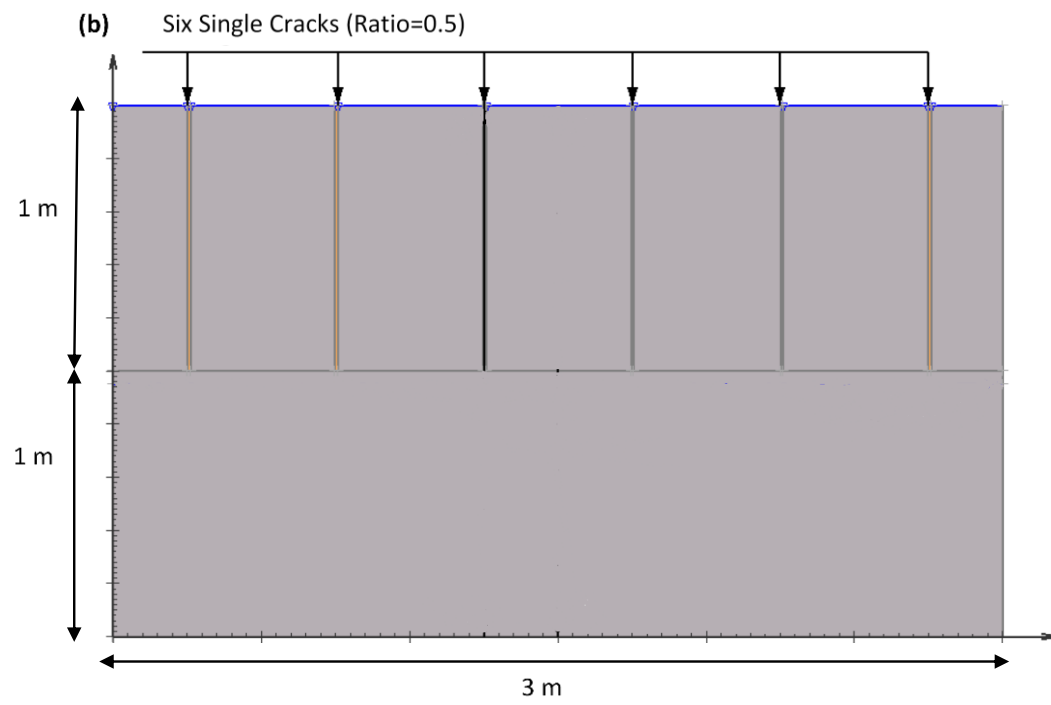
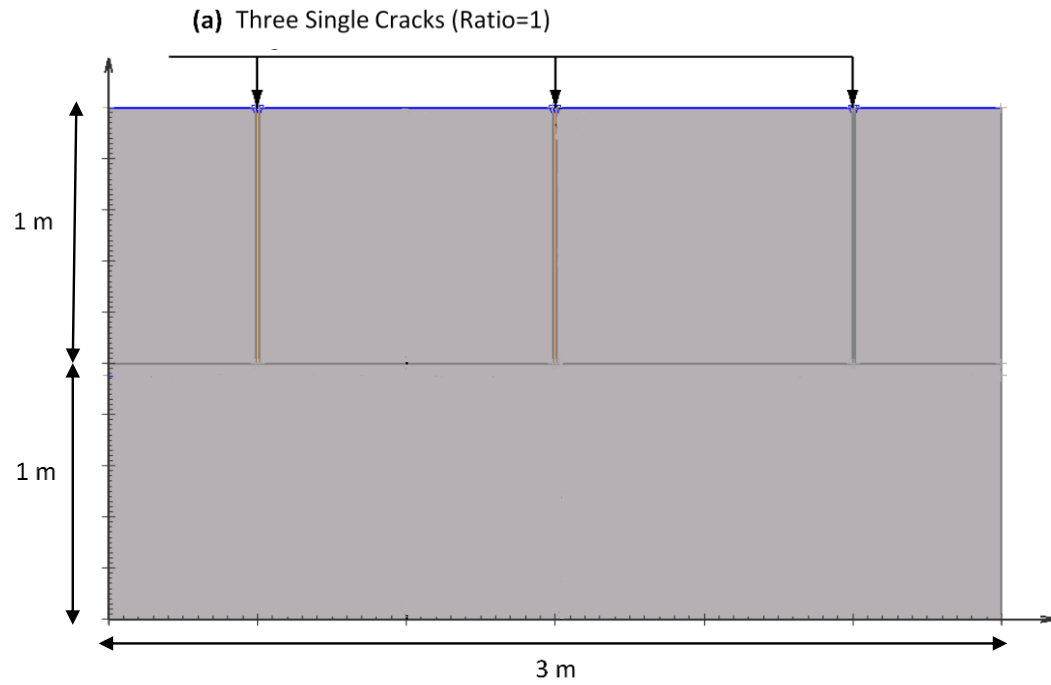


Figure 2.14. Hydraulic conductivity function for single crack and intact soil

A series of finite element models with single cracks was used to evaluate the hydraulic properties of cracked soil using the proposed method. A temporal change of pore water pressure from negative value (unsaturated or initial condition) to zero value (saturated condition) for a given time was used as a climate boundary condition on the top of the model. The numerical simulations were designed to have a different number of cracks distributed in a cracked layer. The cracked layer was placed on the top of the intact layer to calculate the water seepage through the depth of the intact and cracked layers. The entire width and height of the cracked soil layer were 3 m and 1 m, respectively. The width and height of the single cracks were 0.001 m (1 mm) and 1 m, respectively. Ratios of crack spacing to crack depth equal to 1, 0.5, and 0.25 were chosen as alternatives for the parametric study. Figures 2.15(a) to (c) show the geometry of models for the seepage analysis.



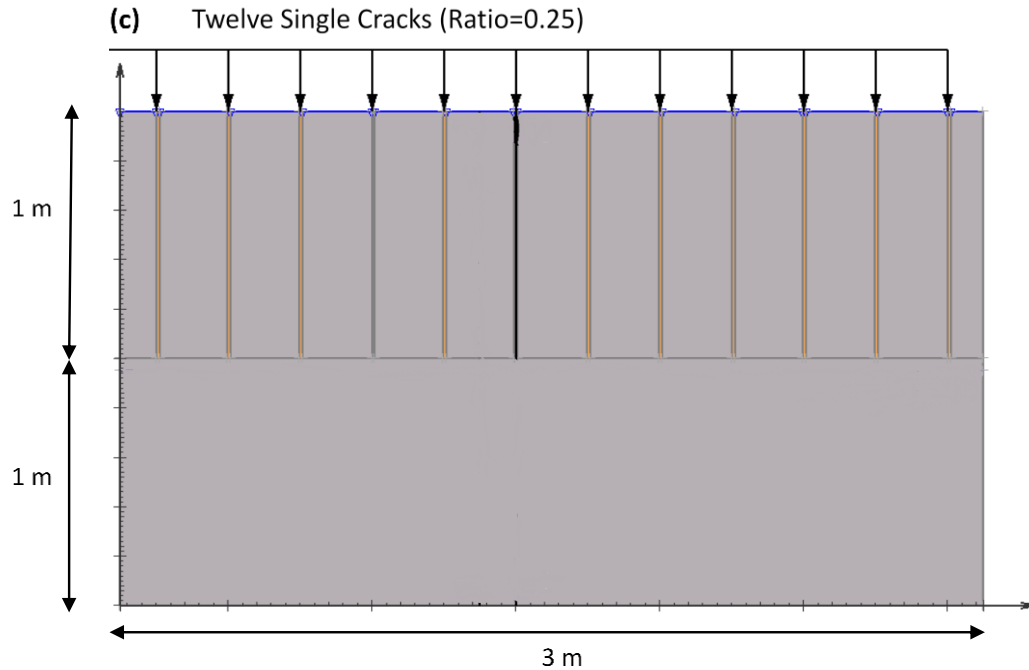


Figure 2.15. Geometry of a cracked soil considering single cracks with a ratio of crack spacing to crack height equal to (a) 1, (b) 0.5, (c) 0.25

2.5.2 Modeling using the equivalent hydraulic conductivity approach

To avoid a time-consuming procedure of finite element modeling with discrete cracks in the mesh, the use of an equivalent coefficient of permeability was proposed (Fredlund et al. 2010) based on the concept of water flow parallel to the soil layers. It was assumed that the cracked layer includes an intact soil and multiple cracks, which were parallel to each other. If the permeability and thickness of each layer were specified, then the equivalent permeability would be obtained from the following equation.

$$k_{eq} = \frac{k_{in}d_{in} + k_{cr}d_{cr}}{d_{in} + d_{cr}} \quad (2-11)$$

where, (k_{cr}, d_{cr}) and (k_{in}, d_{in}) are coefficient of permeability and thickness of single cracks and intact soil, respectively. The development of this equation assumes the flow of water is parallel to the cracks.

The above saturated equivalent permeability associated with a combined SWCC proposed by Fredlund et al. (2010) was employed to develop a permeability function for the cracked layer as shown in Figure 2.16. Thus, the problem illustrated in Figure 2.17 can be modeled using the equivalent permeability approach by replacing the layer with discrete cracks with a layer having an equivalent permeability that accounts for the cracks. The equivalent permeabilities were obtained as 2.75×10^{-7} , 5.35×10^{-7} , and 1×10^{-6} m/s corresponding to the ratios of crack spacing to depth of 1, 0.5, and 0.25, respectively. The two methods can then be compared and analyzed for different boundary and soil conditions. Further, a method for calibrating and refining the equivalent permeability method can be developed based on the comparison of results of the two methods.

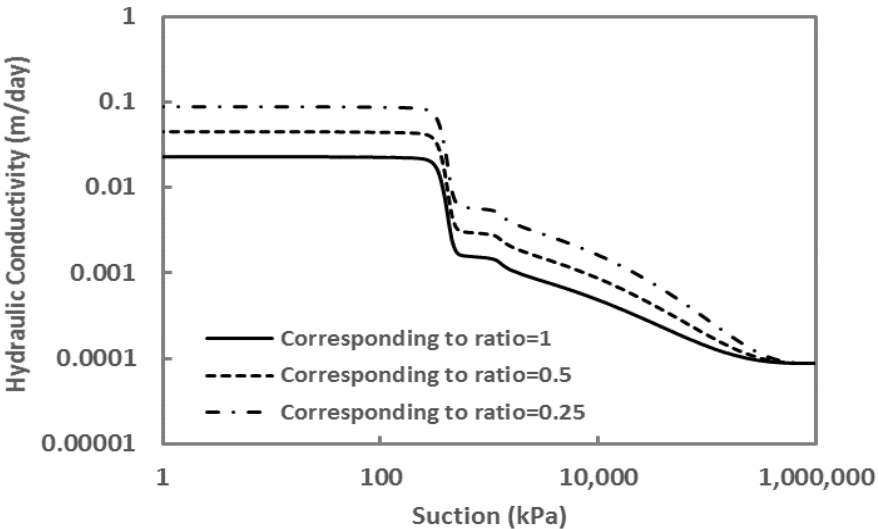


Figure 2.16. Hydraulic conductivity function for a cracked layer

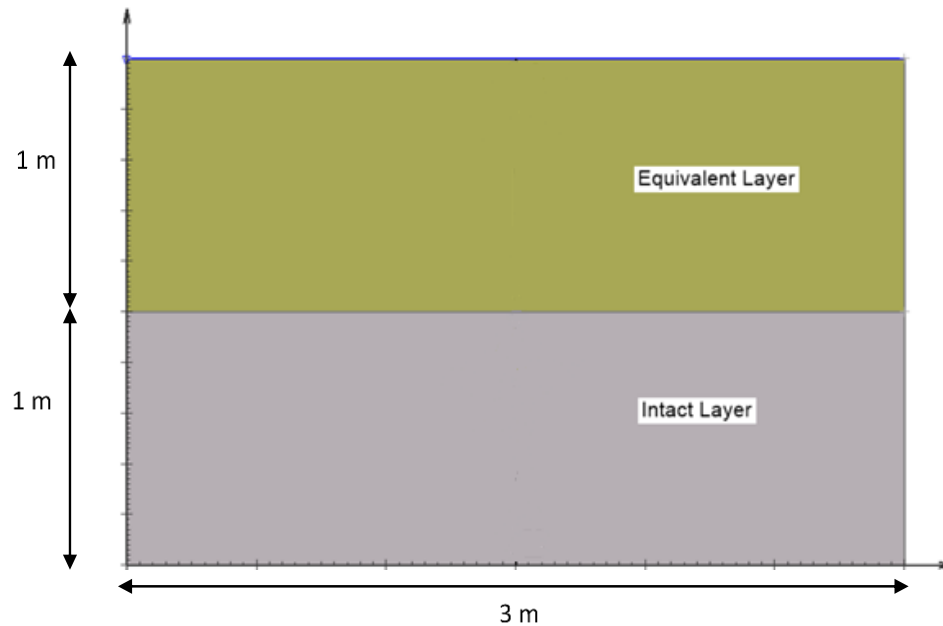


Figure 2.17. Geometry of a cracked soil considering equivalent layer

2.5.3 Comparison of discrete crack and equivalent layer modeling results

A transient seepage analysis was conducted by applying a sudden increase of pore water pressure from minus 200 kPa (assumed initial condition of the model) to a saturated condition or zero water pressure on the surface of a cracked layer and the water seepage within the depth of model was modeled for ten days. The results of seepage analysis within the depth of the model after ten days are shown in Figures 2.18, 2.19 and 2.20 for different crack spacing to depth ratios. In these figures, the pore water pressure contours on the left represent the discrete crack model while the contours on the right represent the equivalent cracked layer model. The blue and brown contours represent positive and negative pore water pressures, respectively. The graphical results in the figures compare the pore water pressure distribution through the depth of the model. The results show that the pore water pressure changes beneath the single cracks

were greater than beneath the intact layers, as expected. This difference reduced as the crack spacing to depth ratios decreased as seen when comparing the pore water pressure plots of Figures 2.18, 2.19 and 2.20. By comparing the results, it is seen that the pore water pressure changes obtained from discrete crack model and the equivalent cracked model are in better agreement when the crack spacing to depth ratio decreases.

In addition to the crack spacing to depth ratio, it was desired to evaluate the influence of the crack width in the discrete crack model, as well as the ratio of the permeabilities between: 1) a crack and intact soil in the discrete crack model, and 2) the equivalent cracked layer and the intact soil layer in the equivalent cracked model. The effect of crack width on the amount of water flow at the interface is shown in Figure 2.21. An increase of 11% to 38% for water flow can be seen due to a change of crack width from 1 to 10 mm. In Figure 2.22 the effect of elapsed time of infiltration and ratio of cracked to intact soil permeability on the pore water pressures for a point close to the interface between cracked and uncracked layers is shown. This point was located at 10 cm below the interface between cracked and intact layers.

The time to reach saturation at point near the interface between the cracked and uncracked zones was investigated for different ratios of cracked to intact permeability for the condition where the ground surface was maintained in a saturated state (pore water pressure set equal to zero). For this purpose, single cracks with a width of 1 mm and a crack spacing equal to the crack depth (ratio=1) were used. As expected, the rate to reach saturation near the interface was faster when the equivalent permeability method was compared to the single crack method as shown in Figures 2.22

and 2.23. At low ratios (e.g. 1.8 for the equivalent permeability model and 181 for the discrete crack model), the pore water pressure increased with increasing elapsed time from unsaturated condition. However, for the discrete crack model, the unsaturated condition (negative pore water pressure) existed even after 40 days. The saturated condition (close to zero pore water pressure) at a point located at 10 cm below the interface between the cracked and intact layers occurred after 10 days when the permeability ratio was 10,000 as shown in Figure 2.22. It can also be seen that even the high ratios were not effective for wetting the interface between the cracked and intact layers at the short-elapsed times (e.g. 1 and 2 days). For the equivalent permeability model as shown in Figure 2.23, the ratio above 100 was enough to reach a saturated condition or zero pore water pressure at the interface located at the given point. According to this transient seepage analysis, the computed permeability ratios equal to 181 and 181×10^3 for the equivalent permeability model and the discrete crack model, respectively, were the best estimates to reach the saturated condition beneath the interface layer.

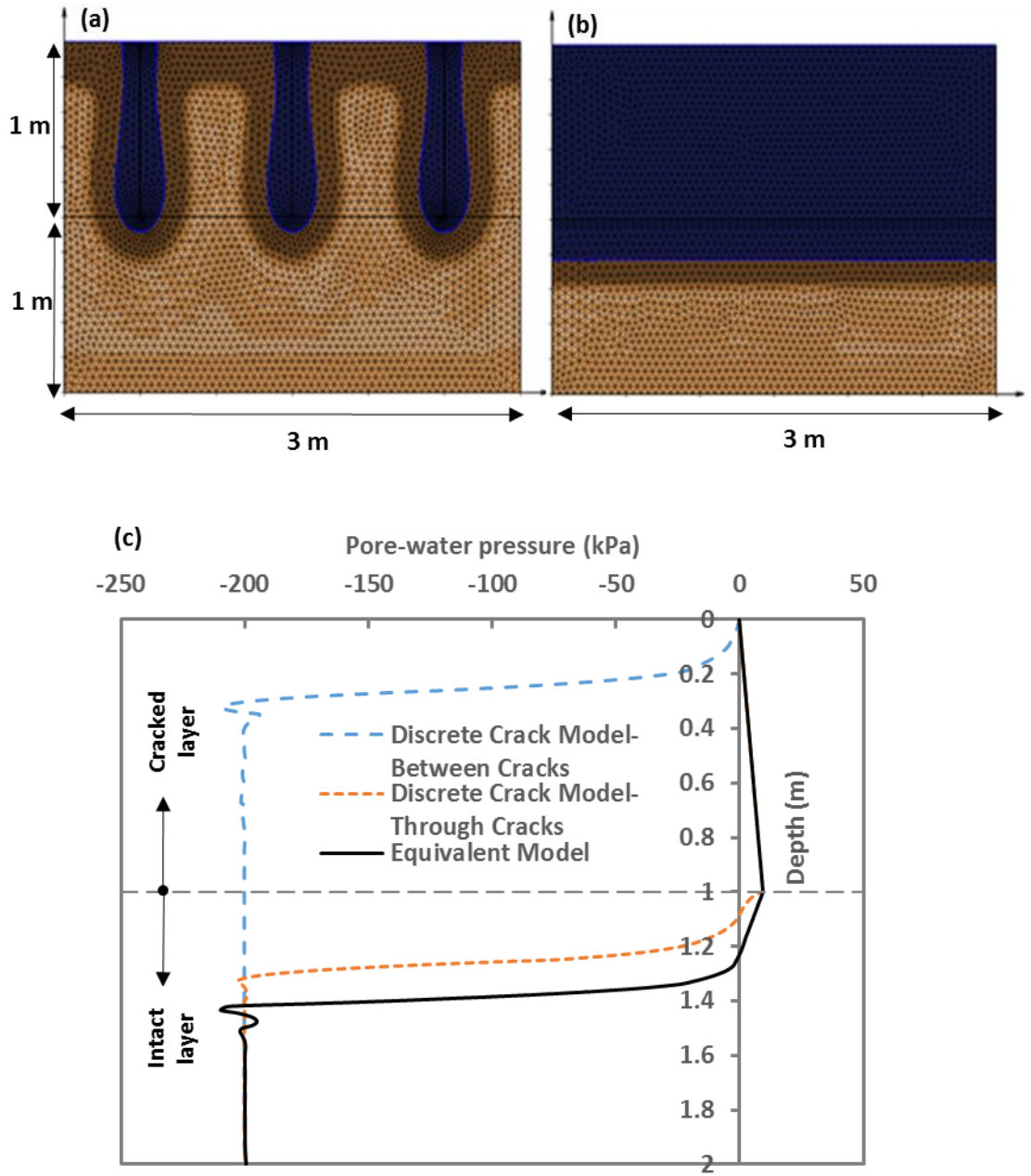


Figure 2.18. Pore water pressure distribution within cracked and intact layers (ratio of crack spacing to crack depth=1) for Discrete crack model (a), Equivalent layer model (b), and both models (c)

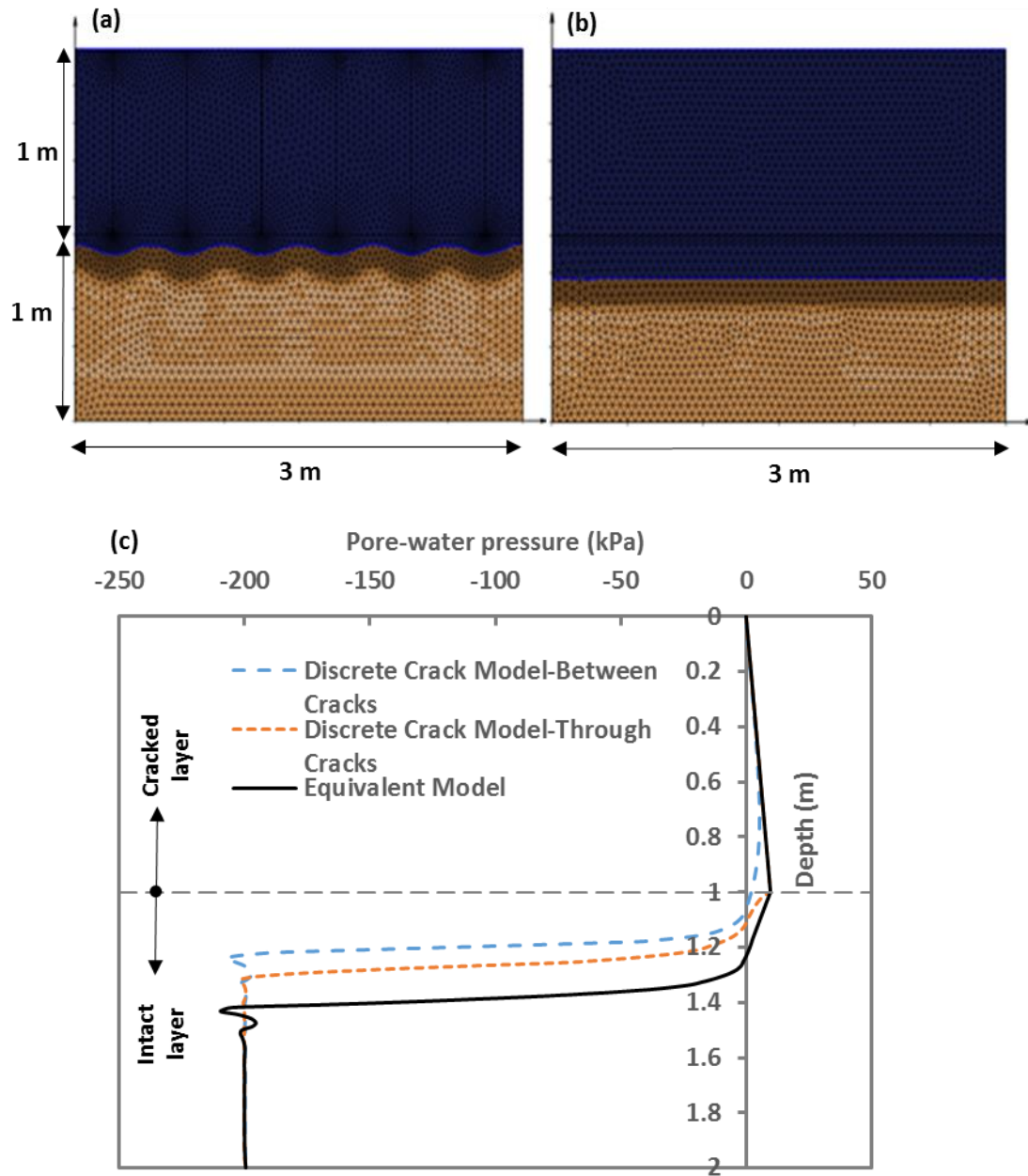


Figure 2.19. Pore water pressure distribution within cracked and intact layers (ratio of crack spacing to crack depth=0.5) for Discrete crack model (a), Equivalent layer model (b), and both models (c)

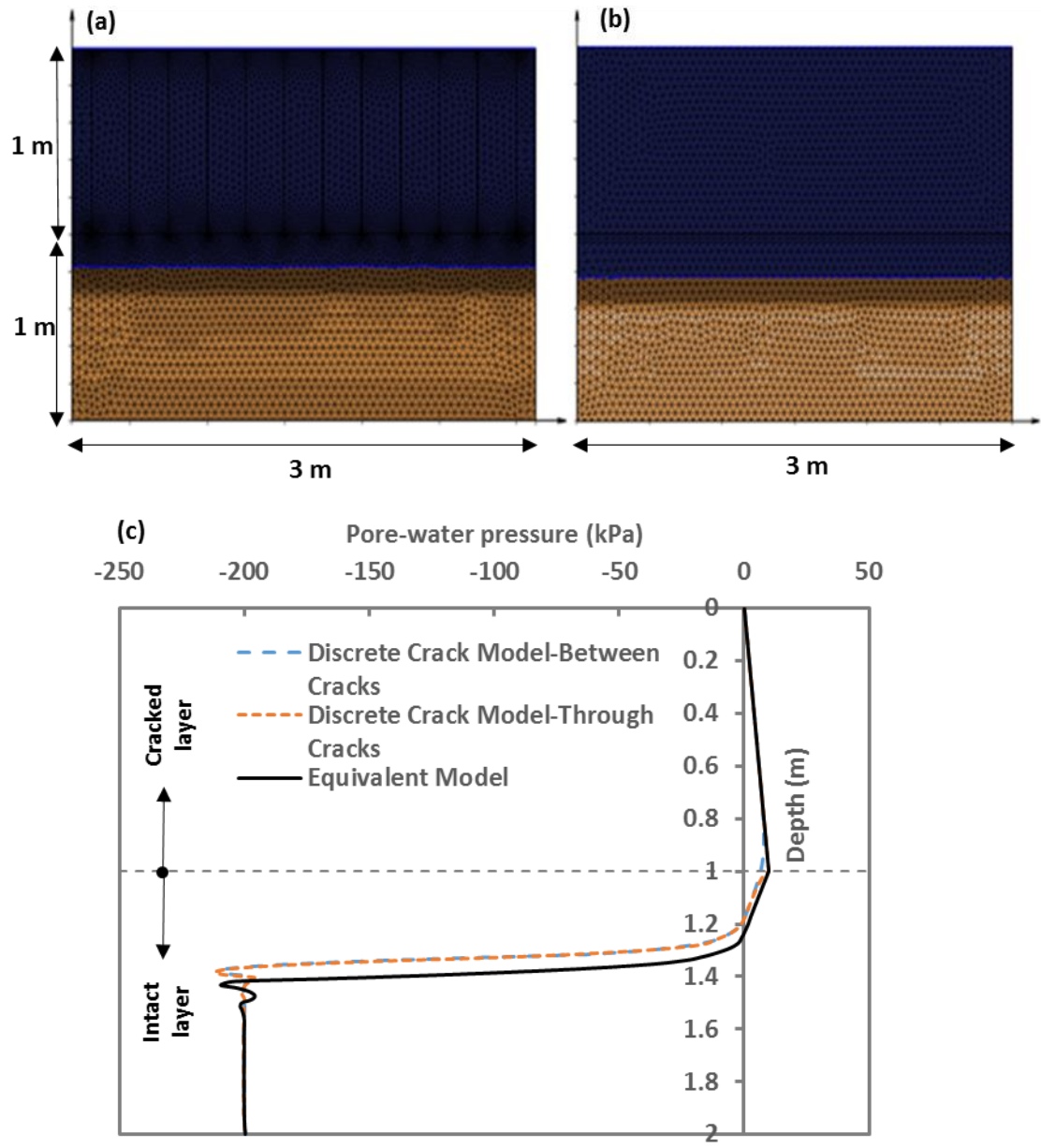


Figure 2.20. Pore water pressure distribution within cracked and intact layers (ratio of crack spacing to crack depth=0.25) for Discrete crack model (a), Equivalent layer model (b), and both models (c)

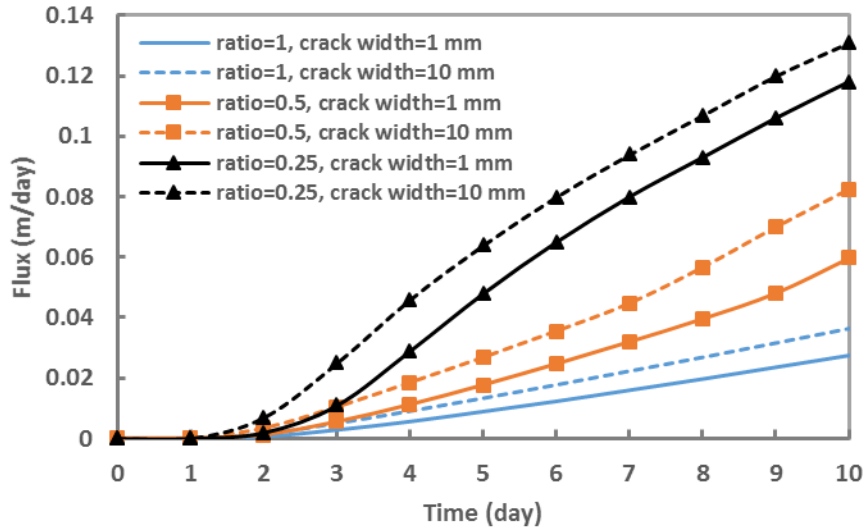


Figure 2.21. Effect of crack width on flow of water at interface between cracked and intact layers

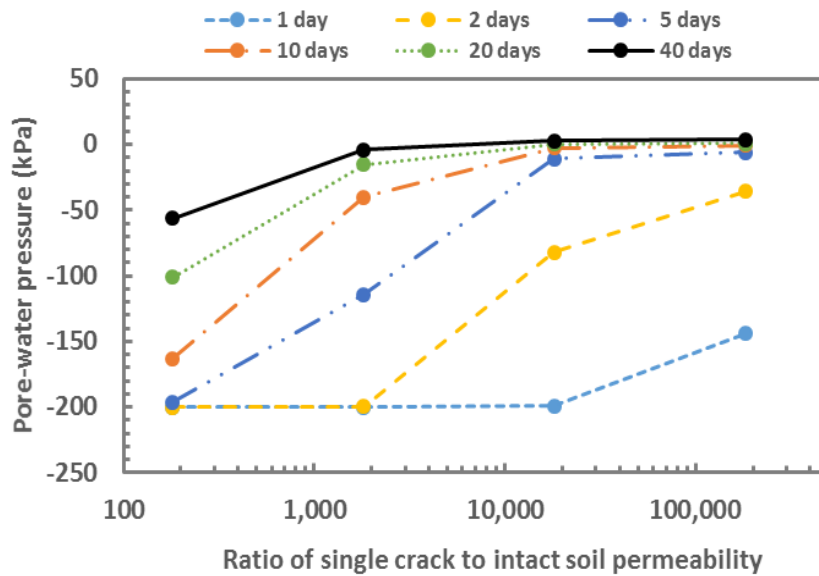


Figure 2.22. Effect of ratio of single crack to intact soil permeability on pore water pressures at a point located at 10 cm below the interface at different elapsed time

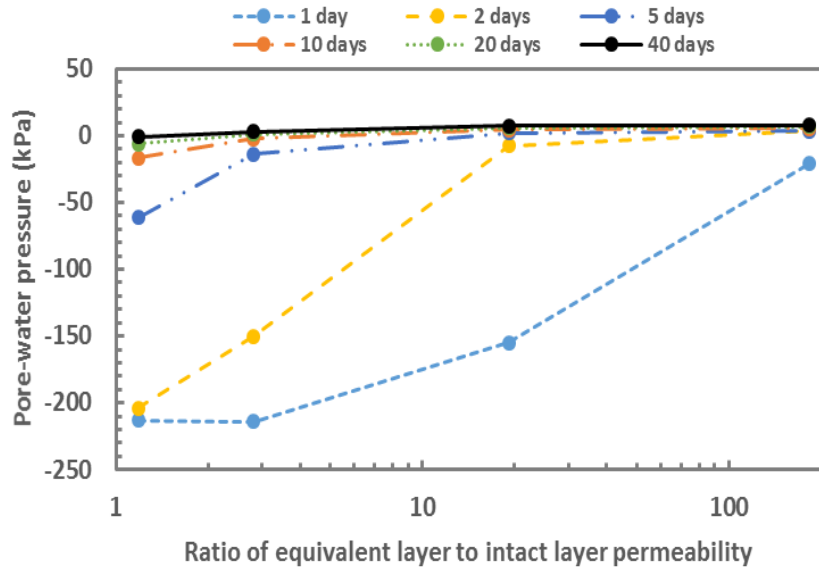


Figure 2.23. Effect of ratio of equivalent cracked layer to intact soil permeability on pore water pressures at a point located at 10 cm below the interface between cracked and intact layers at different elapsed time

2.6 Impact of desiccation cracks on unsaturated seepage and stability of slope

2.6.1 Site selection and soil physical properties

The shallow slope analyzed in this research was located in Chickasha, Oklahoma and was the focus of extensive monitoring for a period about two years. This slope was part of a roadway embankment that had recurring shallow failures. The bedrock geology of this region was classified as middle Permian age and mostly consists of red-brown silty shale with some fine-grained sandstone, and the overlying soil was primarily medium to highly plastic clay. The test soil used for the analysis possessed a liquid limit (LL) of 38%, plastic limit (PL) of 20%, plasticity index (PI) of 18%, and 89% of fines. From a standard compaction test, the maximum dry unit weight was 17.3 kN/m^3 and optimum water content was 18.0 %. The specific gravity of soil solids was 2.75.

2.6.2 Mechanical and hydraulic properties of soil

Mechanical and hydraulic tests were conducted to obtain strength parameters and permeability values to employ in slope stability analyses. Shear strength of soil in saturated and unsaturated conditions are required to analyze the stability of the slope. Crack depths were predicted using the method described previously. The saturated permeability was determined by laboratory testing and was used to estimate the unsaturated hydraulic conductivity function for unsaturated seepage analysis.

2.6.2.1 Unsaturated/saturated shear strength testing

A series of saturated and unsaturated tests on the soil resembling the initial field condition were conducted using the modified and conventional direct shear apparatuses for the slope stability analysis. The direct shear apparatus modified by

Hamid (2005) at OU was used to conduct unsaturated shear tests. The conventional small-scale direct shear device was used for measuring the saturated shear strength parameters. The results of unsaturated and saturated shear tests are shown in Figures 2.24 and 2.25.

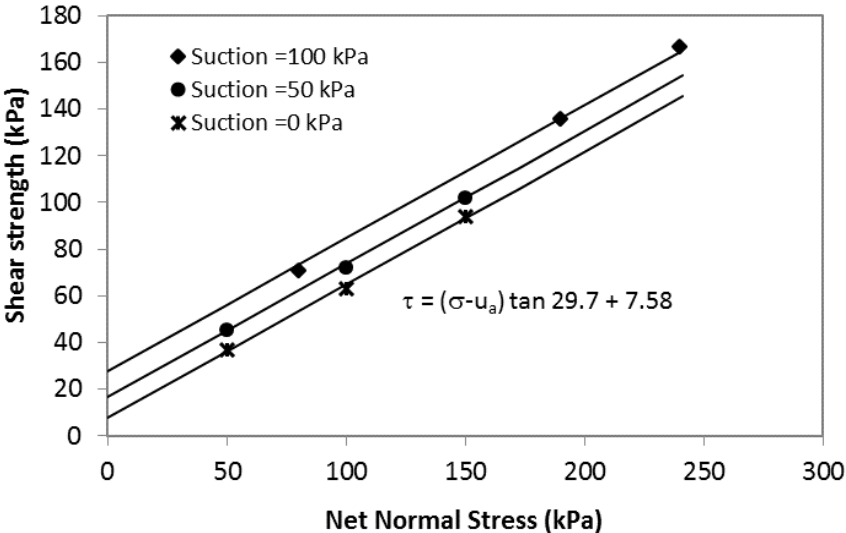


Figure 2.24. Shear strength evolution under different net normal stresses and matrix suctions

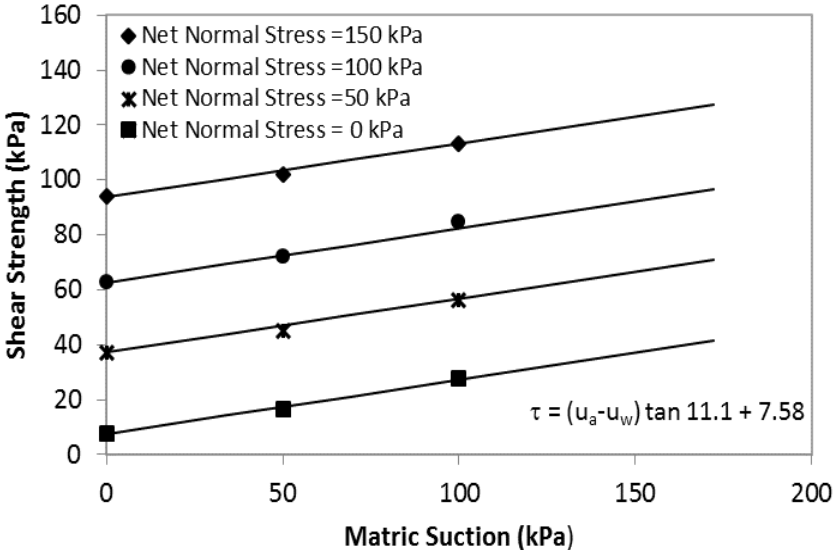


Figure 2.25. Shear strength evolution under different matrix suctions and net normal stresses

2.6.2.2 Saturated hydraulic conductivity testing

To determine the saturated hydraulic conductivity of the soil under study, Shelby tube samples were tested as well as remolded samples prepared at maximum dry unit weight with optimum water content. The standard test method for measurement of hydraulic conductivity of saturated materials with a flexible wall permeameter was used as described in ASTM D5084-10.

Permeability test results are summarized in Table 2.3.

Table 2.3. Summary of saturated hydraulic conductivity values

Depth (cm)	γ_d (kN/m ³)	Effective Confining Stress (kPa)	Hydraulic Gradient	Saturated Hydraulic Conductivity (cm/sec)
35-65	14.3	35	21.5	2.82e-6
65-120	15.6	35	22.3	8.50e-7
Compacted	17.3	35	13.3	6.42e-7

2.6.3 Unsaturated seepage analysis considering a cracked layer

Unsaturated seepage analysis was implemented using an atmospheric loading condition on the ground surface of the Chickasha slope. The initial condition of the slope in terms of soil moisture content was similar to the initial readings from three volumetric moisture content sensors located at depths of 0.3, 0.9, and 1.8 m from the ground surface. The moisture contents for the deeper layers were assumed to be close to saturated moisture content. The initial moisture distribution is shown in Figure 2.26 based on the volumetric water content, which is the product of gravimetric water content and dry unit weight of the soil layer. In order to examine the effect of desiccation cracking on the seepage of water, the slope was divided into two layers (cracked and intact) using the crack depth estimation. A cracked layer with a thickness

equal to the desiccation crack depth obtained from the analytical and numerical models (Appendix A) was specified on the upper part of the slope, which was extended from the crest to the toe of the slope. The rest of layers of the slope were specified as intact soil with original properties. An application of the discrete crack model and the equivalent permeability method for the cracked layer was examined in a seepage analysis of the Chickasha slope using the SVFLUX finite element program. A ratio of crack spacing to crack depth equal to 1 was assumed to consider the impact of desiccation cracks on the seepage analysis. This assumption was based on the crack pattern observed in the field by other researchers (Knight 1971 and Elias et al. 2001). The saturated permeability of the single crack and equivalent layer were assigned to be 2.6×10^{-3} and 2.6×10^{-6} m/s for the seepage analysis, respectively. These values were obtained based on the transient seepage analysis of the simple model discussed in section 2.5.3. A real boundary condition including a combination of rainfall and evaporation was specified on the slope surface. Input data for the analysis was collected from the weather station installed at the Chickasha slope (from Aug. 2012 to Jun. 2014). The location of weather station was close to the crest of the slope. The captured data from the local weather station were supplemented, where data errors or missing data occurred, using nearby Oklahoma Mesonet data (Chickasha Station). Input weather data are shown in Figures 2.27 and 2.28. The potential evaporation (PE) and actual evaporation (AE) were used based on the Penman (1948) and Wilson-Penman (1994) equations to determine net infiltration at the boundary under atmospheric loading. The net solar radiation required for the

equations was obtained from the total radiation, which was already collected from the weather station, according to the equation proposed by Irmak et al. (2003).

The actual and predicted moisture variations at the depth closest to the ground surface (e.g. 0.3 m) show greater fluctuations than the deeper layers as shown in Figure 2.29. This is consistent with the expectation that the surface layers are more influenced by the seasonal climate than the deeper layers.

As shown in Figure 2.29, including the influence of cracks in the unsaturated seepage model, as opposed to assuming an intact surface layer, resulted in more rapid wetting of the soil and larger predicted moisture contents. Modeling the cracked layer with a higher equivalent permeability resulted in larger predicted moisture contents that were generally closer to the field values, compared to using the intact permeability, but did not capture the fluctuations observed in the field. The predicted moisture contents for the slope modeled with a set of single cracks was closest to those based on field measurements and better captured the fluctuations seen in the field values. This suggests that including discretely modeled cracks in an unsaturated seepage analysis can provide a realistic approach to estimating variations in moisture contents over time.

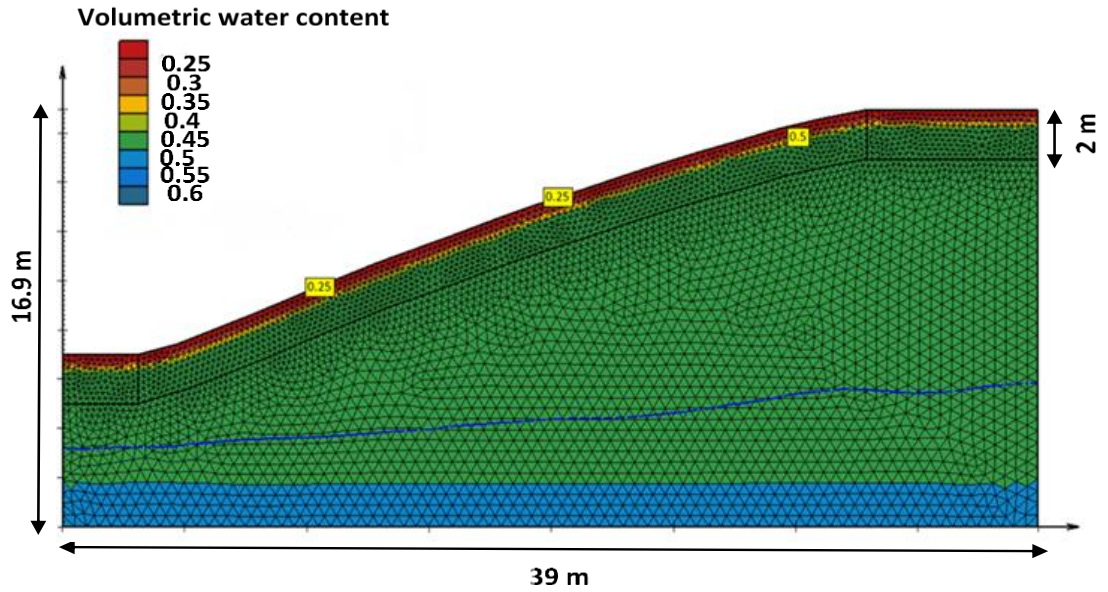


Figure 2.26. Initial volumetric moisture content distribution and geometry of Chickasha slope

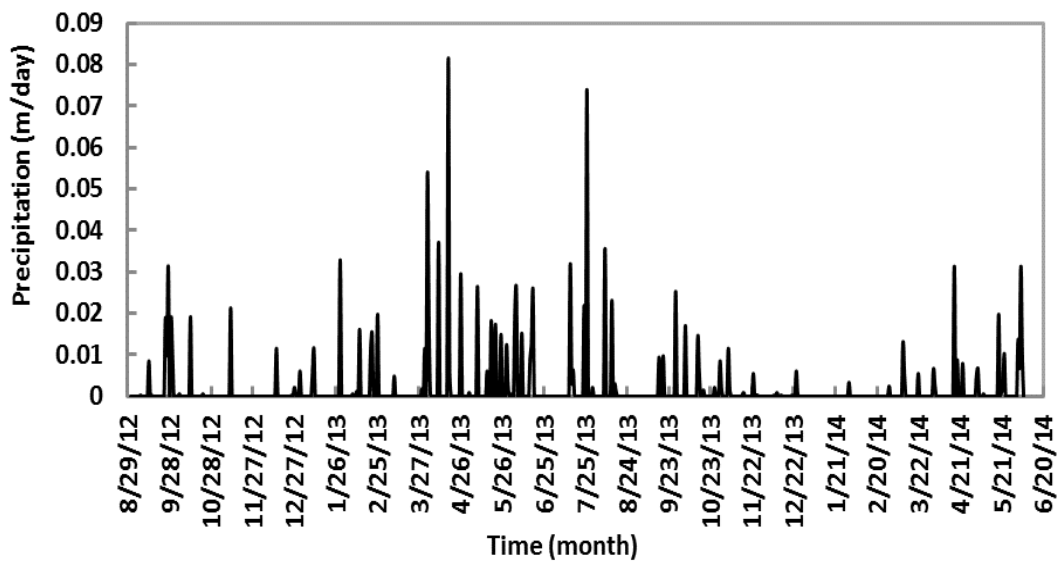


Figure 2.27. Rainfall data for Chickasha slope

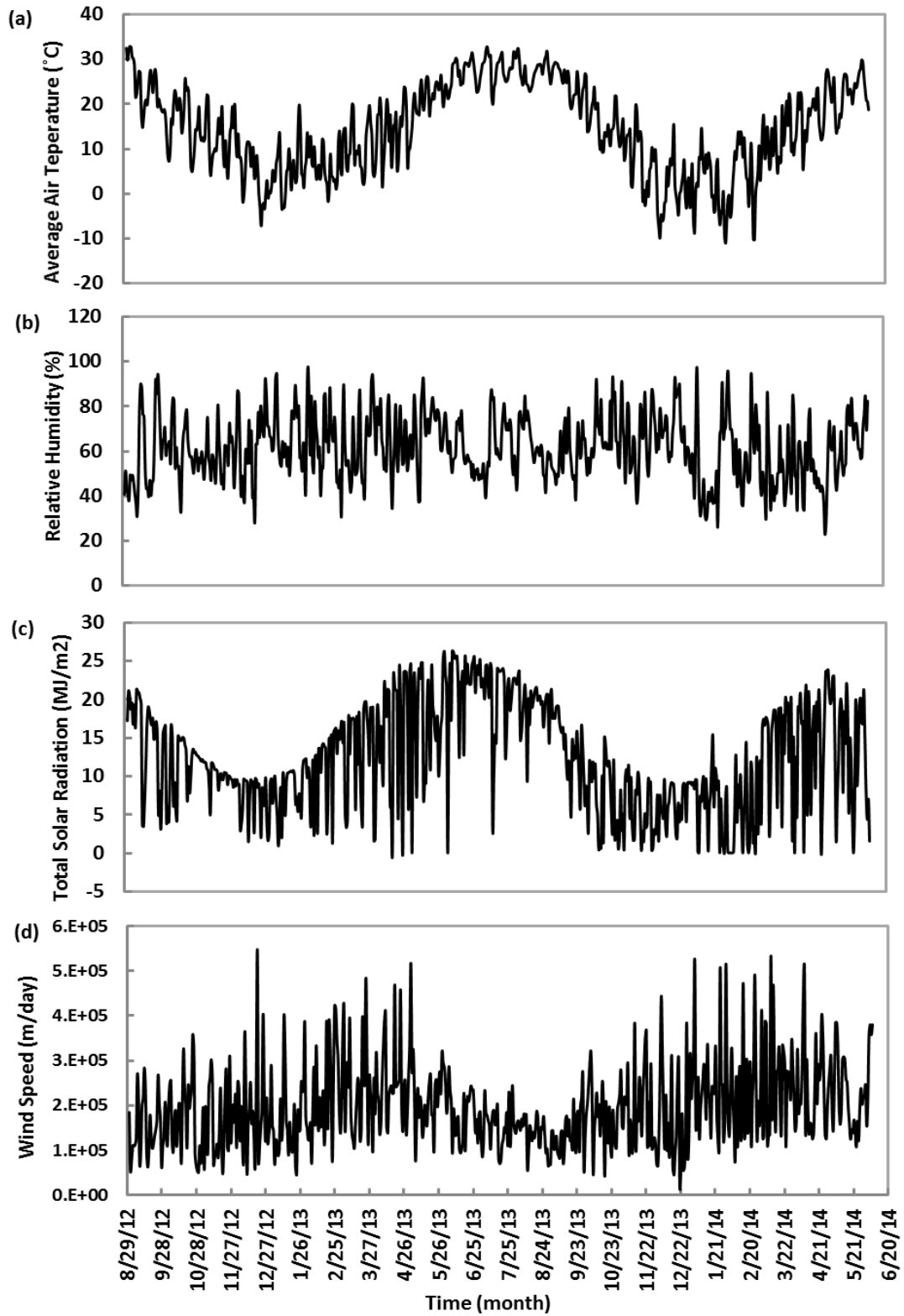


Figure 2.28. Evaporation data from Aug. 2012 to Jun. 2014, (a) relative humidity, (b) average air temperature, (c) total solar radiation, (d) wind speed

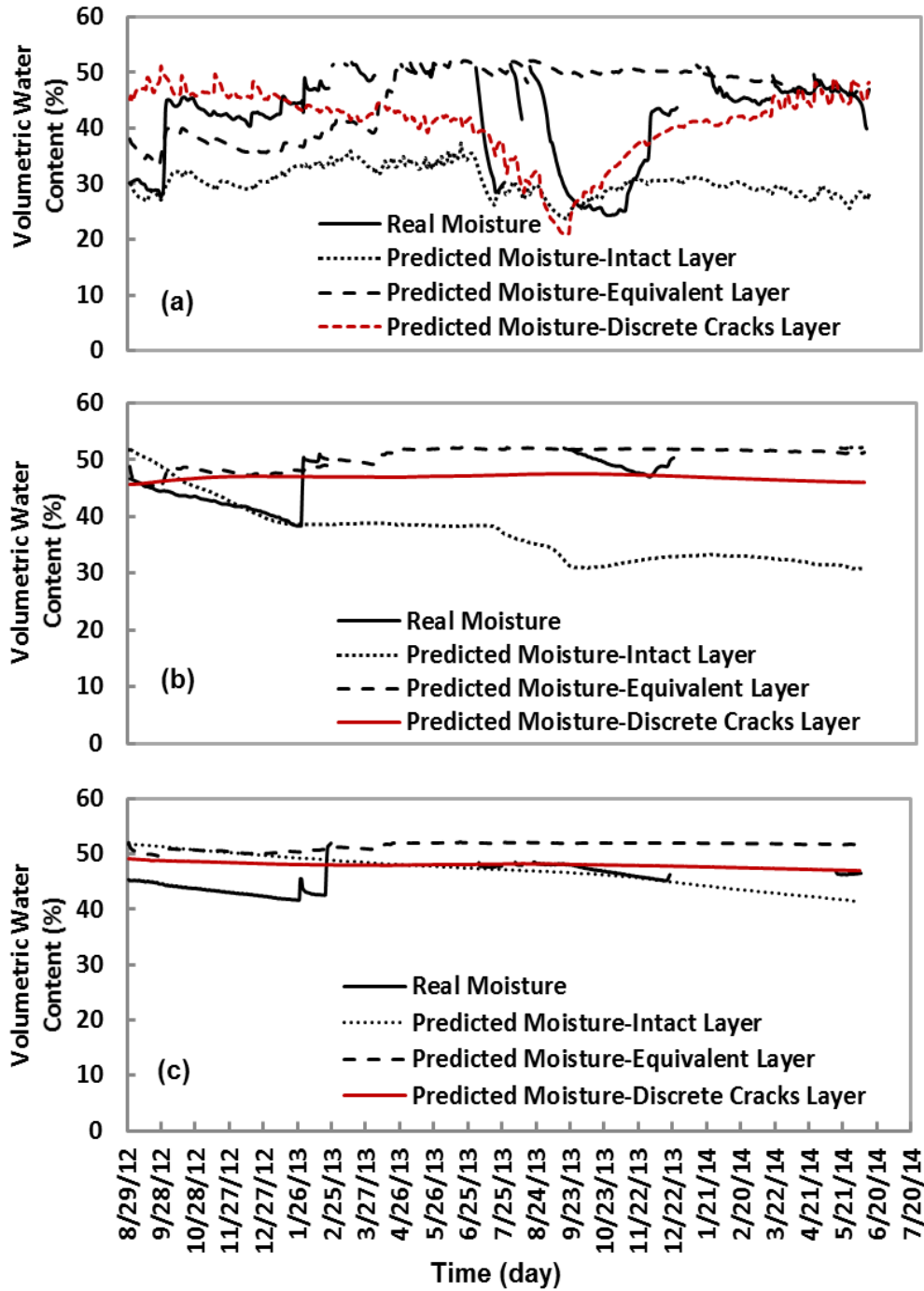


Figure 2.29. Measured and Predicted Soil Moisture Changes for Intact and Cracked Slope at Three Different Depths (a) 0.3 m, (b) 0.90 m, and (c) 1.80 m

2.6.4 Unsaturated slope stability analysis considering a cracked layer

Slope stability analysis was performed through the limit equilibrium method using the SVSLOPE program developed by SoilVision Systems Ltd. (2012). The results of slope

stability analysis using SVSLOPE provided a factor of safety based on the force or moment equilibrium on the slip surface. The factor of safety for slope stability analysis is defined as the ratio of the soil shear strength to the shear stress generated on the slip surface.

Pore water pressures predicted via unsaturated seepage analysis based on discrete cracks and equivalent layer models, as described above using weather data, were used in the slope stability analyses. Both positive and negative (suction) pore pressures were predicted, depending on seasonal weather variations, and included in the slope stability analysis. The effect of desiccation cracking on shear strength was simulated in the slope stability analysis by assuming the effective stress cohesion intercept of the cracked soil was zero. It has been suggested that shear strength of soil subjected to cycles of drying and wetting is simulated by normally consolidated conditions (Kayyal and Wright 1991) with zero cohesion.

The mechanical properties of the soil layers used for the slope and the geometry obtained from an optical survey measurement taken at the site are shown in Figure 2.30.

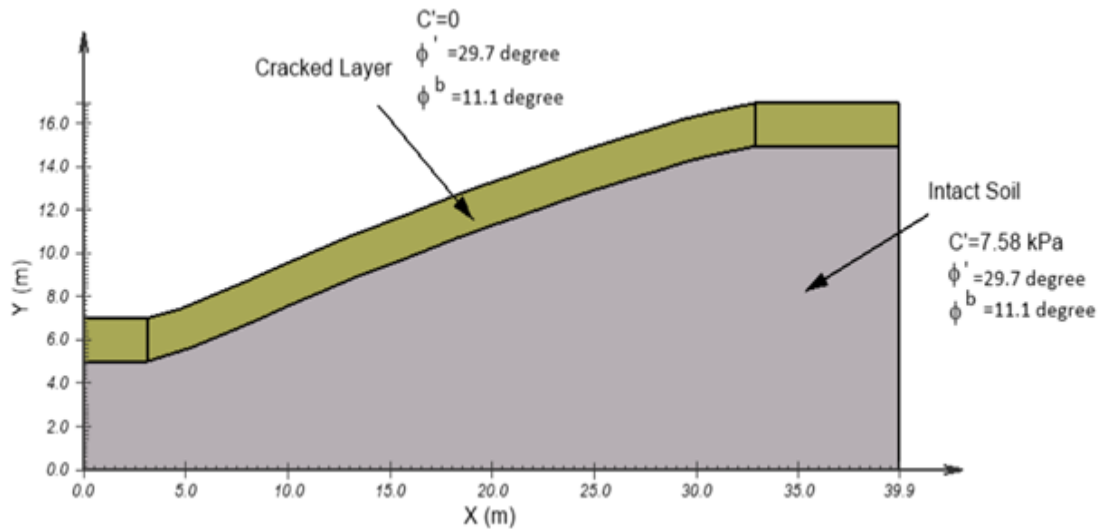


Figure 2.30. Geometry and mechanical properties of Chickasha embankment (slope)

The two variables that were varied in the analysis were the pore pressure distributions corresponding to the transient seepage analysis and the effective stress cohesion intercept (c').

Analyses were run using c' as determined from the laboratory direct shear tests and with c' equal to zero for the near surface soils in the analysis of both the cracked and uncracked slopes. To investigate the effect of only pore pressure distributions on the slope stability analyses the same strength parameters were used in both cracked and uncracked near surface soil layers.

The temporal variations of factor of safety for the intact slope and cracked slope using the two methods, including equivalent and discrete cracks method of unsaturated seepage modeling, are shown in Figure 2.31. The factor of safety for the slope where unsaturated seepage analysis was modeled without cracks, is shown for comparison. In Figure 2.31, the minimum factor of safety was achieved when the pore pressures in the slope were predicted using the equivalent permeability model for the cracked layer.

Temporal variations of factor of safety indicate that stability analysis of a cracked slope with the concept of equivalent layer can result in the critical condition for the slope, which is the sliding failure of slope based on the field observations.

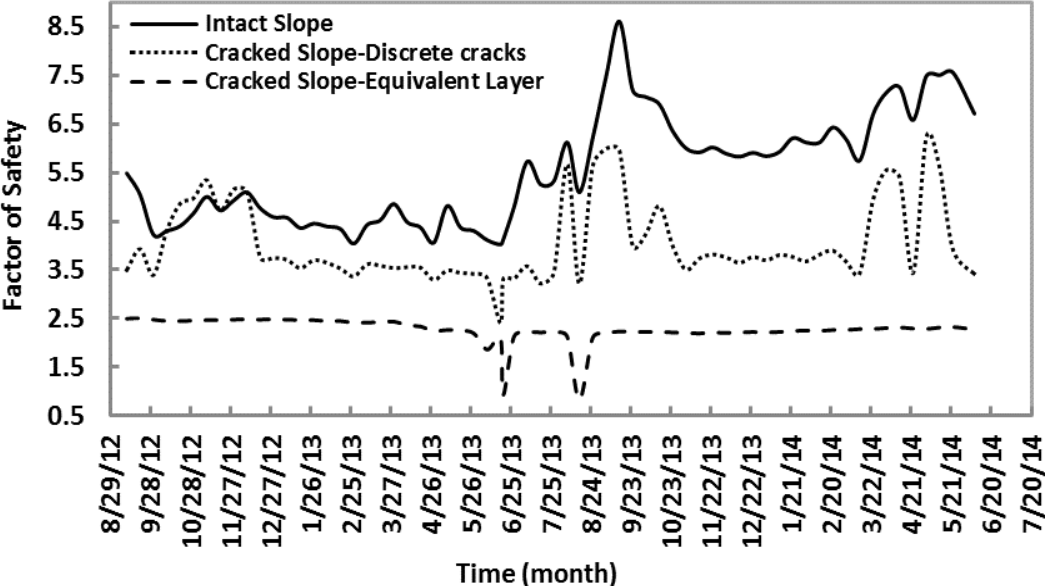


Figure 2.31. Factor of Safety for intact slope, slope with discrete cracks, and slope with an equivalent cracked layer

Figures 2.32 to 2.34 show the critical factors of safety at the same slip surfaces, which touched the bottom of the cracked layer in the slope. The minimum amount of factor of safety was for the slope modeled with the equivalent layer as shown in Figure 2.34. A summary of slope stability analysis using the calculation of the critical factor of safety is shown in Table 2.4. The effect of pore water pressure distribution with and without effective cohesion intercept for the upper layer on the slope stability analysis indicated that the slope failure considering both two variables (e.g. pore water pressure

distribution and effective cohesion intercept) was more likely to happen during the service life of the slope.

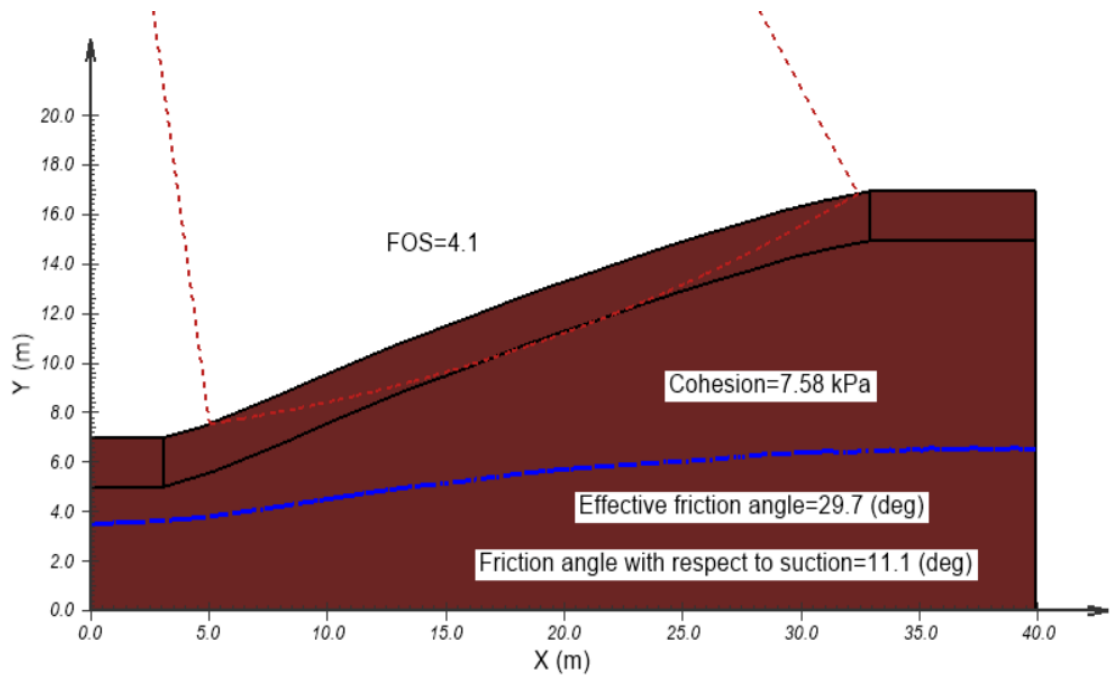


Figure 2.32. Critical Factor of Safety using circular slip surface for intact slope

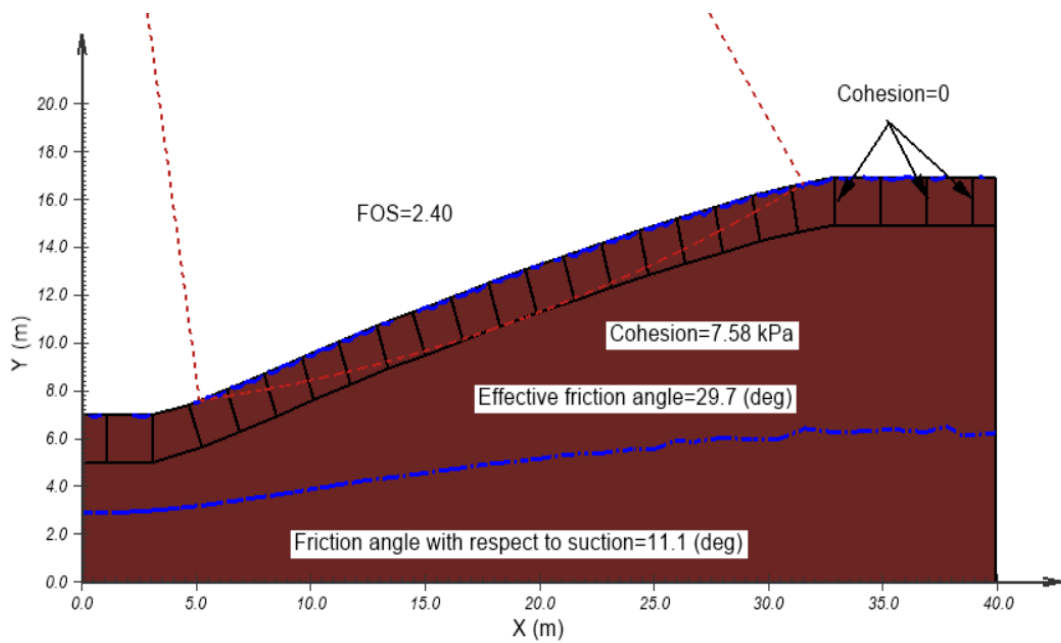


Figure 2.33. Critical Factor of Safety using circular slip surface for cracked slope (discrete crack model)

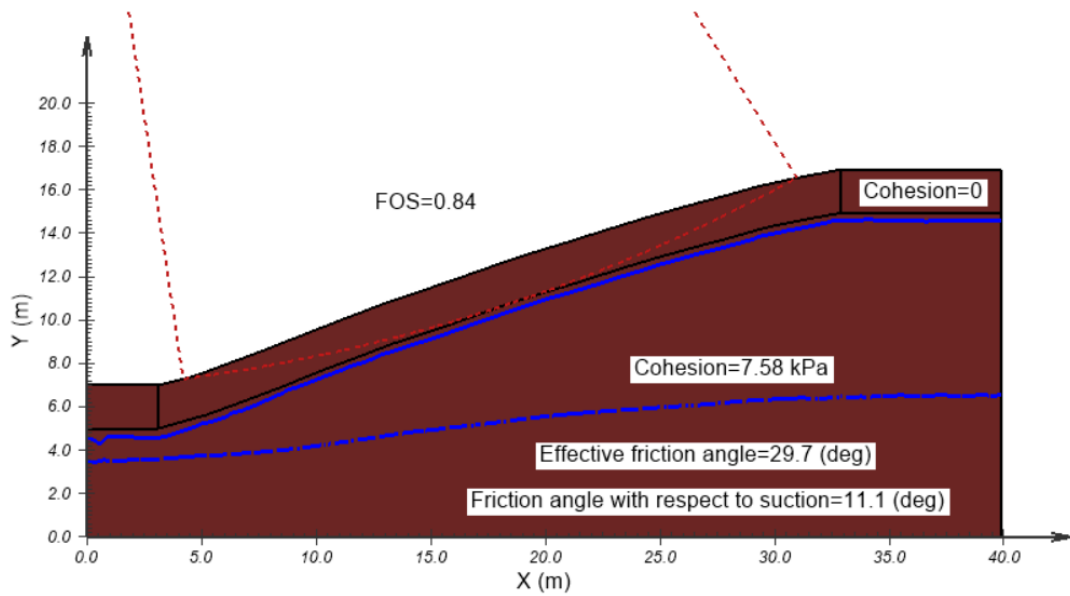


Figure 2.34. Critical Factor of Safety using circular slip surface for cracked slope (equivalent layer model)

Table 2.4. Summary of slope stability analysis

Slope seepage model	Factor of Safety	
	Cracked layer with Cohesion	Cracked layer without Cohesion
No crack	4.1	3.3
Discrete Cracks	2.4	1.9
Equivalent Layer	1.7	0.84

CHAPTER 3: Interface behavior between unsaturated soil and geomembranes

3.1 Background

Due to being relatively impermeable, geomembranes are employed in a variety of environmental, geotechnical, hydraulic, transportation, and private development projects such as dams, landfills, reservoirs, etc. Geomembranes at the best level of their performance divide soil layers into two separate parts with different moisture contents to prevent liquid or gas flow from top layer to the underlying soil. Shear strength parameters such as friction angle and cohesion of the interface between geomembrane and soil are needed to assess the stability of facilities involving such a material. Failures occurred in landfills across the world studied by Mitchell et al. (1990), and Koerner and Soong (2000), illustrated the importance of interface mechanical behavior on stability. The studies conducted indicated that the low friction angle between the geomembrane and soil, as compared to internal friction angle of soil, was one of the triggering causes of the failures. Landfill failure occurred in Kettleman City, California included a lateral displacement and vertical settlement of up to 10.7 m and 4.3 m, respectively. The most critical interface characteristics among the multilayers system of liners were recognized between high-density polyethylene (HDPE) geomembrane and geonet, HDPE geomembrane and geotextile, and HDPE geomembrane and saturated compacted clay. The type of surface failure for the landfills lined with geomembrane studied by Koerner and Soong (2000) were translational above or below the geomembrane and the main triggering mechanism of the failures were attributed to an excess pore water pressure generated at interface between the geomembrane and the underlying clayey soil. Thus,

it is crucial to understand and assess the interface shear strength parameters between the geomembrane and soil at different conditions using proper testing programs.

A common testing program to obtain the interface shear strength parameters is conducted using pull out, direct shear, and ring shear or rotational shear apparatuses. These devices vary from the geometry and boundary conditions to the load application. A pull-out machine is a large direct shear box, which used to measure a peak and residual shear strength of interfaces by applying a relatively large horizontal displacement. A direct shear device is a standard machine introduced by ASTM D5321-02 and D6243-06, to assess the frictional behavior of interfaces between soil-geosynthetics or geosynthetic-geosynthetic, respectively. A rotational shear device provides a relatively large displacement without the need of a directional reversal. In addition to these common devices a circular arc test developed by developed by Ghiassian et al. (1997), which is based on a variation of tension created on a circular arc of geosynthetic installed over soil in the presence of dead load on two ends.

Interface mechanisms that produce shearing resistance between geomembrane and soil include: sliding, adhesion, rolling of soil particles, interlocking of soil particles and geomembrane surface, plowing of soil particles into geomembrane surface, negative pore water pressure or suction in the interface (Jogi, 2005). Normal stress, compaction conditions, consolidation, shear displacement rate, type of geomembrane, soil particle shape and property, and testing set-up are testing parameters that influence these shearing resistance mechanisms. Previous interface test results showed that a non-linear relationship existed between the interface shear

strength and normal stress for a wide range of normal stress. Dilation or expansion developed at the interfaces during shearing at lower normal stresses was cited as a reason for increases in the interface friction angle by Koutsourais et al. (1991). Thus, the range of normal stress used to obtain the interface friction angle must correspond with the field application. For example, an interface friction angle for a cap or landfill cover would be certainly different from the landfill base liner due to the various amount of normal stresses. Swan et al. (1991) showed the effect of compaction conditions in terms of dry unit weight and moisture content on the interface behavior of smooth geomembrane and clayey soil. They concluded that the increase of dry unit weight and water content can lead to increase of the friction angle and peak shear strength of interface. Seed and Boulanger (1991) also indicated that minor changes in dry unit weight and water content can lead to increase of two times or more for interface friction angle between smooth geomembrane and as-compacted clay liner. The effect of rate of shear displacement on the interface shear strength was studied by Fishman and Pal (1994). They concluded that a smooth geomembrane-clayey soil interface peak shear strength was not influenced by the rate of displacement. In contrast, a textured geomembrane-clayey soil interface was sensitive to the rate of shear displacement, which included a range from 12.7 mm/min to 0.005 mm/min. The high rate of displacement caused an increase in the observed cohesion for the interface between textured geomembrane and clayey soil.

The shearing process immediately after applying the normal stress simulates a fast loading condition insufficient for dissipation of excess pore water pressures and an

undrained-unconsolidated condition can occur. The investigation conducted by Gomez and Filz (1999) on the interface between smooth geomembrane and compacted clayey soil showed that the interface shear strength can increase due to the consolidation of the clay layer.

Koerner et al. (1986) collected a dataset based on interface shear strength between different types of geomembranes and cohesive soils. The cohesive soils were at degrees of saturation less than 100% and sheared in a drained condition without any control in pore water pressure. The interface friction and adhesion between the geomembranes and soils were less than those that exist between soil particles. However, geomembranes with soft or very hard surfaces indicated higher shear parameters due to change of shear plane from the geomembrane-soil interface to the soil-soil interface.

The effect of plasticity index on the shear strength of clayey soil and interfaces between soil and geomembrane (Textured and smooth PVC) was studied by Ling et al. (2001). The soils were prepared under as-compacted conditions and were similar to the field condition at the beginning of the test. Results were inconclusive in that they showed an increase in friction angle followed by a decrease with increasing plasticity index whereas the cohesion intercept increased with increasing of plasticity index.

The shear strength parameters of clay-smooth and textured HDPE interfaces were investigated by Fishman and Pal (1994). Clayey samples were prepared at partially saturated conditions and sheared without any control in pore water pressure during the shearing process. Tests indicated that the geomembrane-clay interface shear strengths

in unsaturated conditions could increase compared to those at the saturated conditions during shearing.

Monteiro et al. (2013) employed smooth and textured geomembranes to study their interface behavior with sandy soil at different degrees of saturation. They showed that the effect of the degree of saturation on the interface friction angles was small or negligible. As expected, the friction angle between the textured geomembrane and the sandy soil was higher compared to the smooth geomembrane interface.

Interface shear tests on smooth geomembrane-soil interfaces were performed by Fleming et al. (2006) using a modified direct shear apparatus installed with a miniature pore pressure transducer (PPT). Using the PPT, pore water pressure changes close to geomembrane-soil interface were measured during the shearing process, thus making it possible to analyze test results in terms of effective stresses. Since the miniature pore water pressure transducer was able to capture the suction at a low range (up to 30 kPa), a sandy soil having low suction was used. At lower normal effective stresses, however, it was possible to predict interface shear strength values using unsaturated soil mechanics concepts and matric suction measured in the vicinity of the geomembrane–soil interface during the shearing process. At high normal stresses, the use of unsaturated soil mechanics concepts resulted in calculated shear strength values that were significantly lower than the measured values.

An examination of the change in surface roughness of the geomembrane surface strongly indicated that at higher normal stresses, the failure mechanism changed from pure sliding to a combination of sliding and plowing (Fleming et al. 2006).

It appeared that soil particles embedded partially into the geomembrane surface plowed trenches in the surface of the geomembrane during shear displacement under higher normal stress. As a result, additional shear strength was mobilized at the interface in addition to that mobilized by frictional sliding.

To better interpret the experimental results of soil-geomembrane interface, it is necessary to establish a constitutive model. Gilbert and Byrne (1996) used a linear relationship between shear stress and shear displacement in order to quantify the magnitude and rate of strain-softening for selected containment system interfaces such as geomembrane-clay soil, geomembrane-geotextile interfaces.

Reddy et al. (1996) used a hyperbolic model proposed by Clough and Duncan (1969) to predict the geomembrane-geotextile interface behavior. The relationship between shear stress and relative shear displacement at the interface was nonlinear and stress dependent. Esterhuizen et al. (2001) developed a constitutive model based on displacement-softening and work-softening models. The above-mentioned models were used to assess the clay-geomembrane interface behavior at constant and increasing normal stresses during shearing, respectively.

Hu and Pu (2003, 2004) proposed two constitutive models to assess the mechanical behavior of a rough interface such as hardening, softening, and shear dilatancy with nine and ten parameters, respectively. Seo et al. (2004) proposed two constitutive models for pre-peak and post-peak behavior of a geomembrane-geotextile interface. The first was the combined model, which was a modified displacement-softening model proposed by Esterhuizen et al. (2001); the second was a Disturbed State

Concept (DSC) model, which takes into account the disturbance of a material subjected to a force using a disturbance function coupling the initial relative intact state and the fully adjusted state of a material.

Zhou and Lu (2009) proposed a 2-D constitutive model based on the generalized potential theory. The strain-softening and dilation of interface in the model was considered and verified using sand-rigid materials interface results. Anubhav and Basudhar (2010) used a non-linear constitutive model to predict the interface behavior between soil and woven geotextile. The model was able to capture the interface shear strength parameters over the complete stress-displacement ranges. Back analysis from the experimental tests was used to develop the simplified model.

In addition to the material models, many researchers have created models to address specific boundary value problems of interest to geotechnical engineers. For example, Wu and Shu (2012) proposed a method based on a combination of the limit equilibrium method and numerical analysis to model the stability of an earth dam considering the geomembrane and soil interaction. They have found that the interface shear strength, the deformation of dam, and relative shear displacement are the main factors in impacting the factor of safety.

A model of progressive failure for typical municipal solid waste liners was used by Filz et al. (2001) in finite element analysis and the results were compared to those from the limit equilibrium method, which is not able to consider the progressive failure. The parametric studies of seven different cases indicated that an increase of about 10

% from the residual to peak shear strength would be a safe margin for designing municipal solid waste liners.

It is clear from the preceding literature review that significant work has focused on soil-geomembrane interface behavior. However, to truly understand the mechanical behavior of this interface, the constitutive behavior, i.e. shearing behavior, must be examined under controlled stress conditions in the unsaturated state. In this way, the importance of net normal stress and matric suction can be appreciated, and constitutive models of the behavior under varying states of saturation can be developed. The work described in this chapter begins to fill in this gap in knowledge by providing an experimental data set from suction controlled testing of unsaturated soil-geomembrane interfaces. In addition, a constitutive model developed for unsaturated soil-interfaces is evaluated using these data.

3.2 Unsaturated Geomembrane-Soil Interface testing

3.2.1 Material and Sample Preparation

The modified direct shear apparatus developed by Hamid (2005) was used to conduct the unsaturated shear interface tests. A medium plastic soil, obtained from the Chickasha, Oklahoma embankment described previously, was selected as a test specimen. The Chickasha soil had a liquid limit, LL=38%, plastic limit, PL=20%, plasticity index, PI=18%, and 89.4% fines (49.4% silt and 40% clay). This soil was selected because it has been the focus of significant study at OU and it has characteristics that are consistent with those required for a compacted clay liner (Koerner and Daniel 1997). Often, compacted clay liners are placed above in contact with geomembranes to

produce a composite liner for retaining waste and leachate in sanitary and hazardous waste landfills.

The maximum dry unit weight measured by a standard proctor test was 17.3 kN/m^3 and optimum moisture content (OMC) was 18%. The specimens for interface tests were prepared at 95% of maximum dry unit weight and 3% wet of optimum moisture content. These compaction criteria are consistent with specifications for compacted clay liners. The specimens were placed in a humid room for 24 hours to have a specimen with uniformly distributed moisture.

Two high density polyethylene (HDPE) geomembranes with different surface roughness were selected for interface tests with soil. Geomembranes with textured and smooth surfaces were cut circularly in the machine direction (MD) from the roll donated by GSE Company as shown in Figure 3.1.



Figure 3.1. Textured geomembrane cut and rolled (a) and smooth geomembrane cut and rolled (b)

The mechanical specifications of geomembranes are shown in Table 3.1. The circular specimens were glued to a steel plate with an adequate thickness to fill the

lower half of the shear apparatus and the upper half was filled with prepared soil compacted to the target dry unit weight. Soil was placed in three lifts inside the upper half the shear box and compacted using a tamping rod to achieve the target density (volume based compaction).

The roughness of the geomembranes was characterized using the surface roughness definition proposed by Uesugi and Kishida (1986), and was employed for the geomembrane's surfaces as follows:

$$R_n = R_{max}/D_{50} \quad (3.1)$$

Where, R_{max} is the maximum peak to valley height, and D_{50} is the grain size diameter corresponding to fifty percent finer. The maximum peak to valley height for smooth geomembrane was assumed to be 0.0045 mm, which was compatible with that measured by Dove et al. (1996) using tapping mode atomic force microscopy. They have obtained mean value and standard deviation for a surface of smooth HDPE geomembrane at a scale comparable to fine-grained soil particles. The maximum value was calculated using the following equation:

$$R_{max} = R_a - 2R_q \quad (3.2)$$

Where, R_a is the mean value, which was 0.005 mm, and R_q is the standard deviation, which was 2e-4 mm. R_{max} for the textured geomembrane was approximated by measuring the geomembrane peak-valley distance using a caliper, which was 0.45 mm.

Table 3.1. Properties of the smooth and textured geomembranes used in the interface shear tests

Property	Test Method	Geomembrane	
		Smooth	Textured
Thickness (mm)	ASTM D5994	1.00 nominal	1.00 nominal
Density (g/cm ³)	ASTM D1505	0.94	0.94
Carbon Black content (%)	ASTM D1603/4218	2-3	2-3
Elongation at break (%)	ASTM D6693	700	100
Tensile Strength at break (N/mm)	ASTM D6693	27	10
Tear resistance (N)	ASTM D1004	125	125
Puncture resistance (N)	ASTM D4833	320	267

3.2.2 Unsaturated geomembrane and soil interface testing procedure

The assembled shear box containing the interface test specimen was installed in the Direct Shear Test (DST) air pressure chamber. A sketch of the DST chamber containing the test specimen is shown in Figure 3.2 (after Khoury et al. 2011). A high air entry porous disc (HAEPD) saturated with de-aired water was installed on top of the specimen. Drainage lines connected to the pore water pressure controller and the diffused air volume indicator (DAVI) were attached to the inlet and outlet ports of the HAEPD, respectively. A seating load of 10 kPa was applied to the specimen in order to minimize movement of upper half of the shear box due to making the required gap between the upper and the lower halves of the shear box before the shearing process. A gap equal to 10-20 times of D_{50} of the soil was created approximately 30 minutes after placing the seating load. The DST air pressure chamber is isolated from outside using a lid equipped with 16 screws.

Pore water pressure is controlled through the inlet port of the saturated HAEPD installed on the top of the specimen. Air pressure is controlled through the inlet port in the lid of the chamber. The difference between pore water and air pressure is adjusted using the digital and manual regulators to reach the target suction value.

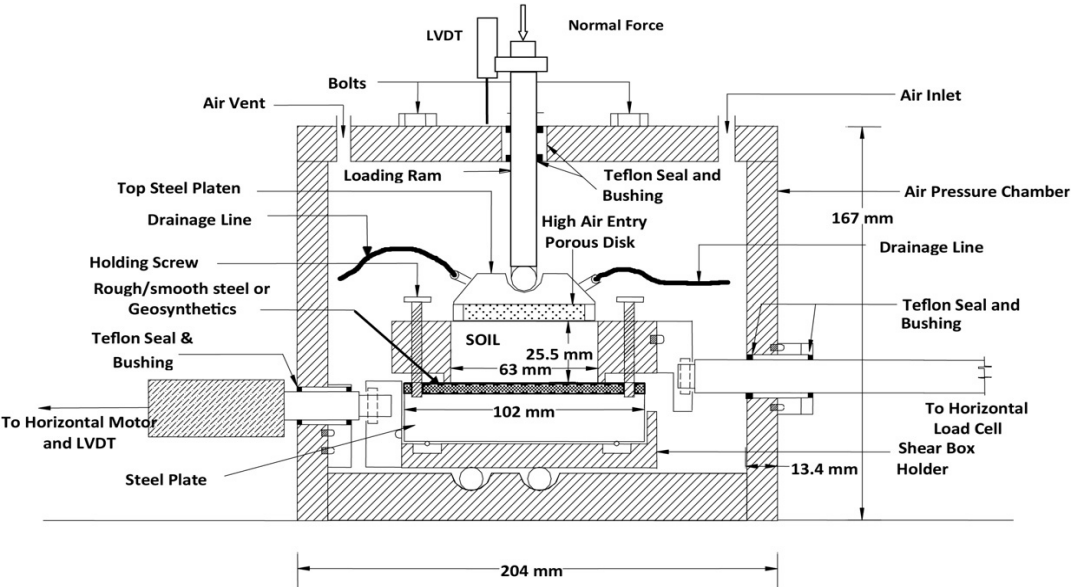


Figure 3.2. Schematic cross section of the test chamber and shear box (from Khoury et al. 2011)

An equilibrium state is required before starting the final consolidation. The equilibrium state is defined when the amount of vertical displacement of the specimen and the volume of water exiting from the specimen after apply the suction reach a constant value, indicating there is a negligible amount of change in total volume of the specimen and water volume. After reaching equilibrium, a gradual increase of vertical stress, using the increments of 10 kPa every 30 minutes, was applied on the top of the specimen until the target value of net normal stress was achieved. The end of consolidation is defined as the time when there is negligible change in volume of soil after reaching the target net normal stress.

The target values of suction according to test matrix shown in Table 3.2 were obtained through applying a constant pore water pressure of 40 kPa, and air pressures of 240 and 440 kPa for the target suction values of 200 and 400 kPa, respectively. The effect of strain rate on the shear behavior was investigated by comparing results of selected tests conducted at two different displacement rates. The displacement rates selected were based on results reported in the literature for direct shear testing of fine-grained cohesive soils. The effect of strain rate on the shear strength behavior was examined only for 200 kPa suction.

Table 3.2. Test matrix of unsaturated geomembrane-soil interface tests

Geomembrane-Test	Net normal stress (kPa)	Suction (kPa)	Displacement rate (mm/min)
Textured-1	25	200	5e-3
Textured-2	50	200	5e-3
Textured-3	75	200	5e-3
Smooth-1	25	200	5e-3
Smooth-2	50	200	5e-3
Smooth-3	75	200	5e-3
Textured-4	25	200	5e-4
Textured-5	50	200	5e-4
Textured-6	75	200	5e-4
Smooth-4	25	200	5e-4
Smooth-5	50	200	5e-4
Smooth-6	75	200	5e-4
Textured-7	25	400	5e-4
Textured-8	50	400	5e-4
Textured-9	75	400	5e-4
Smooth-7	25	400	5e-4
Smooth-8	50	400	5e-4
Smooth-9	75	400	5e-4

3.3 Saturated geomembrane-soil interface testing

3.3.1 Material and sample preparation

A conventional small direct shear device with the same shear box shape as that used for the unsaturated condition was employed to conduct the saturated interface shear tests. The specimens for saturated testing were prepared in the same manner as unsaturated specimens.

3.3.2 Saturated geomembrane-soil interface testing procedure

A seating load of 10 kPa was applied to the specimen to keep the position of soil while making the required gap before the shearing process. The specimen within the shear box was submerged in water for 24 hours and then a target value of normal stress according to the test matrix shown in Table 3.3 was applied to the specimen for 24 hours. The vertical displacements during the saturation and consolidation conditions indicated that the elapsed time for each phase (saturation and consolidation) were adequate to reach the equilibrium states. The shearing phase was started after making a required gap, which was similar to the unsaturated interface shear test.

Table 3.3. Test matrix of saturated soil-geomembrane interface tests

Geomembrane-Test	Net normal stress (kPa)	Displacement rate (mm/min)
Textured-1	25	5e-4
Textured-2	50	5e-4
Textured-3	75	5e-4
Smooth-4	25	5e-4
Smooth-5	50	5e-4
Smooth-6	75	5e-4

3.4 Saturated and unsaturated soil-soil interface testing

A series of modified and conventional direct shear tests on soil only was conducted to compare the results with interface shear tests between the soil and geomembrane at the same stress conditions. To keep the consistency, the soil specimens were prepared in a manner similar to the interface tests. A summary of the test matrix is shown in Table 3.4 for saturated and unsaturated soil-soil direct shear tests. A difference between soil-soil direct shear tests and geomembrane-soil interface tests is that in the case of soil-soil DSTs, pore water pressure drainage lines connect to the HAEPD is the pedestal of the top cap. Also, both the lower and upper half of the shear boxes were filled with the compacted soil for soil-soil DSTs.

Table 3.4. Test matrix of saturated and unsaturated soil-soil direct shear tests

Condition-Test	Net normal stress (kPa)	Suction (kPa)	Displacement rate (mm/min)
Saturated-1	25	0	5e-4
Saturated-2	50	0	5e-4
Saturated-3	75	0	5e-4
Unsaturated-1	25	200	5e-4
Unsaturated-2	50	200	5e-4
Unsaturated-3	75	200	5e-4
Unsaturated-4	25	400	5e-4
Unsaturated-5	50	400	5e-4
Unsaturated-6	75	400	5e-4

3.5 Results of unsaturated geomembrane-soil interface tests

This section presents the results of interface tests under unsaturated conditions in a modified direct shear box. The effect of net normal stress ($\sigma_n - u_a$), suction ($u_a - u_w$), rate of displacement, and roughness on the horizontal stress-displacement and volumetric behavior of unsaturated interfaces are discussed.

3.5.1 Effect of net normal stress

A series of net normal stresses including 12.5, 25, 50, and 75 kPa was selected to investigate the effect of net normal stress on the shear strength and volumetric behavior of interfaces, which are presented in this section. Interface test results are plotted in the form of shear stress and vertical displacement evolution during shearing and in the form of water and specimen volume changes during shearing. The results presented in this section correspond to a matric suction of 200 kPa and a displacement rate of 0.005 mm/min.

3.5.1.1 Effect of net normal stress on textured interface behavior

According to Figures 3.3 and 3.4, the peak shear stress and residual stress of the interface between textured geomembrane and test soil showed an increase with increase in net normal stress. Dilation, or increase in volume during shearing, was more pronounced at lower net normal stresses. The specimens subjected to lower net normal stresses (e.g. 12.5 and 25 kPa) experienced more strain-softening behavior compared to higher net normal stresses (e.g. 50 and 75 kPa). The peak shear stress reached after low amount of shear displacement equal to approximately 1 mm especially for low range of net normal stress. The residual shear stress condition appeared as a flat line after approximately 3 up to 4 mm displacement in the shear stress-horizontal displacement curves and the dilation process was stopped.

During shear process, a small volume of water tended to be drained out from the soil specimen even during dilation. The tendency of water drainage was lower when the dilation was higher as shown in Figure 3.5. It is believed that disruption of the air-

water interface (i.e. menisci) among the soil particles tends to increase the pore water pressure as the soil dilates and this tends to a decrease the suction and thus, water must drain as pressure control system maintains constant suction (drained test).

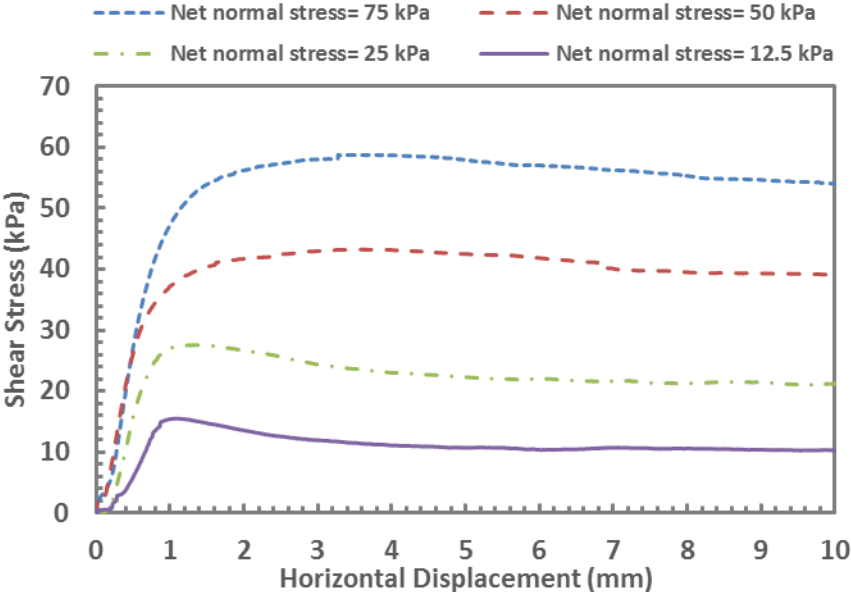


Figure 3.3. Shear stress changes during shearing at different net normal stresses for a matric suction of 200 kPa for textured geomembrane interface

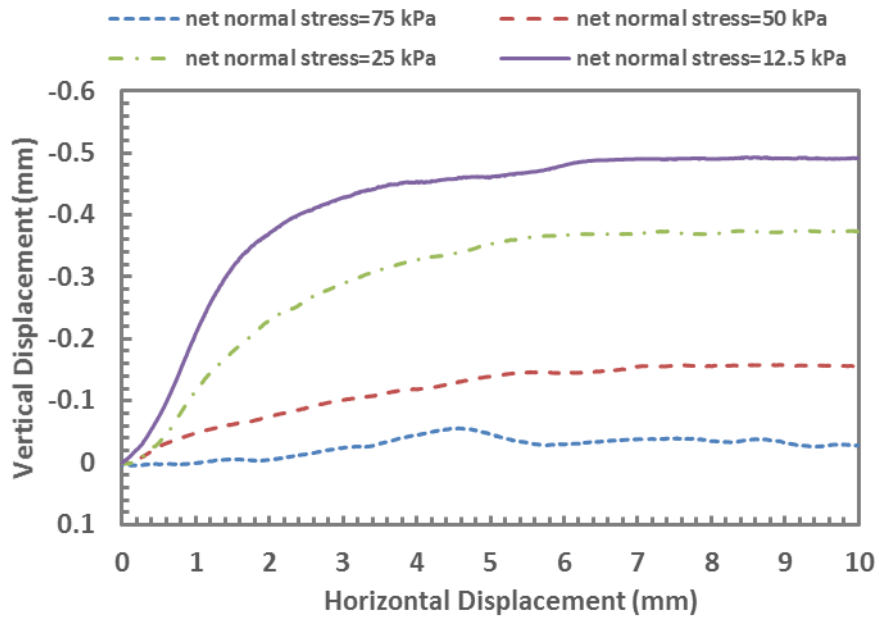


Figure 3.4. Vertical displacement versus horizontal displacement at different net normal stresses for a matric suction of 200 kPa for textured geomembrane interface

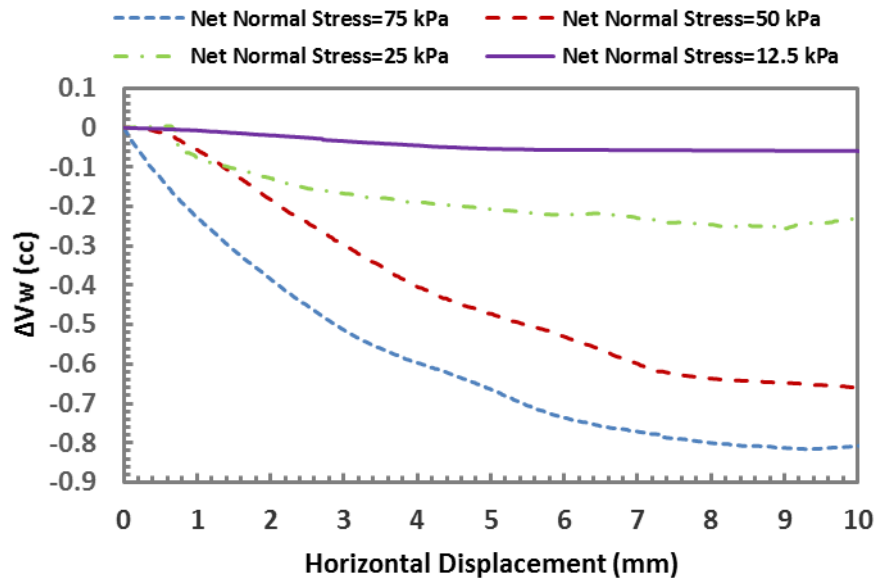


Figure 3.5. Water volume change versus horizontal displacement at different net normal stresses for textured geomembrane interface

3.5.1.2 Effect of net normal stress on smooth interface behavior

According to Figures 3.6 and 3.7, the peak shear stress and residual shear stress of the interface between smooth geomembrane and test soil increased with increase in net normal stress. Samples showed a strain-softening behavior during the shearing process. Observations from the vertical displacement versus horizontal displacement curves indicate that a small amount of dilation occurred at the beginning of shearing followed by contraction. The curves are somewhat irregular, but it is clear the amount of contraction tended to be greater as net normal stress (e.g. 75 kPa) increased. The shear stress reached a peak value at very low horizontal displacement equal to approximately 0.5 mm during the shearing process. The post-peak shear stress occurred after approximately after 4 mm for all specimens subjected to different net normal stresses.

As opposed to the rough interface tests, the unsaturated smooth interface tests indicated a similarity to some extent to expected volume changes for drained saturated soils, as shown in Figure 3.8. In the saturated condition during shearing, dilation points out a tendency for the development of matric suction, thus water tends to enter the soil specimen to maintain constant pore water pressure. In contrast with dilation, contraction indicates a tendency for generation of positive pore water pressure, thus water tends to exit from the specimen during shearing to maintain constant pore water pressure.

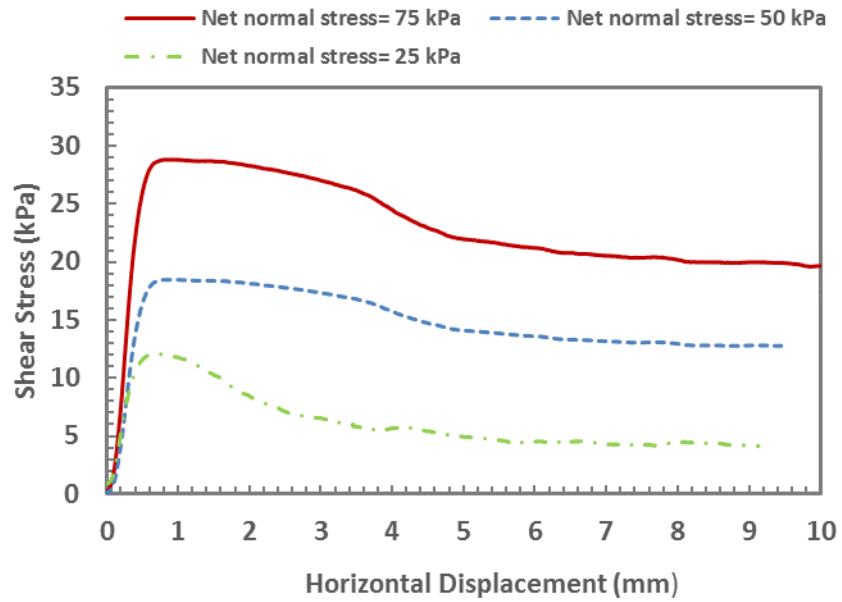


Figure 3.6. Shear stress changes during shearing at different net normal stresses for a matric suction of 200 kPa for smooth geomembrane interface

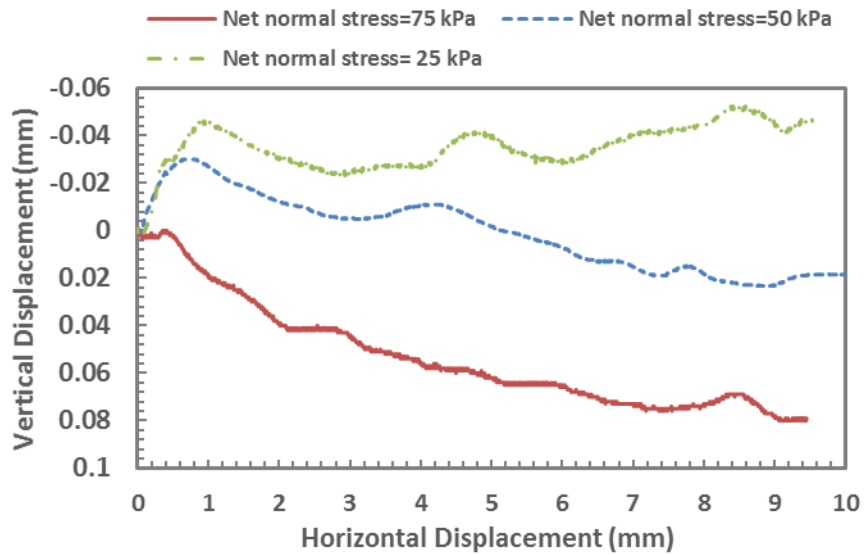


Figure 3.7. Vertical displacement versus horizontal displacement at different net normal stresses for a matric suction of 200 kPa for smooth geomembrane interface

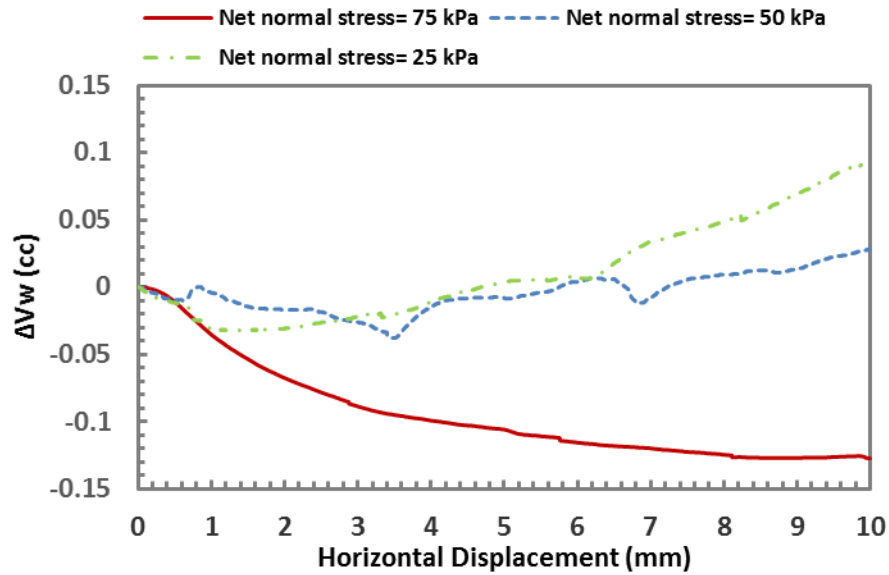


Figure 3.8. Water volume change versus horizontal displacement at different net normal stresses for a matric suction of 200 kPa for smooth geomembrane interface

3.6 Effect of shear displacement rate

The effect of different rates of displacement (e.g. 0.005 and 0.0005 mm/min) on the shear strength and volumetric behavior of soil and interfaces was investigated in this section. Interface and soil test results are plotted in the form of shear stress and vertical displacement evolution during shearing as shown in Figures 3.9 to 3.14. The results presented in this section represent a matric suction of 200 kPa and different net normal stresses of 25, 50, and 75 kPa.

3.6.1 Effect of rate of shear displacement on textured interface behavior

According to Figures 3.9 and 3.10, the peak shear stress at the interface between textured geomembrane and test soil showed a decrease with increasing rate of shear displacement. The shear stress increased less and exhibited lower stiffness for the interfaces subjected to low rate of shear displacement (0.0005 mm/min), compared to

those obtained from the high shear displacement rate (0.005 mm/min). The dilatancy of the tests conducted at the high shear displacement rate was also more pronounced than the ones conducted at the low shear displacement rate. The variation of peak shear strength and net normal stress indicated that cohesion intercept and friction angle of the low shear displacement tests were considerably less than those obtained from the high shear displacement tests as shown in Figure 3.11.

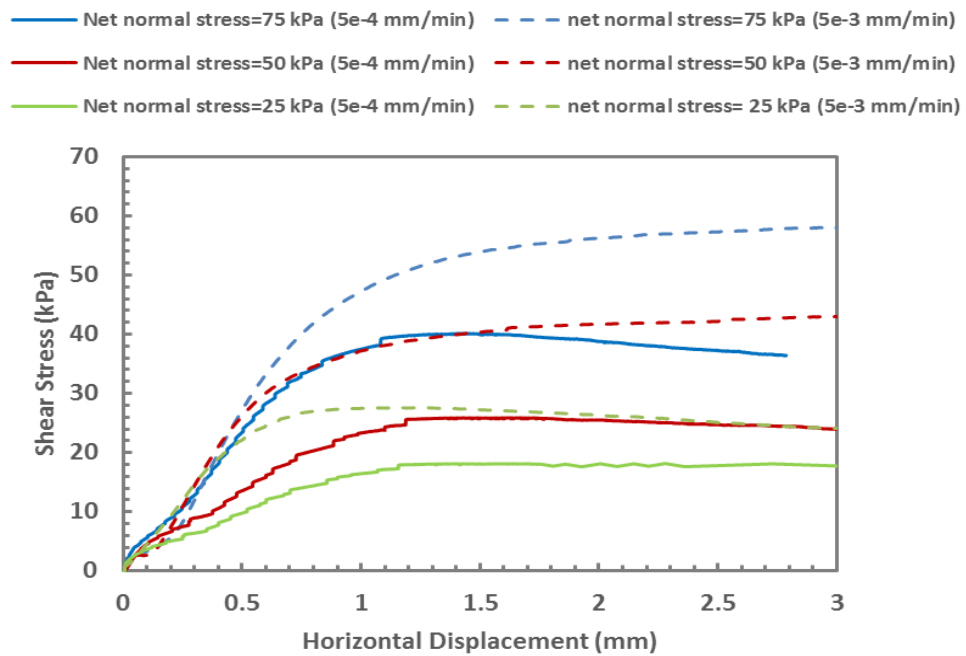


Figure 3.9. Shear stress changes during shearing at different strain rates for textured geomembrane-soil interface for a matric suction of 200 kPa

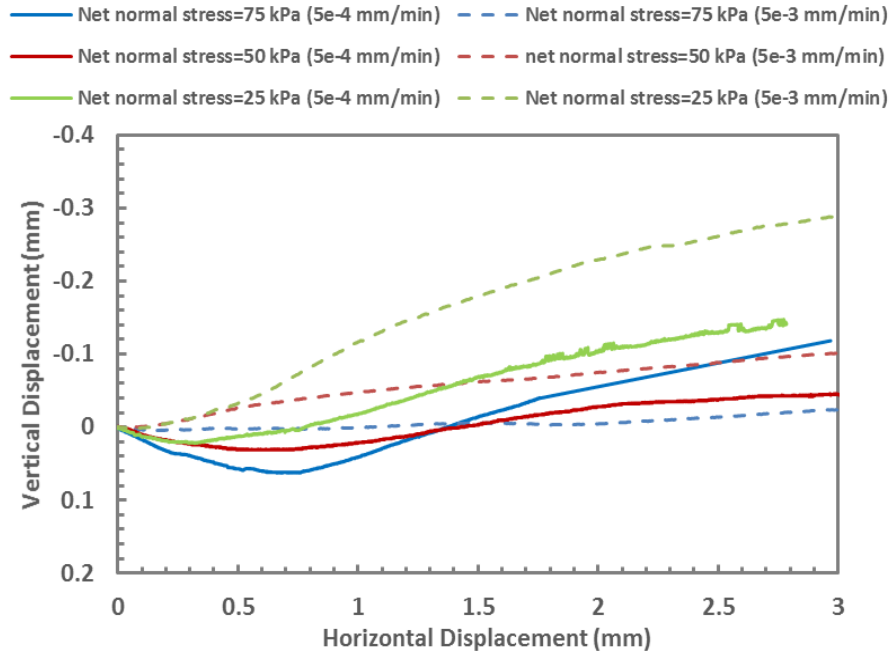


Figure 3.10. Vertical displacement versus horizontal displacement at different strain rates for textured geomembrane-soil interface

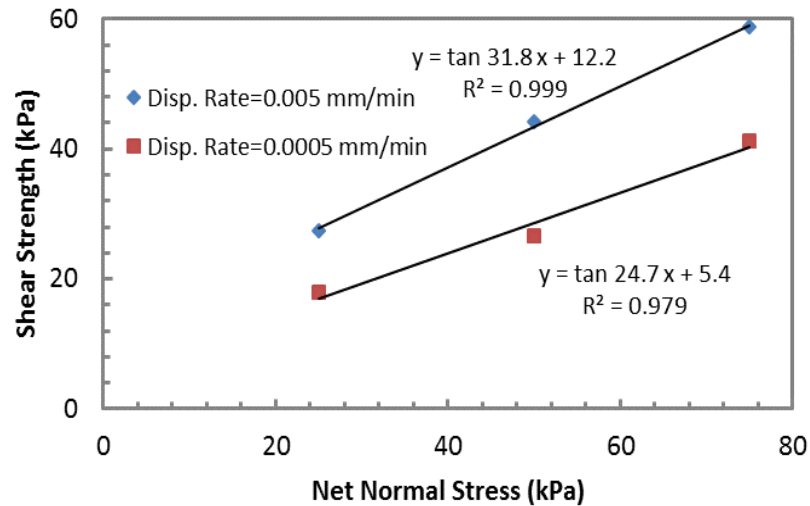


Figure 3.11. Extended Mohr-Coulomb envelope during a constant suction test at different displacement rates for textured geomembrane-soil interface for a matric suction of 200 kPa

3.6.2 Effect of rate of displacement on smooth interface behavior

According to Figures 3.12 and 3.13, the effect of shear displacement rate on the peak shear stress was not as apparent for the interface between smooth geomembrane and

test soil. The strain-softening behavior for the samples subjected to the low shear displacement rate (0.0005 mm/min) was slightly more pronounced than those at the high shear displacement rate (0.005 mm/min). The shear stress reached almost the same peak value for both rates but the slope of variations was steeper for the high displacement rate compared to the low displacement rate. However, the vertical displacement during the shearing process shows that tendency for dilation was lower when the shear displacement rate decreased. As shown in Figure 3.14, there was no considerable change in the variation of peak shear stress against net normal stress for the selected displacement rates.

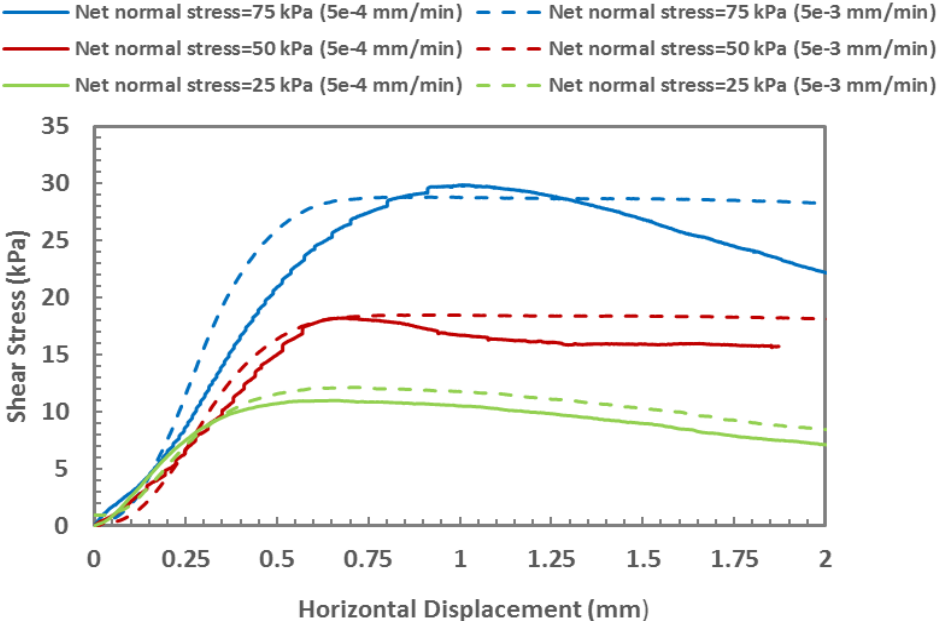


Figure 3.12. Shear stress changes during shearing at different strain rates for smooth geomembrane-soil interface for a matric suction of 200 kPa

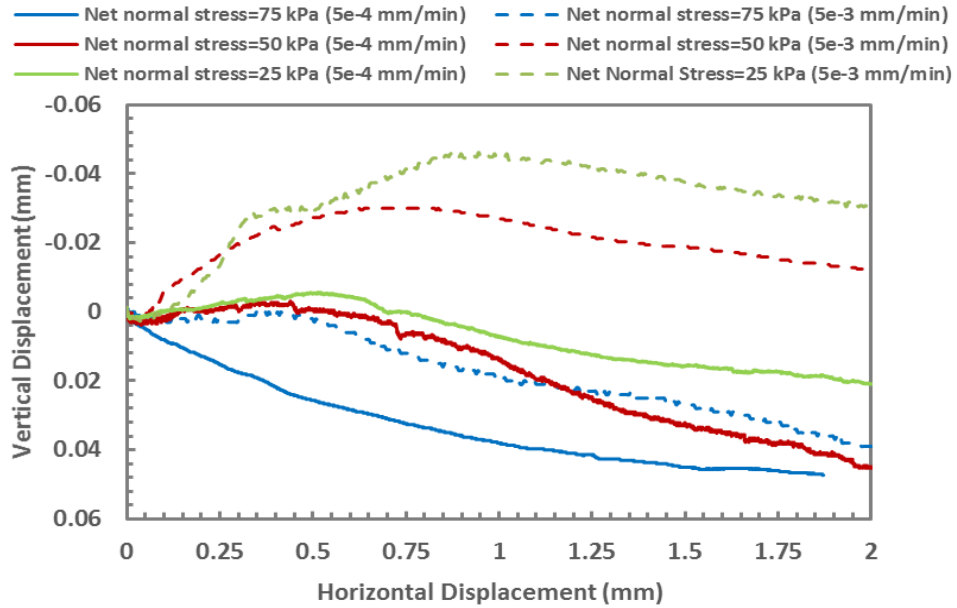


Figure 3.13. Vertical displacement versus horizontal displacement at different strain rates for smooth geomembrane-soil interface for a matric suction of 200 kPa

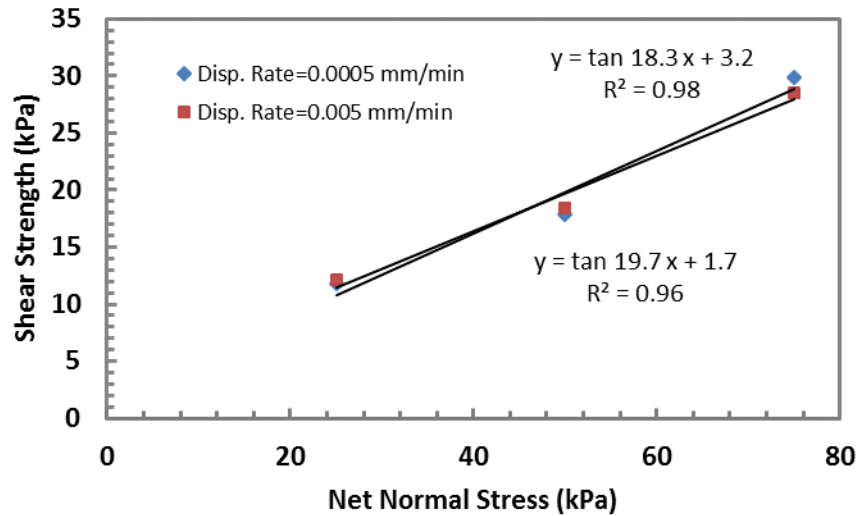


Figure 3.14. Extended Mohr-Coulomb envelope during a constant suction test at different displacement rates for smooth geomembrane-soil interface for a matric suction of 200 kPa

3.7 Effect of suction

Matric suction values of 200 and 400 kPa was selected to investigate the effect of suction on the shear strength and volumetric behavior of soil and interfaces, which are

presented in this chapter. Interface test results are plotted in the form of shear stress and vertical displacement evolution during shearing as shown in Figures 3.15 to 3.16. Results presented in this section were recorded under constant net normal stress (e.g. 50 kPa) using a displacement rate equal to 0.0005 mm/min.

3.7.1 Effect of suction on textured interface behavior

The variations of shear stress during the shearing process for interface between textured geomembrane and test soil under constant net normal stress are shown in Figure 3.15. The peak shear stress increased with increase of matric suction. A tendency to have a strain softening behavior was more pronounced in samples subjected to high suction. The samples experienced a contraction up to a horizontal displacement, in which the peak shear stress occurred and then dilated. The tendency for dilation was more pronounced for the samples under greater suction as shown in Figure 3.16.

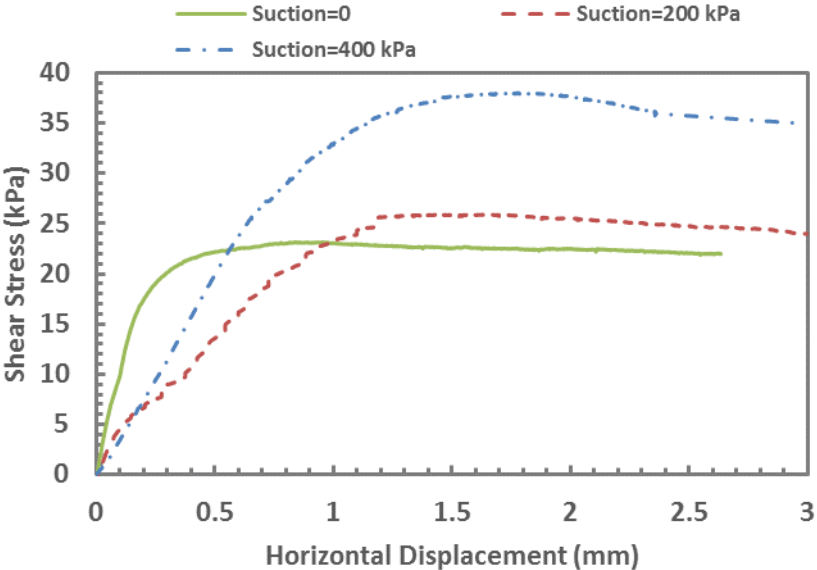


Figure 3.15. Shear stress changes during shearing at different suction for textured geomembrane-soil interface at net normal stress of 50 kPa

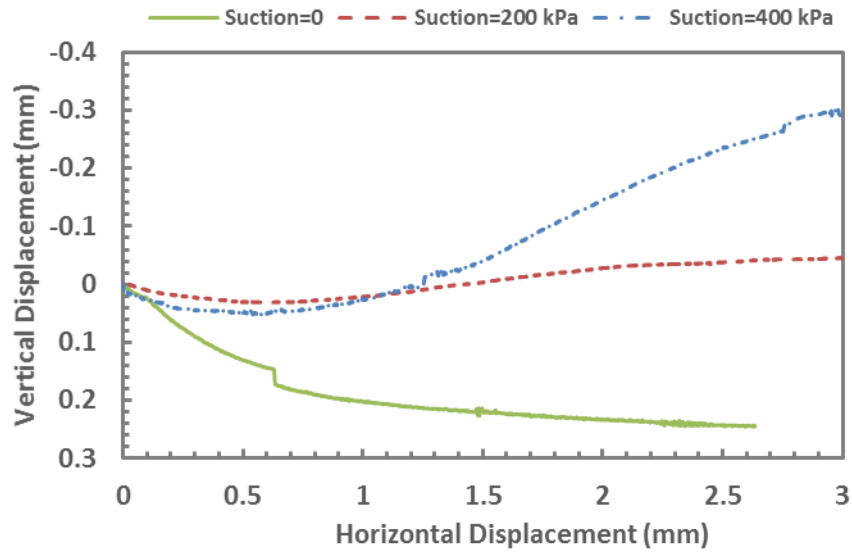


Figure 3.16. Vertical displacement versus horizontal displacement at different suction for textured geomembrane-soil interface at net normal stress of 50 kPa

3.7.2 Effect of suction on smooth interface behavior

In Accordance with Figures 3.17 and 3.18, the effect of matric suction on the smooth geomembrane and test soil interface was similar to that observed in textured interface shear tests. One difference was the peak shear stress was reached at a horizontal displacement of approximately 0.5 mm, which is about half of horizontal displacement experienced in textured interface shear tests. The tendency for contraction was more pronounced for the samples under lower suction compared to textured geomembrane-soil interface tests.

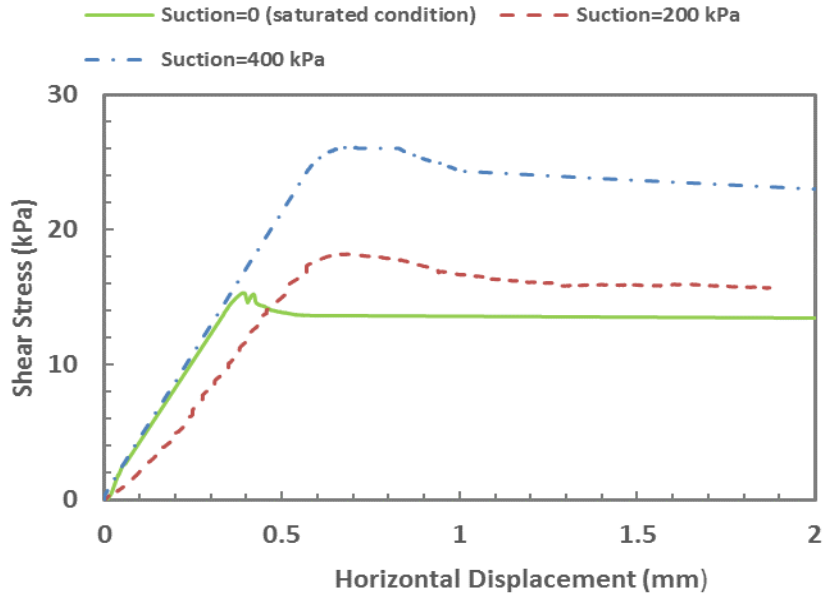


Figure 3.17. Shear stress changes during shearing at different suction for smooth geomembrane-soil interface for a net normal stress of 50 kPa

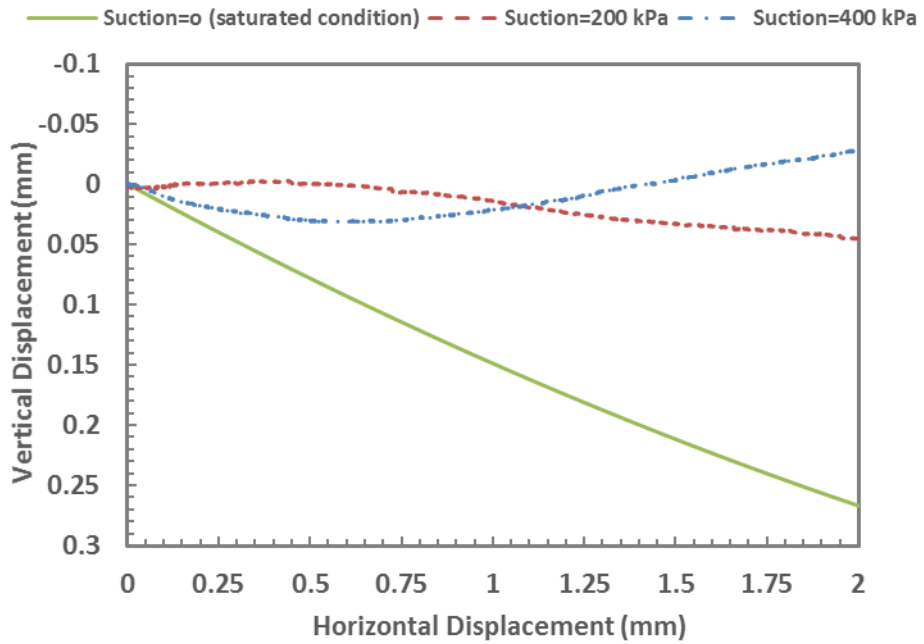


Figure 3.18. Vertical displacement versus horizontal displacement at different suction for textured geomembrane-soil interface

3.8 Results of saturated interface behavior

This section presents the results of interface tests under saturated conditions conducted using a conventional direct shear box. The effect of normal stress on shear stress-displacement and volumetric behavior of saturated interfaces are discussed.

3.8.1 Effect of normal stress on saturated textured interface behavior

The peak shear stress of the interface between textured geomembrane and test soil indicated an increase with increase in normal stress as shown in Figure 3.19. The contraction behavior of the specimen under higher normal stress was more noticeable during shearing as shown in Figure 3.20.

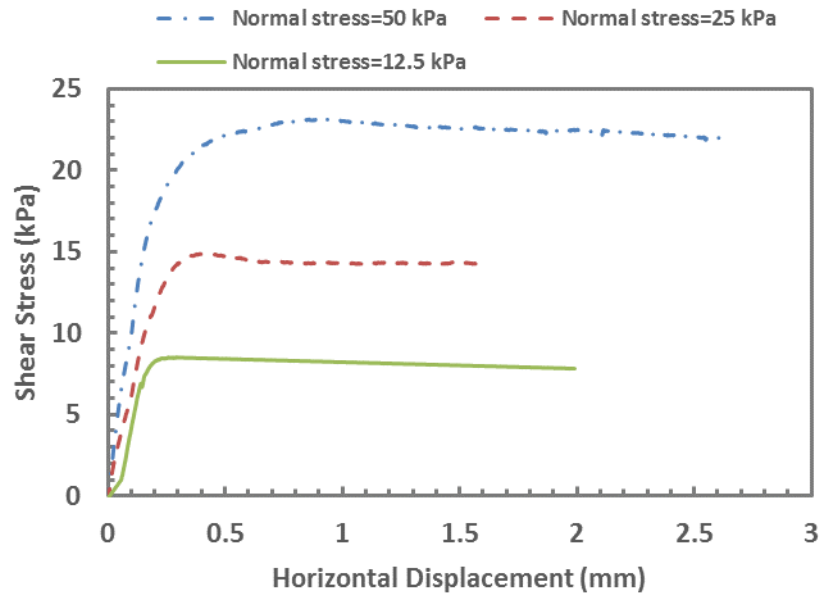


Figure 3.19. Shear stress changes during shearing at different normal stresses for textured geomembrane-soil interface under saturated conditions

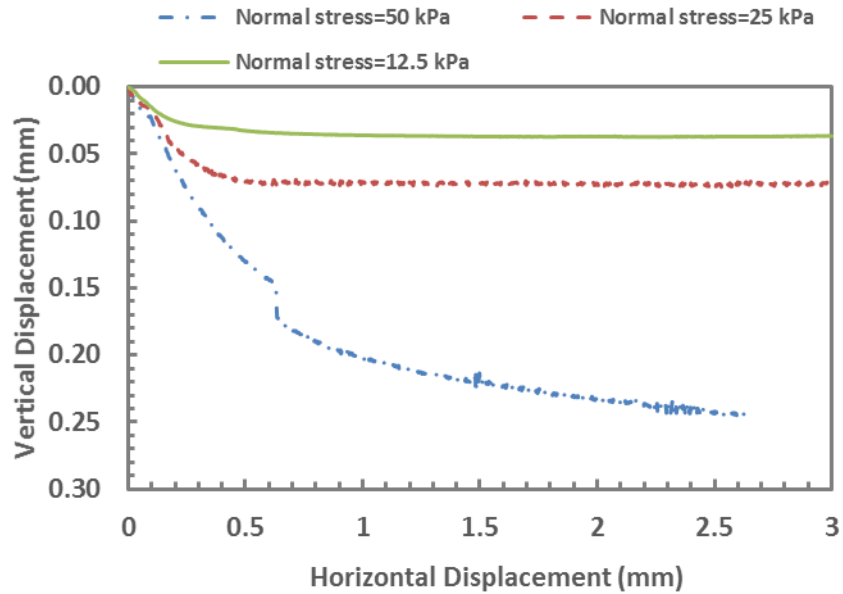


Figure 3.20. Vertical displacement versus horizontal displacement at different normal stresses for textured geomembrane-soil interface under saturated conditions

3.8.2 Effect of normal stress on saturated smooth interface behavior

The peak shear stress of the interface between smooth geomembrane and test soil occurred at the early stages of shearing and increased with increase of normal stress as shown in Figure 3.21. According to Figure 3.22, the volumetric behavior of smooth interface was analogous to that of the textured interface.

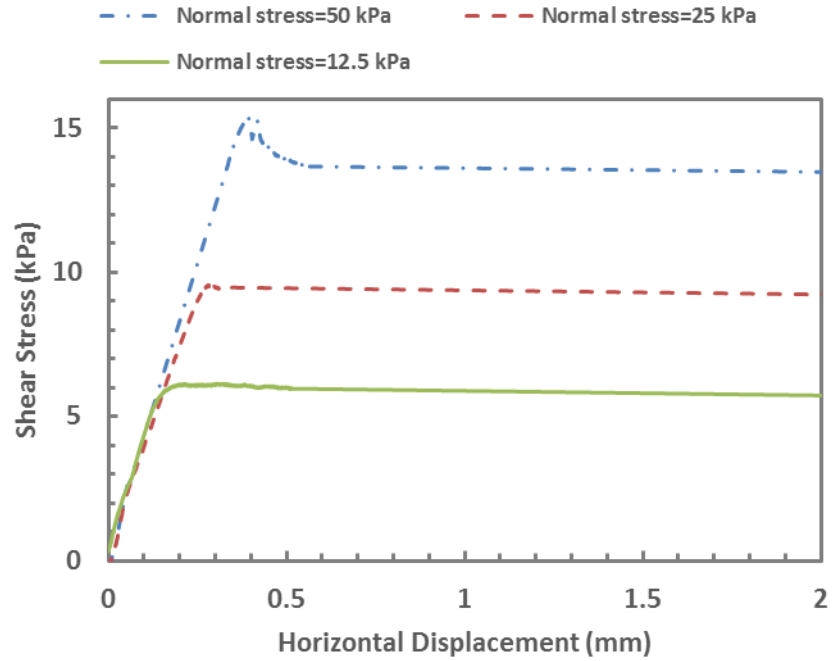


Figure 3.21. Shear stress changes during shearing at different normal stresses for smooth geomembrane-soil interface under saturated conditions

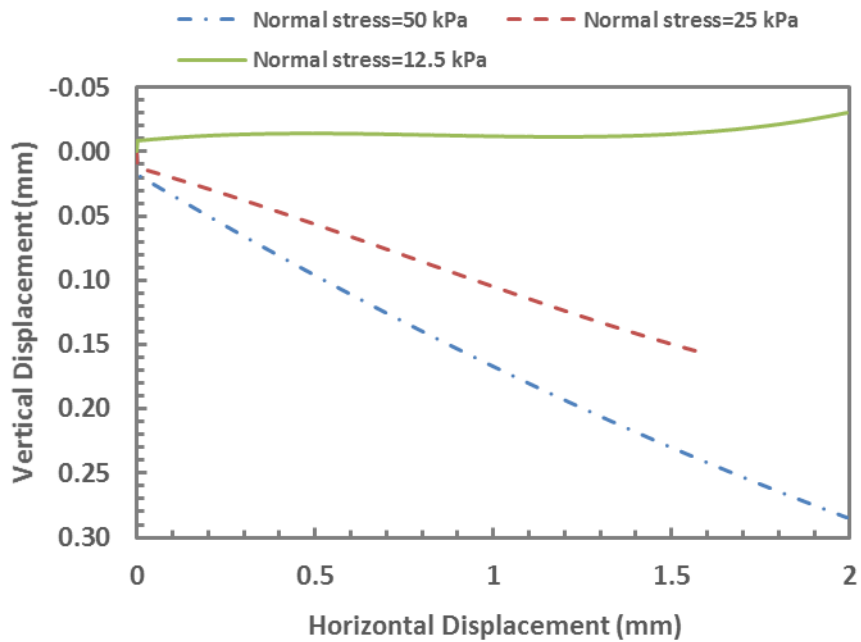


Figure 3.22. Vertical displacement versus horizontal displacement at different normal stresses for smooth geomembrane-soil interface under saturated conditions

3.9 Unsaturated/saturated soil direct shear test results

This section presents results of direct shear tests for soil specimens under both saturated and unsaturated conditions. The shear stress-displacement and volumetric behavior of the soil specimen under a suction of 200 kPa and zero kPa (or saturated condition) are discussed.

3.9.1 Unsaturated soil direct shear test results

The shear stress during soil direct shear testing reached a maximum value at a larger displacement than the textured and smooth interfaces for similar net normal stress, as seen when comparing Figure 3.23 to 3.3 and 3.6. Similar to unsaturated smooth and textured interface tests, the peak shear stress increased with increase of net normal stress. The dilation shown in Figure 3.24 was more pronounced when the results were compared to those from smooth and textured interface tests.

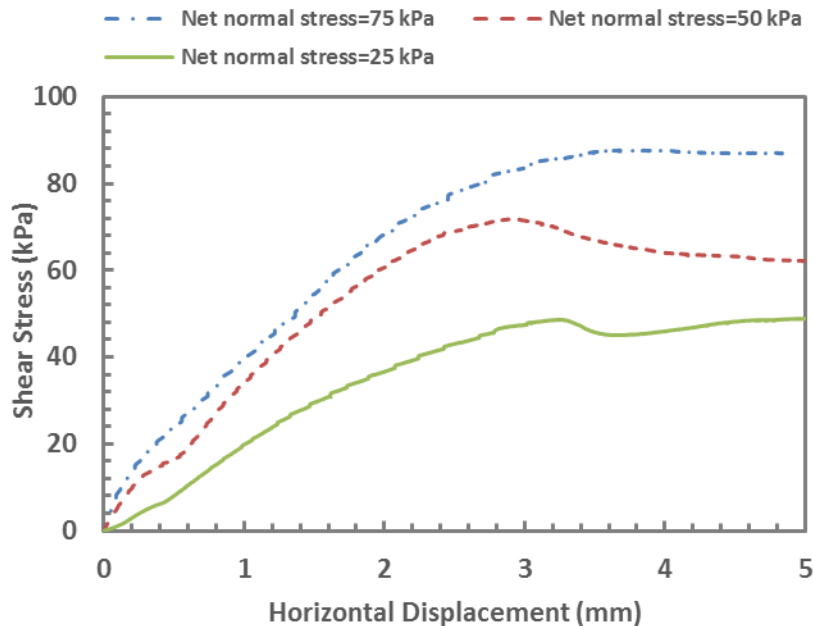


Figure 3.23. Shear stress changes during shearing at different net normal stresses and suction=200 kPa for soil direct shear tests

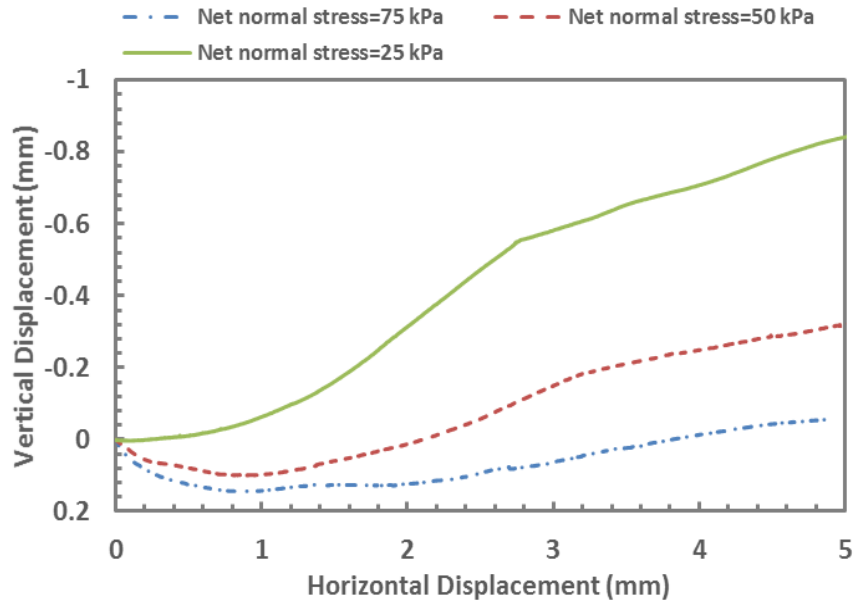


Figure 3.24. Vertical displacement versus horizontal displacement at different net normal stresses and suction=200 kPa for soil direct shear tests

3.9.2 Saturated soil direct shear test results

The peak shear stress was reached at relatively small displacements during shearing for saturated soil-soil direct shear tests. The peak shear stress increased with increasing normal stress as shown in Figure 3.25. As shown in Figure 3.26, the volumetric behavior transitioned from dilation to contraction normal stress increased.

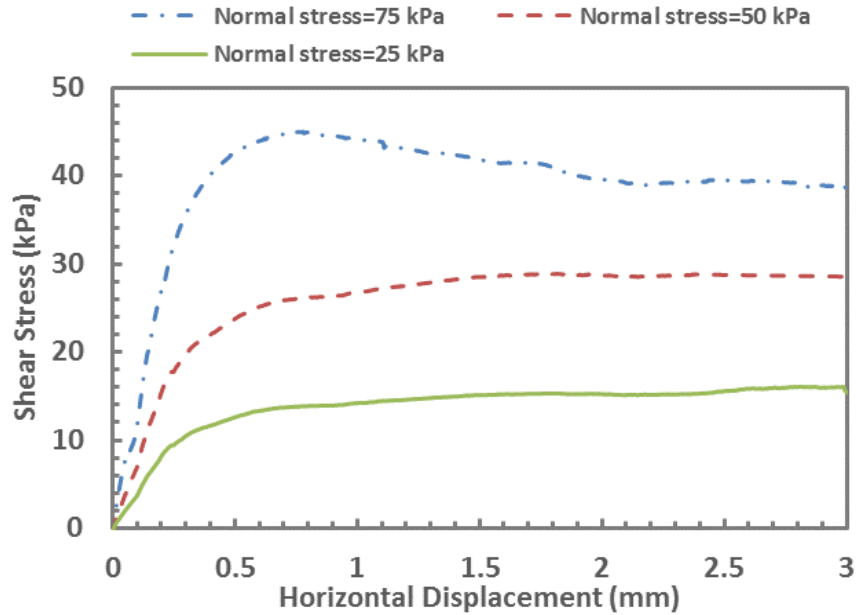


Figure 3.25. Shear stress changes during shearing at different net normal stresses and under saturated condition for soil direct shear tests

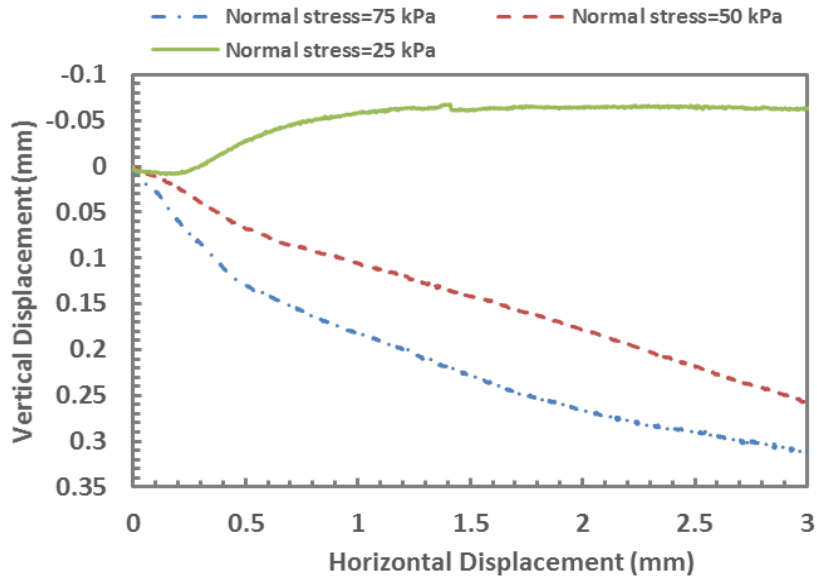


Figure 3.26. Vertical displacement versus horizontal displacement at different net normal stresses and under saturated condition for soil direct shear tests

3.10 Interface strength model for unsaturated conditions

An extended Mohr-Coulomb failure criterion is used to predict the shear strength of the interface between soil and geomembrane under the unsaturated conditions. Shear

strength variations with respect to net normal stress and suction are predicted using some parameters obtained from the experimental tests. A constitutive model based on elastoplastic behavior of interfaces is employed to predict the shear strength and volumetric behavior of the interface between geomembrane and soil under constant net normal stress and suction.

3.10.1 Extended Mohr-Coulomb criterion of unsaturated soil and interfaces

The Mohr-Coulomb failure criterion can be extended for both unsaturated soils and interfaces. Fredlund and Rahardjo (1993) proposed an equation following the Mohr-Coulomb failure criterion using as stress state variables; the matric suction and net normal stress, to predict the shear strength of soils under unsaturated conditions. An effective cohesion is substituted by an apparent cohesion into the conventional failure envelope equation. A normal stress is substituted by a net normal stress into this equation. The unsaturated shear strength equation is presented as follows:

$$\tau = c' + (\sigma - u_a) \tan \phi' + (u_a - u_w) \tan \phi^b \quad (3.3)$$

where, c' is effective cohesion, ϕ' is effective friction angle with respect to net normal stress, ϕ^b is friction angle with respect to matric suction, $(\sigma - u_a)$ is net normal stress, $(u_a - u_w)$ is matric suction, and τ is shear strength of soil.

Miller and Hamid (2009) proposed a modified form of Equation 4.3 for interface shear strength between steel and soil under unsaturated conditions, as follows,

$$\tau = c'' + (\sigma - u_a) \tan \delta' + (u_a - u_w) \tan \delta^b \quad (3.4)$$

where, δ' is the friction angle with respect to net normal stress, δ^b is friction angle with respect to matric suction and c'' is the effective adhesion intercept of the interface.

The failure envelopes are plotted in Figures 3.27 to 3.32 in the net normal stress-shear strength and matric suction-shear strength planes for soil, soil-smooth geomembrane, and soil-textured geomembrane interfaces. In Figures 3.27, 3.29, and 3.31, the slope of the failure envelope in the matric suction-shear strength plane yields the angle of internal friction with respect to suction for the interfaces and soil. The nearly parallel failure envelopes from the experimental results indicate that the average slope can be an adequate representation of angle of internal friction with respect to suction for the interfaces and soil. In Figures 3.28, 3.30, and 3.32, the slope of the failure envelope in the net normal stress-shear strength plane yields the effective friction angle with respect to net normal stress for the interfaces. These failure envelopes were nearly parallel and the effective friction angles were determined as the average of the slopes for the interfaces and soil. The intercept of failure envelopes in the net normal stress-shear strength plane at zero matric suction were used to determine the effective adhesion intercept of the interfaces and soil. These shear strength parameters for soil and interfaces are summarized in Tables 3.5 and 3.6.

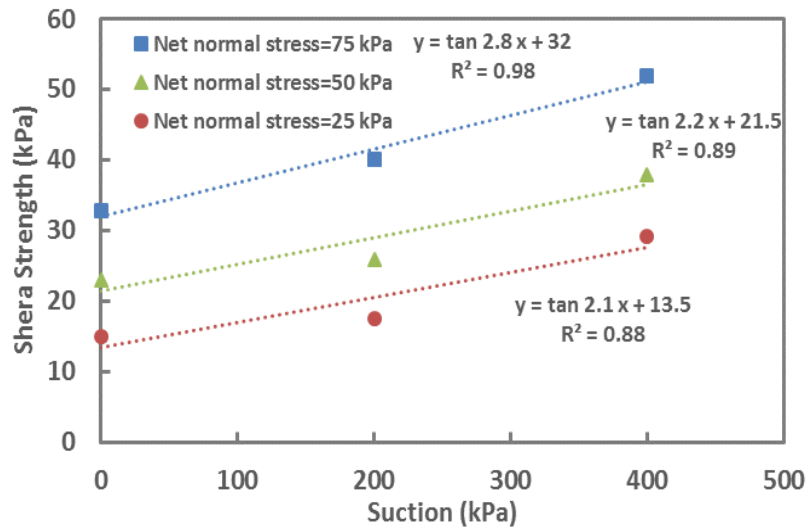


Figure 3.27. Failure envelope projections of unsaturated textured geomembrane-soil interface on suction-shear strength plane

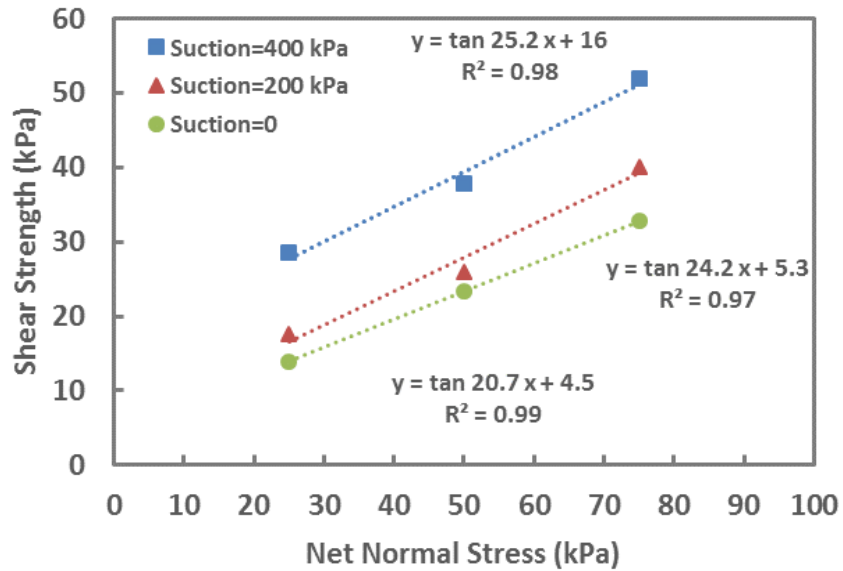


Figure 3.28. Failure envelope projections of unsaturated textured geomembrane-soil interface on net normal stress-shear strength plane

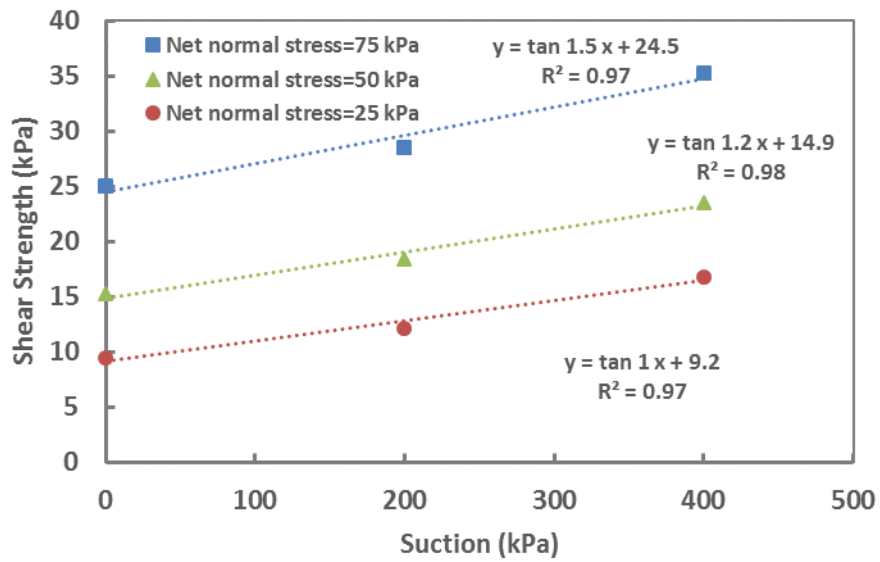


Figure 3.29. Failure envelope projections of unsaturated smooth geomembrane-soil interface on suction-shear strength plane

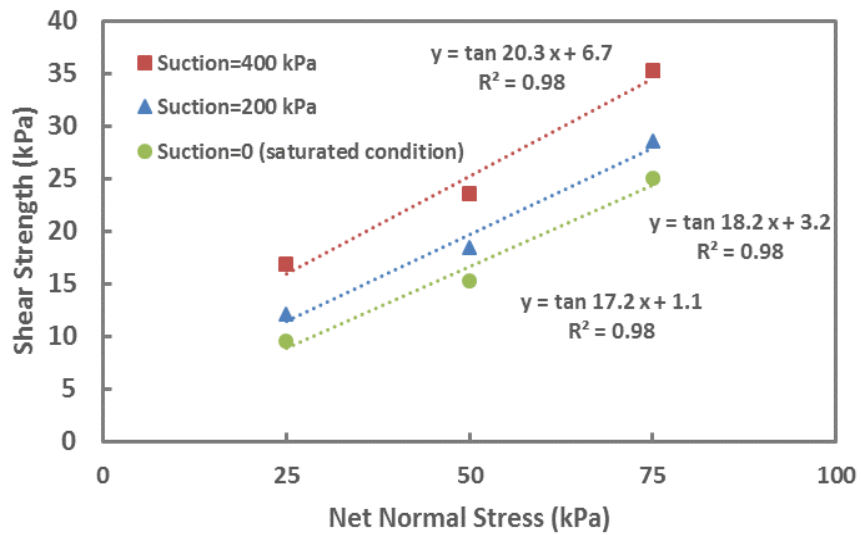


Figure 3.30. Failure envelope projections of unsaturated smooth geomembrane-soil interface on net normal stress-shear strength plane

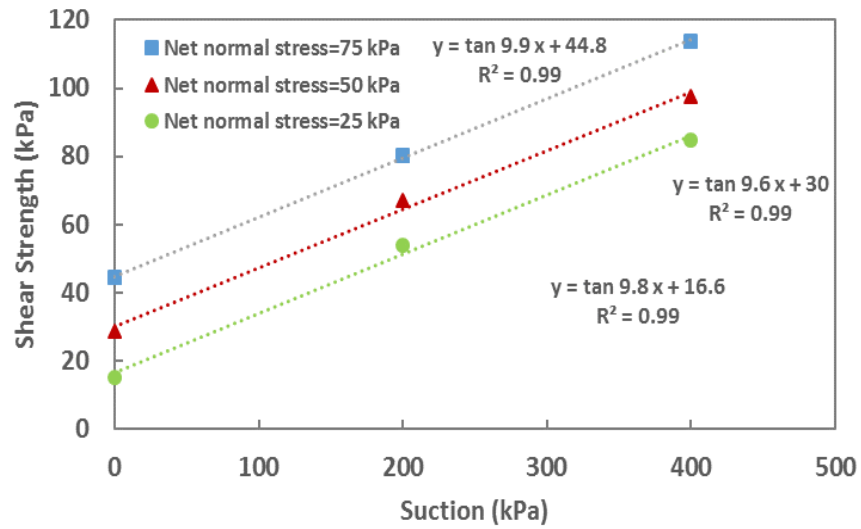


Figure 3.31. Failure envelope projections of for unsaturated soil on suction-shear strength plane

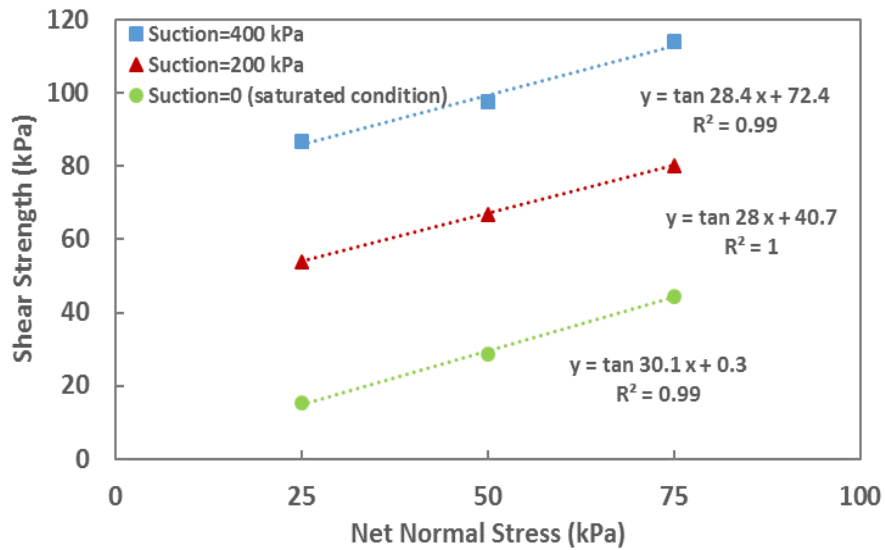


Figure 3.32. Failure envelope projections of unsaturated soil on net normal stress-shear strength plane

Table 3.5. Unsaturated shear strength parameters (c , ϕ' , ϕ^b) for soil

Material	c' (kPa)	ϕ' (deg.)	ϕ^b (deg.)
Soil	0.3	28.8	9.8

**Table 3.6. Unsaturated interface shear strength parameters (c'' , δ' , δ^b)
for soil-geomembrane interface**

Interface Type	c'' (kPa)	δ' (deg.)	δ^b (deg.)
Textured Geomembrane-Soil	4.5	23.4	2.4
Smooth Geomembrane-Soil	1.1	18.6	1.2

3.10.2 General elastoplastic constitutive model

A constitutive model modified by Hamid (2005) was selected to capture the shear strength and volumetric behavior of the unsaturated interface between soil and geomembrane. The proposed model is based on the elastoplastic theory and takes into account non-associativeness and strain-softening behavior of interfaces. The incremental constitutive equations were derived based on the flow rule and the consistency condition.

A computer code written in MATLAB by Hamid (2005) was modified for the back prediction of test results using the elastoplastic model. The resulting equations are expressed by:

$$\{d\sigma\} = [C^{ep}] \{d\varepsilon\} \quad (3.5)$$

where $\{d\sigma\}$ = vector of incremental stresses and $[C^{ep}]$ = elasto-plastic constitutive matrix. The vector $\{d\varepsilon\}$ represents increments of relative shear and normal displacements. The incremental form of the elasto-plastic stress-strain relation in the above equation can be written as,

$$\{d\sigma\} = ([C^e] - [C^p]) \{d\varepsilon\} \quad (3.6)$$

where: $[C^e]$ = is an elastic form of constitutive matrix and related to normal and shear stiffness of the interface. $[C^p]$ is a plastic form of constitutive matrix and related to yield (F) and potential (Q) and hardening (H) functions, which are defined using some experimental parameters as follows,

$$F = \tau^2 + \alpha(s)[\sigma_{net} + R(s)]^n - \gamma(s)[\sigma_{net} + R(s)]^2 \quad (3.7)$$

$$Q = \tau^2 + \alpha_Q(s)[\sigma_{net} + R(s)]^n - \gamma(s)[\sigma_{net} + R(s)]^2 \quad (3.8)$$

$$H = \left(\frac{\partial F}{\partial \xi_v} \right) \left(\left| \frac{\partial Q}{\partial \sigma_{net}} \right| \right) + \left(\frac{\partial F}{\partial \xi_D} \right) \left(\left| \frac{\partial Q}{\partial \tau} \right| \right) \quad (3.9)$$

where: F = yield function, τ = shear strength, $\sigma_{net} = \sigma_n - u_a$ = net normal stress, $R(s)$ = bonding stress, which is the increase in the strength of the unsaturated interface with the increase in suction defined as $R(s) = \lambda(s)(u_a - u_w) + \lambda^*$; the plot of $R(s)$ versus $(u_a - u_w)$ gives the slope $\lambda(s)$ and intercept λ^* . However, in this study and due to the observation that interface shear strength increased linearly with suction, $R(s)$ was defined as a linear function of suction as $R(s) = \lambda(s)(u_a - u_w) + \lambda_1 R_n + \lambda_2$; For each interface, λ^* is plotted versus R_n (defined in Equation 4.1) which provides parameters λ_1 (slope) and λ_2 (intercept). A material parameter or $\gamma(s)$ that defines the limiting state of stress is calculated as follows:

$$\gamma(s)^{1/2} = \frac{\tau_p}{\sigma_{net} + R(s)} = \mu_{p1} + \mu_{p2}R_n \quad (3.10)$$

where, τ_p = peak shear strength, the intercept and slope of $\gamma(s)^{1/2}$ versus R_n yield the material constants μ_{p1} and μ_{p2} , respectively.

A non-associative flow rule is adopted in the model to correlate the volume change behavior and loading. Parameter $\alpha(s)$ is a hardening parameter that defines the evolution of the yield surface during deformation. Dependency of parameters on matrix suction is indicated by “s” and “n” is a phase change parameter related to a state of stress at which the material passes through a state of zero volume change.

$$\alpha(s) = \gamma(s) \exp(-a\xi_v) \left(\frac{\xi_D^* - \xi_D}{\xi_D^*} \right)^b, \quad \xi_D < \xi_D^* \quad (3.11)$$

$$\alpha(s) = 0, \quad \xi_D \geq \xi_D^* \quad (3.12)$$

Parameters a, b, and ξ_D^* are functions of $R(s)$ and roughness ratio R_n .

$\xi_v = \int |dv^p|$, $\xi_D = \int |du^p|$; v^p , and u^p are the plastic displacements normal and tangential to the shearing surface, respectively, and ξ_D^* is a value of ξ_D when shear stress reaches its peak value.

By modifying the growth function, $\alpha(s)$ in the yield surface, a potential function (Q) is proposed as follows:

$$Q = \tau^2 + \alpha_Q(s) [\sigma_{net} + R(s)]^n - \gamma(s) [\sigma_{net} + R(s)]^2 \quad (3.13)$$

$$\alpha_Q(s) = \alpha(s) + \alpha_{ph}(s) \left[1 - \frac{\alpha(s)}{\alpha_i} \right] \left[1 - \kappa \left(1 - \frac{D}{D_u} \right) \right] \quad (3.14)$$

Where, and κ is a material parameter (non-associative parameter) related to the normalized roughness, net normal stress, and suction.

D is a damage function, $\alpha_{ph}(s)$ and α_i are values of $\alpha(s)$ at the phase change point and the initiation of the non-associativeness, defined as $\alpha_i = \gamma(s)(\sigma_{net} + R(s))^{2-n}$, respectively.

$D_u = \frac{\tau_p - \tau_r}{\tau_p}$, where τ_p and τ_r are the peak and residual shear stresses, respectively.

The residual shear stress is related to R_n through the model parameter μ_0 as follows:

$\tau_r = \sigma_{net} \times \mu_0 = \sigma_{net} \times (\mu_{01} + \mu_{02} R_n)$, where μ_{01} and μ_{02} are the intercept and slope of the plot of R_n versus μ_0 . The determination and meaning of the model parameters are presented in the following sections.

3.10.2.1 Ultimate or failure parameter

The ultimate parameter or $\gamma(s)$ is a ratio of the peak shear strength of unsaturated interface to the sum of two stresses including the net normal stress and the bonding stress, which is the peak shear strength of interface with respect to suction. The variation of the root square of the ultimate parameter versus surface roughness determines two parameters of the model (μ_{p1} and μ_{p2}), which are slope and intercept of the line shown in Figure 3.33.

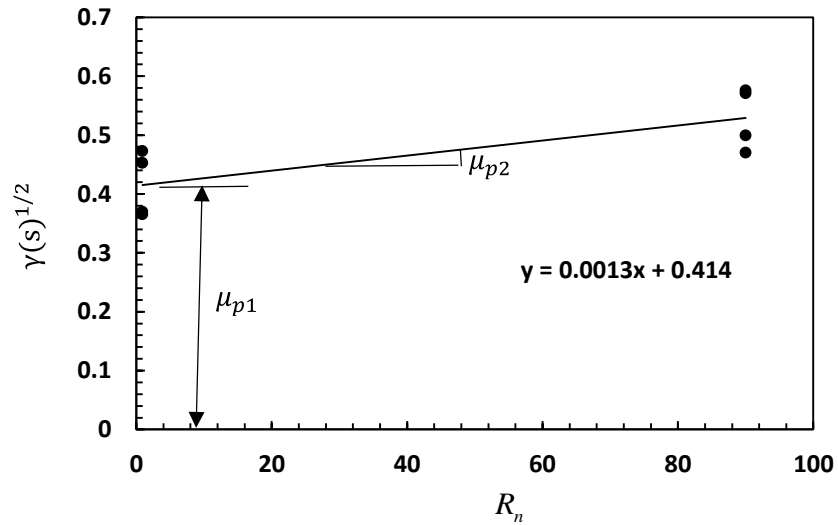


Figure 3.33. Typical plot for determination of factors for ultimate parameter

3.10.2.2 Bonding stress

The bonding stress or $R(s)$ is a portion of interface peak shear strength, which is a function of matric suction. The linear variation of the bonding stress versus suction for different interfaces shown in Figure 3.34 provides two parameters, which are the intercept, λ^* , and the slope, $\lambda(s)$, of the line. The variation of the intercept versus the surface roughness gives two parameters of the model (λ_1 and λ_2), which are the slope and the intercept of the line shown in Figure 3.35.

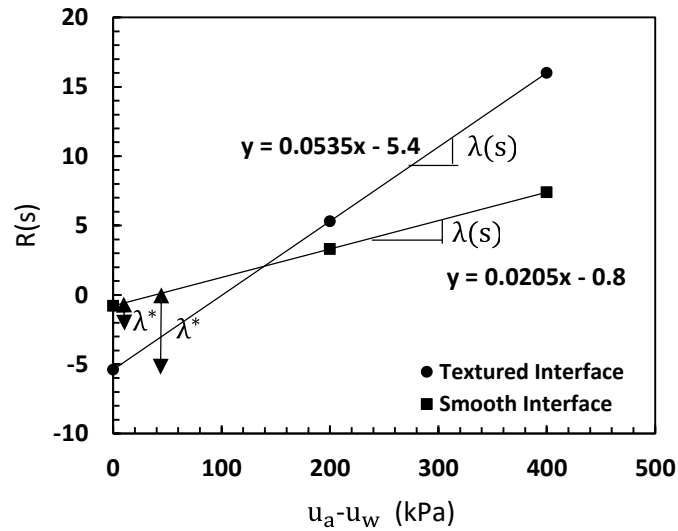


Figure 3.34. Typical plot for determination of factor λ^* for bonding stress

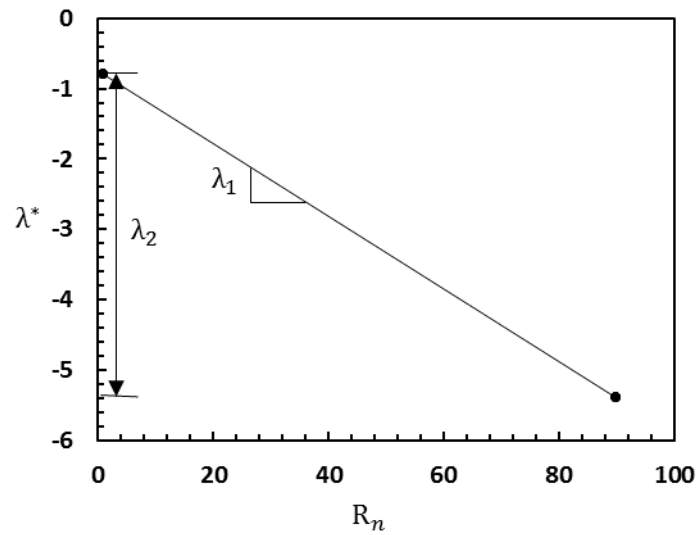


Figure 3.35. Typical plot for determination of factors λ_1 and λ_2 for bonding stress

3.10.2.3 Phase change parameter

The phase change parameter or “n” is used to transition the vertical displacement from contraction to dilation during the shearing phase. The phase change parameter is obtained from the following equation, which is a modified form of equation proposed by Wathugala (1990).

$$\frac{\gamma_1^{1/2}}{\gamma(s)^{1/2}} = \left[\frac{(n-2)}{n} \right]^{1/2} \quad (3-15)$$

Where, $\gamma(s)^{1/2}$ is the slope of the ultimate state, and $\gamma_l^{1/2}$ is the slope of the line connecting the crest of all the yield surfaces.

3.10.2.4 Hardening parameters

ξ_{D1}^* , ξ_{D2}^* , a , and “ b ” are the hardening parameters, which are obtained from the slope and the intercept of the lines shown in Figures 3.36 and 3.37. The experiments showed that the accumulation of plastic tangential displacement is the function of suction and surface roughness and it can be expressed as the following relationship:

$$\xi_D^* = \xi_{D1}^* + \xi_{D2}^* \left[R_n + \frac{R(s)}{P_a} \right] \quad (3-16)$$

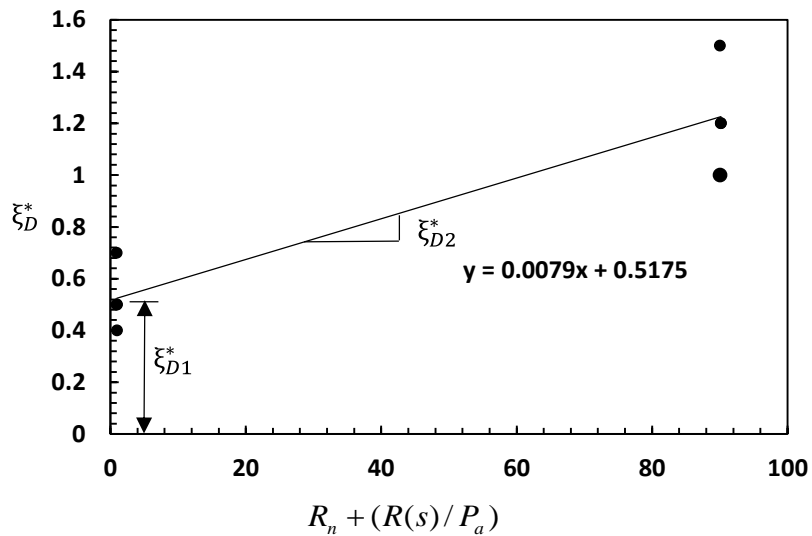


Figure 3.36. Typical Plot for determination of factors for hardening parameter from the experimental results

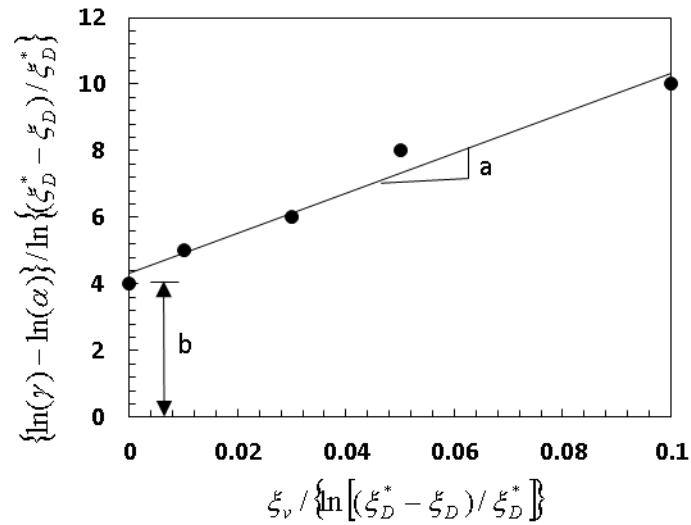


Figure 3.37. Typical plot for determination of “a” and “b” as hardening parameters from rough interface test results

3.10.2.5 Non-associative parameter

The non-associative parameter or κ is obtained from the procedure described by Navayogarajah (1990) and is determined using the following equation and Figure 3.38.

$$\kappa = -[\gamma(s)]^{-\frac{1}{2}} * \left(\frac{dv^p}{du^p}\right) \quad (3.17)$$

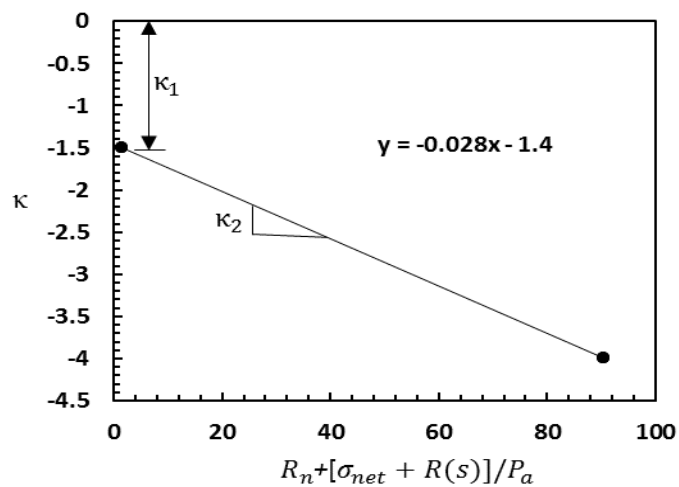


Figure 3.38. Typical plot for determination of κ for suction of 200 kPa for rough interface

3.10.2.6 Residual parameter

Experimental results indicated that the residual shear stress was dependent on suction and net normal stress, therefore, the residual parameter, μ_0 , is expressed based on the following relationship:

$$\mu_0 = \frac{\tau_r}{[\sigma_{net} + R(s)]} = \mu_{01} + \mu_{02}R_n \quad (3.18)$$

Where, μ_{01} and μ_{02} are the slope and the intercept of the line shown in Figure 3.39.

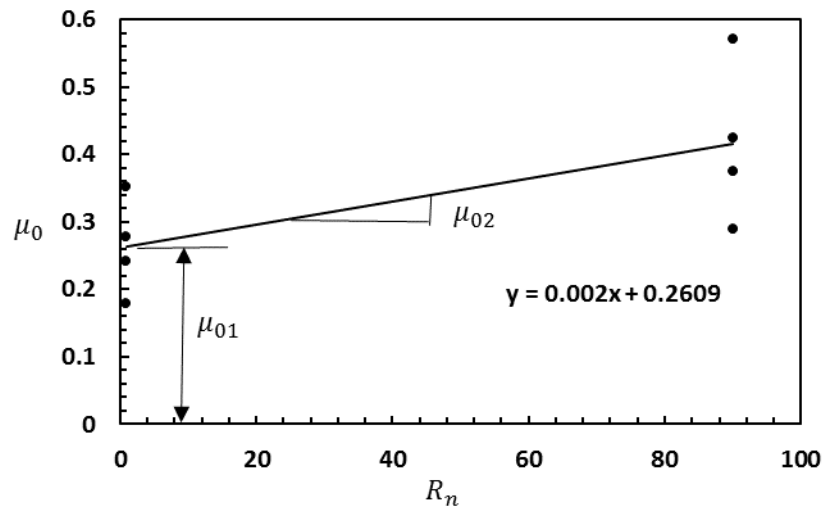


Figure 3.39. Typical plot for determination of residual parameters

3.10.3 Application of the constitutive model to the unsaturated soil-textured geomembrane interface test results

The model parameters for the textured geomembrane-soil interface were obtained based on the procedure discussed in the previous section. A Summary of the constitutive model parameters is shown in Table 3.7.

Table 3.7. Model Parameters for the unsaturated textured geomembrane-soil Interface

Parameter	Value
ξ_{D1}^* (mm)	0.51
ξ_{D2}^* (mm)	0.007
μ_{p1}	0.41
μ_{p2}	0.001
n	2.1
κ_1	2.6
κ_2	-0.028
μ_{01}	0.26
μ_{02}	0.002
$\lambda_1(s)$	-0.1
$\lambda_2(s)$	10
a	60
b	4
K_n (kPa)	365
K_s (kPa)	35

Figures 3.40(a) and 3.41(a) indicate a comparison between the predicted and measured results of shear stress (τ) versus horizontal shear displacement (u) for the textured geomembrane-soil interface conducted in this study subjected to different suction and net normal stress values. The comparison revealed that the model was capable of capturing the behavior of the unsaturated textured geomembrane-soil interface with reasonable accuracy. The following observations were made with respect to the model results:

1. The peak shear strength of textured geomembrane-soil interface increased with suction and net normal stress. However, the slope of predicted shear stress curves was observed to be different from the corresponding results of the experimental tests.
2. Strain softening was more pronounced at higher suction and lower net normal stress values.

Figures 3.40(b) and 3.41(b) show the predicted and measured results of vertical displacement versus horizontal shear displacement (u) for different suction and net normal stresses. Important volume change behavior of unsaturated textured geomembrane-soil interfaces was captured using this model:

1. Unsaturated textured geomembrane-soil interface predictions generally followed the overall trend (mostly dilation) of volume change behavior. However, in most cases experimental results showed a slight amount of compression following dilation that the model did not capture well.
2. Specimens did not show any dilation in saturated conditions for both predicted and measured results.

— Net normal stress=75 kPa (Experimental Results) - - - Net normal stress=75 kPa (Model Predictions)
— Net normal stress=50 kPa (Experimental Results) - - - Net normal stress=50 kPa (Model Predictions)
— Net normal stress=25 kPa (Experimental Results) - - - Net normal stress=25 kPa (Model Predictions)

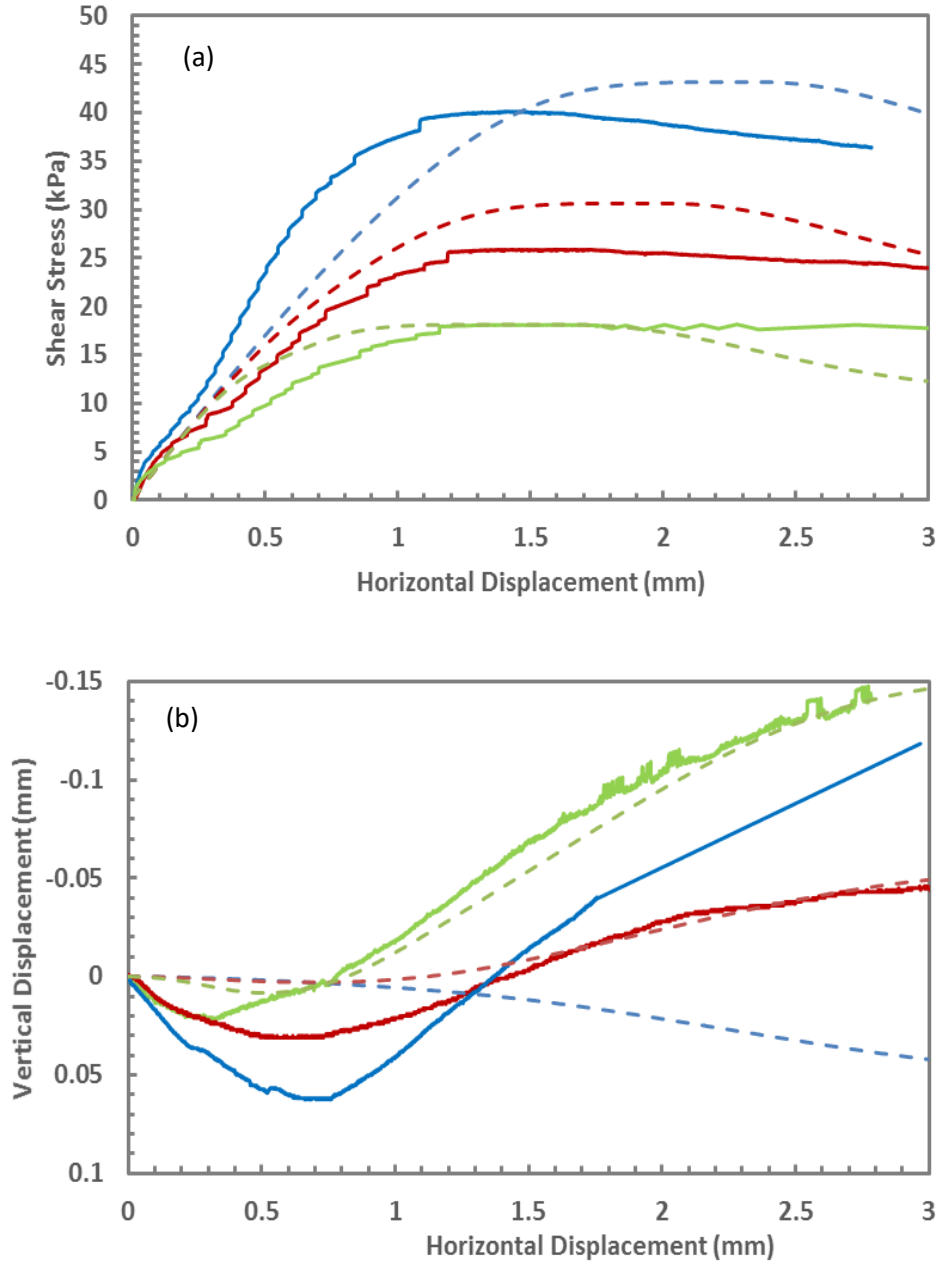


Figure 3.40. A Comparison of Experimental and Predicted Results for Textured geomembrane and soil Interface Shear Test at Suction=200 kPa, shear strength behavior (a) and volumetric behavior (b).

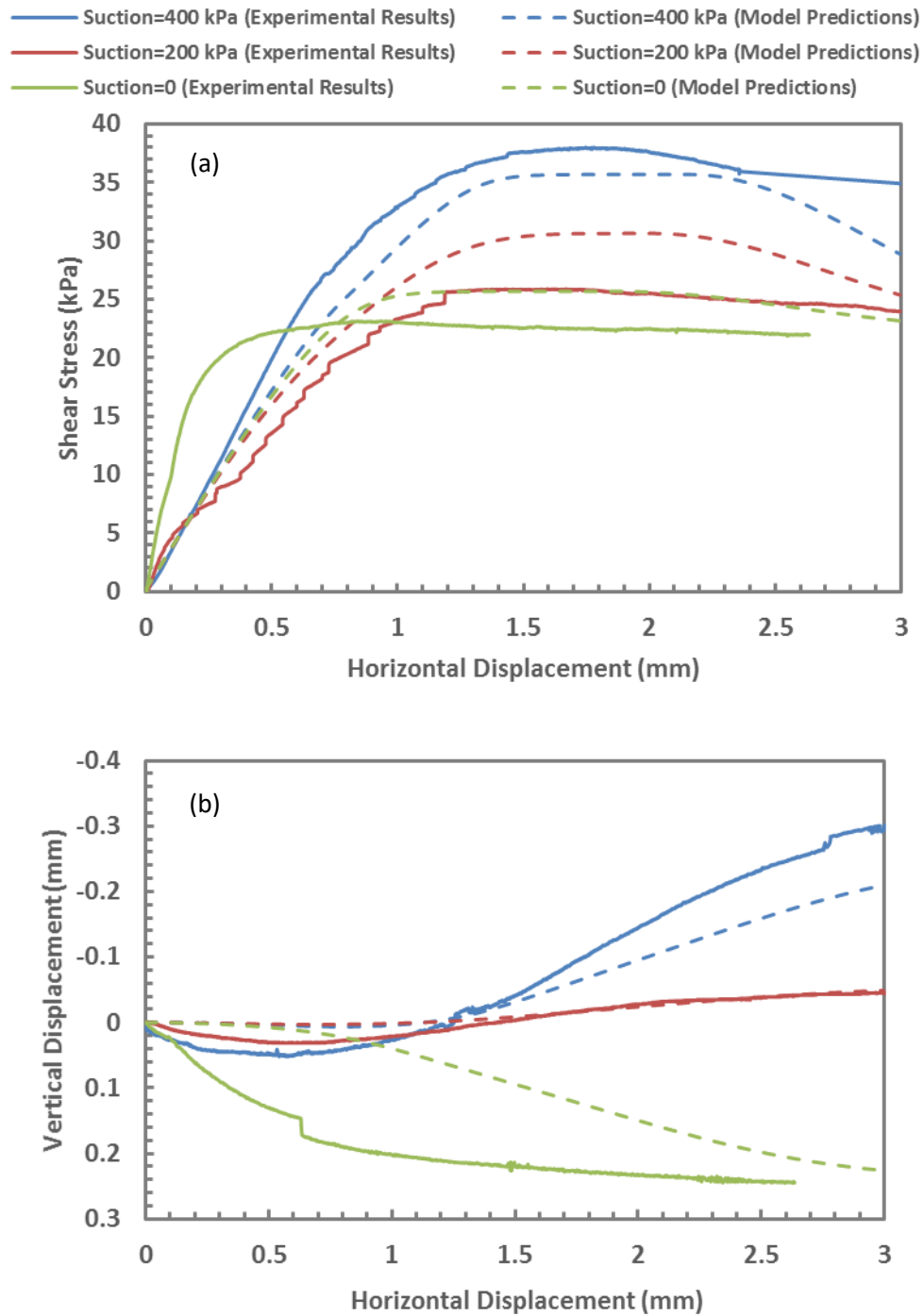


Figure 3.41. A comparison of experimental and predicted results for textured geomembrane and soil interface shear test at net normal stress=50 kPa, shear strength behavior (a) and volumetric behavior (b).

3.10.4 Application of the constitutive model to the unsaturated soil-smooth geomembrane interface test results

The model parameters for the smooth geomembrane-soil interface were obtained based on the procedure discussed in the previous section. A Summary of the constitutive model parameters is shown in Table 3.8.

Table 3.8. Model Parameters for the unsaturated textured geomembrane-soil Interface

Parameter	Value
ξ_{D1}^* (mm)	0.51
ξ_{D2}^* (mm)	0.007
μ_{p1}	0.32
μ_{p2}	0.001
n	2.1
κ_1	0.01
κ_2	-0.028
μ_{01}	0.26
μ_{02}	0.002
$\lambda_1(s)$	-0.05
$\lambda_2(s)$	5
a	60
b	4
K_n (kPa)	365
K_s (kPa)	35

Figures 3.42(a) and 3.43(a) indicate a comparison between the predicted and measured results of shear stress (τ) versus horizontal shear displacement (u) for the smooth geomembrane-soil interface conducted in this study subjected to different suction and net normal stress values. The comparison revealed that the model was capable of capturing the behavior of the unsaturated smooth geomembrane-soil interface with reasonable accuracy. The following observations were made:

1. The peak shear strength of smooth geomembrane-soil interface increased with suction and net normal stress.

2. Strain softening was more pronounced at higher suction and higher net normal stress values.

Figures 3.42(b) and 3.43(b) show the predicted and measured results of vertical displacement versus horizontal shear displacement (u) for different suction and net normal stresses. Important volume change behavior of unsaturated smooth geomembrane-soil interfaces was captured using this model:

1. Unsaturated smooth geomembrane-soil interface predictions generally followed the overall trend of volume change behavior. However, in most cases experimental results showed a slight amount of dilation following compression that the model did not capture.
2. Specimens did not show significant dilation for both experimental and computational results.

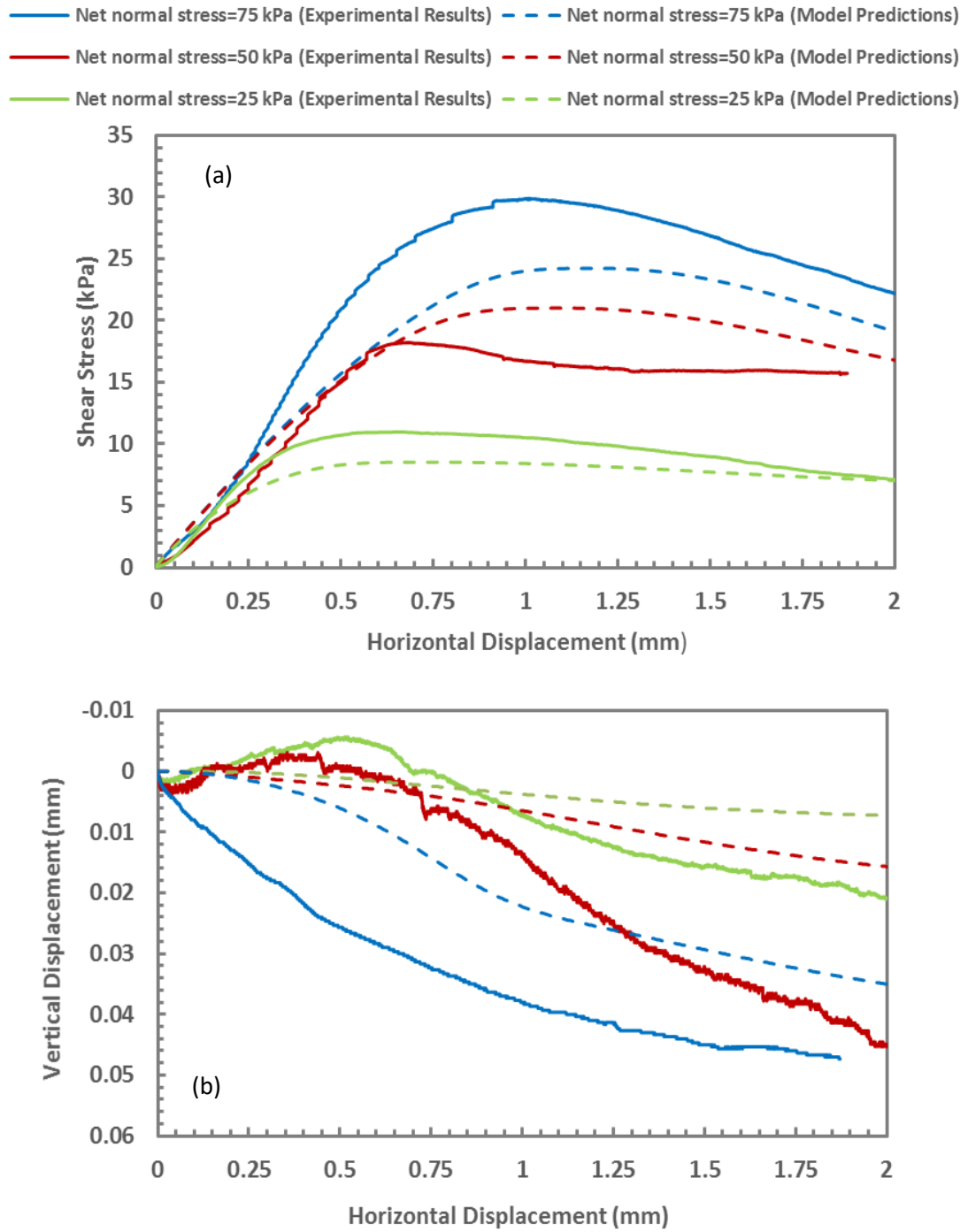


Figure 3.42. A comparison of experimental and predicted results for smooth geomembrane and soil interface shear test at suction=200 kPa, shear strength behavior (a) and volumetric behavior (b).

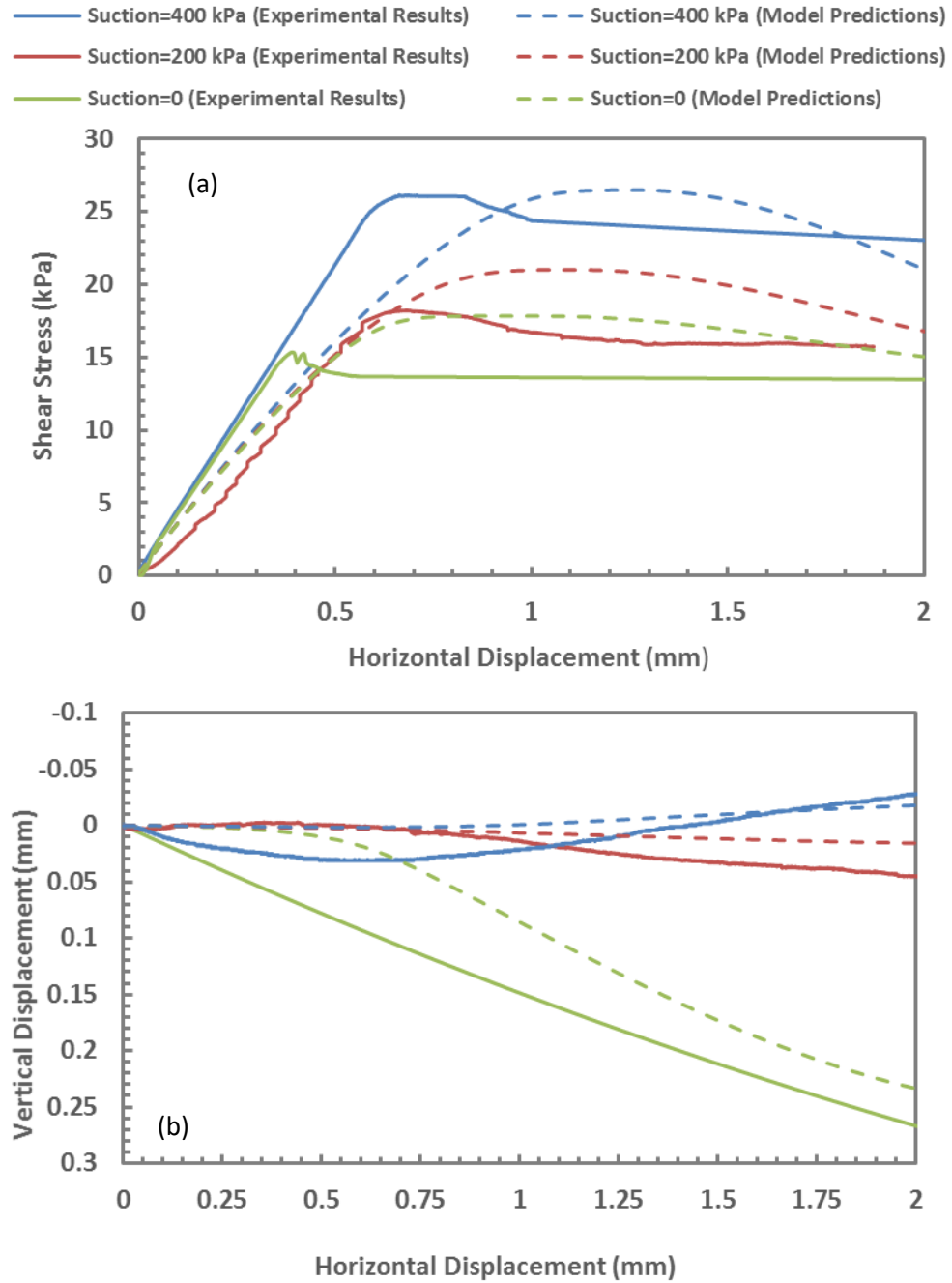


Figure 3.43. A comparison of experimental and predicted results for smooth geomembrane and soil interface shear test at net normal stress=50 kPa, shear strength behavior (a) and volumetric behavior (b).

CHAPTER 4: Modeling lateral load behavior of piles in unsaturated soil due to seasonal moisture content changes

4.1 Background

Piles are the component of an integral abutment bridge (IABs) that transfers superstructure loads to resistant layers of soil and/or rock. Unlike conventional bridges, IABs are a special type of bridge, which transfer thermally induced lateral loads directly from superstructure to substructure due to the elimination of expansion joints within the bridge deck or between superstructure and abutment. As shown in the sketch of an IAB in Figure 4.1, bridge girders are embedded within the concrete of the abutment and as the structure is heated and cooled the abutment must move outward and inward, respectively, to accommodate the expansion and contraction of the bridge. This creates a daily and seasonal cyclic loading sequence on the piles and soil in contact with the piles and abutment. The stiffness of the abutment backfill and soil surrounding the piles, in addition to the bending stiffness of the piles, is critically important to the lateral load behavior of the piles and bridge system. Ideally, the system should be relatively flexible to accommodate thermal expansion without producing excessive stresses in the piles and bridge structure. The research presented in this chapter focuses on the impact of the soil stiffness on the lateral load behavior of the piles. In particular, the soil moisture conditions have an important influence on the soil stiffness because the soil matric suction will increase or decrease in response to decreasing or increasing moisture content.

As shown in Figure 4.1, generally, components of IABs include deck, abutments, piles, soil behind abutments, and soil surrounding piles, which interact with each other

during loading over the service life of the bridge. In addition to vertical loads, such as self-weight and traffic loads, the horizontal loads due to temperature changes are also governing factors in designing an integral bridge. Deformation of a bridge abutment due to thermal loading appears in different forms, including lateral translation and rotation of the abutment.

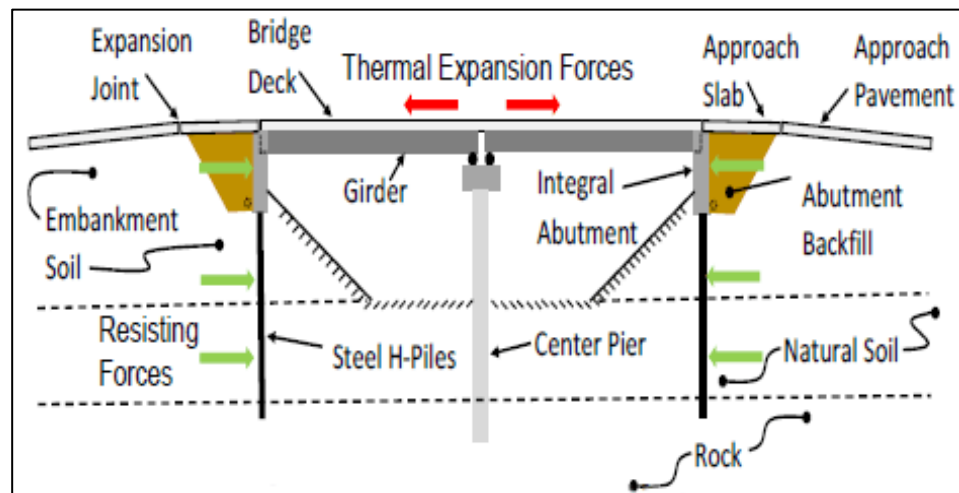


**Figure 4.1. A sketch of Integral Abutment Bridge (IAB)
(from Muraleetharan and Miller 2015)**

A summarized survey conducted by Kirupakaran (2013) showed that the design and construction of IABs were varied from state to state in the USA. According to this study, piles were commonly installed either oriented for weak axis bending or strong axis bending. The pile-abutment connections in IABs were either free, fixed, or partially restrained against rotational movements due to lateral loadings. The length of bridges, depending on the materials used, were variable from 121.9 m and 282.5 m for steel girder and concrete girder bridges, respectively.

Ng et al. (1998) recognized the movement of an integral abutment as translational, rotational, and bending deflections. Abutment translation is mobilized as

a relative displacement at the top and base of abutment, and rotational deflection occurs at the base of abutment. The abutment bending appears as different tangents along the height of abutment. Expansion and contraction of integral bridge decks due to thermal loading are accommodated by backfill-abutment and foundation soil-pile interactions. The earth pressure behind the backfill and around the piles can build up due to deck expansion or reduce by deck contraction (Arsoy et al. 2004).

Soil-pile interaction analysis in saturated conditions has been investigated by numerous researchers. A few numerical and experimental studies have been conducted in unsaturated soil-pile interaction analysis (Mokwa et al. 2000, Georgiadis et al. 2003, Weaver and Grandi 2009, and Hamilton 2014). A common method for analyzing lateral load behavior of piles involves a finite difference solution of the equation for bending of a vertical beam embedded in soil analogous to the beam on elastic foundation problem, also known as a “Winkler” foundation. As illustrated in the sketch of Figure 4.2, the soil interaction with the pile occurs at nodal points and is represented by a non-linear spring, where the behavior of the spring is defined by a load (p)-displacement (y) response curve, i.e., a p - y curve. The p - y curve depends on soil properties and can be modified to account for variations in soil matric suction. A computer program called “LPILE” was used to conduct the single pile lateral load analysis presented in this dissertation. LPILE is available from Ensoft, Inc. and has become an industry standard in geotechnical engineering for single pile lateral load analysis.

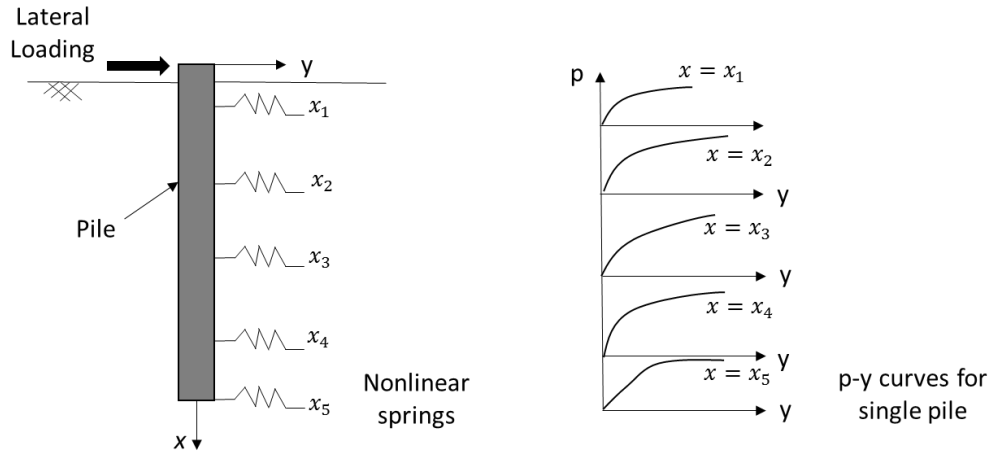


Figure 4.2. A sketch of Winkler springs (p-y curves) for pile-soil interaction models

The p-y curve for c- ϕ soil proposed by Evans and Duncan (1982) and as incorporated in LPILE consists of combining soil resistance from the Reese et al. (1974) sand p-y curve and Matlock (1970) clay p-y curve. The early portion of the p-y curve is obtained by the soil modulus at small displacements. The soil modulus is the product of the modulus coefficient, k, and the depth below the ground surface. The modulus coefficient for sand and clay are based on friction angle and cohesion, respectively. To draw a p-y curve using this method, two restricted points on the displacement axis are defined in which the peak soil resistance and the residual soil resistance take place. The displacement coordinates of $y=b/60$ and $y=3b/80$ (b = foundation diameter) are where the peak and residual soil resistance occur, respectively. It is also assumed that the soil resistance decreases from the peak to the residual linearly.

Mokwa et al. (2000) proposed the following equation using a cubic parabola:

$$p = 0.5p_{ult} \left[\frac{y}{A\epsilon_{50}D} \right]^{0.33} \quad (4-1)$$

where p is the soil resistance, p_{ult} is the ultimate resistance, y is the lateral foundation displacement at a particular depth, A is an empirical coefficient, ϵ_{50} is the strain at 50 %

of the ultimate soil strength obtained from a triaxial shear test, and D is the foundation diameter. The ultimate soil resistance, p_{ult} , is calculated using Brinch-Hansen's theory (1961) and modified based on results from full-scale tests. The equation of p_{ult} is as follows:

$$p_{ult} = M\gamma_m DzK_q + McDK_c \quad (4-2)$$

where M is an empirical modification factor = 0.85, γ_m is the soil moist unit weight, D is the foundation diameter, z is the depth below the ground surface, K_q is a coefficient for the frictional component of the soil resistance, c is the soil cohesion and K_c is a coefficient for the cohesive component of the soil resistance. Five load tests conducted on relatively short drilled shaft foundations embedded in unsaturated silty (ML and MH) and clayey (CL and CH) soils were used to back-calculate the parameters required for the above equations.

The influence of partial saturation on the axial capacity of a pile was studied by Georgiadis et al. (2003) in which they determined that the load capacity (ultimate pile load) increased as the degree of saturation decreases. The analysis also showed an excessive settlement due to collapse exhibited by the unsaturated soil under the tip of the pile. This settlement was perhaps attributed to wetting-induced collapse behavior of unsaturated soils (Miller et al. 2001). It was important to note that this settlement could not be recognized with saturated finite element analysis (Georgiadis et al. 2003).

Weaver and Grandi (2009) used a finite element program to compare the lateral resistance via deformation curves (p - y curves) with those obtained by Evans and Duncan (1982), and Mokwa et al. (2000). The apparent cohesion was used instead of the drained

cohesion using the concept of unsaturated soil mechanics. The method proposed by Evans and Duncan (1982), which was included in the computer program LPILE (2004) presented some parameters to capture a p-y curve associated with cohesion and friction angle. The soil moduli used for finite element analysis were obtained using the modulus coefficient, k , which was identical to the “ k ” proposed by Evans and Duncan (1982) in LPILE. The modulus coefficient for unsaturated soil was considered as a combination of the modulus coefficient for cohesive and cohesionless soil. They have found that lateral pile design in a saturated condition would not be conservative as it is in the other soil-structure interaction problems. The unsaturated lateral pile deformations were significantly smaller than those captured from a saturated condition, resulting in higher bending moments in pile.

Hamilton (2014) used a concept of suction stress to obtain the effective stress required for capturing the p-y curve. Suction stress concept proposed by Lu et al. (2010) is an extension of Bishop’s equation for the effective stress that uses the suction stress characteristic curve (SSCC). This curve only requires two controlling parameters: the inverse of the air entry value and pore size spectrum number. The degree of saturation was assumed to be constant through the soil layer. It was concluded that the least amount of deformation occurred in the middle range of saturation because of greater effective stress.

4.2 Historical and future weather data collection

Historical weather data can be obtained in Oklahoma from Mesonet stations or weather stations installed at research sites. The Historical weather data measured through

equipment installed in weather stations include: precipitation, air temperature, relative humidity, total solar radiation, and wind speed. As a case study, the historical weather data were collected from a station close to an IAB site under study (I-44 Bridge in Oklahoma). Among the above-mentioned data from the weather station only precipitation and air temperature on a monthly basis are available from climate projections of future weather. The projected weather data can be downloaded from the U.S. Geological Survey (USGS) using the National Climate Change Viewer (NCCV). The monthly average air temperature and precipitation data from 1950 to 2099, shown in Figures 4.3 and 4.4, were obtained for a location in Comanche county, OK, where the I-44 Bridge is located.

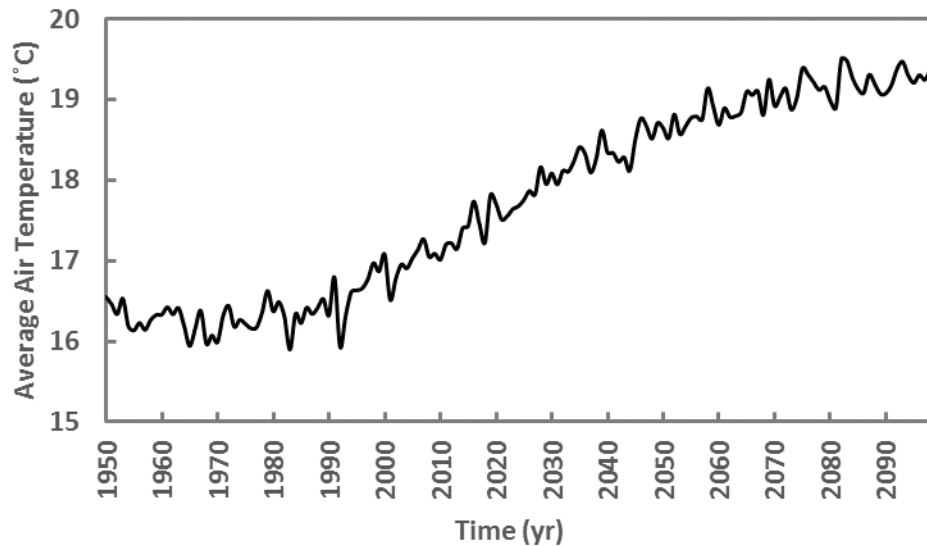


Figure 4.3. Average air temperature from 1950-2099 available in Comanche county, OK (data obtained from USGS via the National Climate Change Viewer)

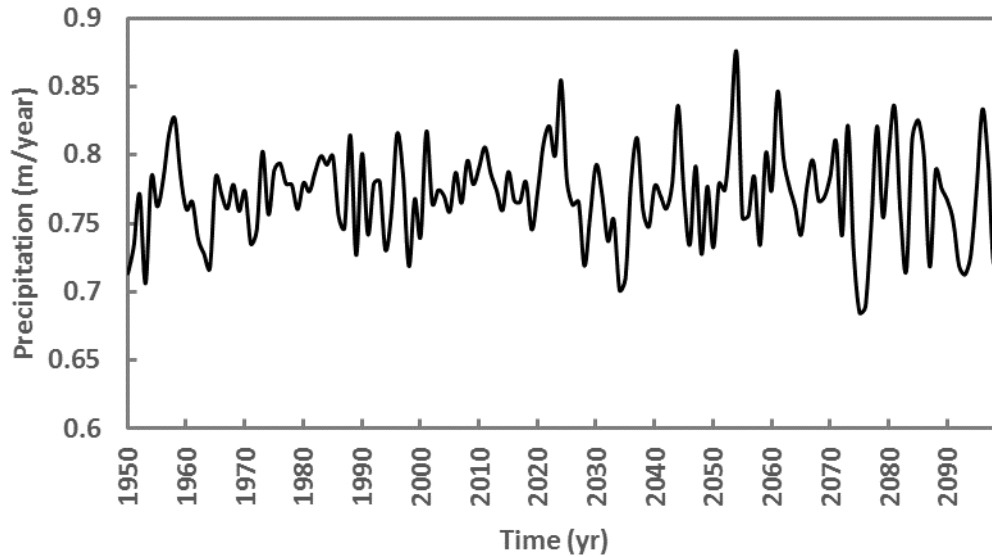


Figure 4.4. Average precipitation from 1950-2099 available in Comanche county, OK (data obtained from USGS via the National Climate Change Viewer)

In addition to precipitation data, the potential evaporation and transpiration are required to predict the moisture variations in foundation soil and abutment backfill material in a typical IAB. The potential evaporation can be determined in different ways including measured data, calculated with Penman’s equation (1948), calculated with Thornthwaite’s equation (1948), and calculated with Priestley-Taylor’s equation (1972).

Among the above-mentioned equations, Thornthwaite’s equation (1948) is the only one that functions on a single parameter, the monthly air temperature and some empirical parameters as shown in Equation 6-3. Since available data for the future are limited to monthly maximum and minimum air temperature, Thornthwaite’s equation (1948) was selected as the method to predict the moisture changes for the current research. The equation is,

$$PET=1.6 L_d \left(\frac{10T}{I}\right)^a \quad (4-3)$$

where: PET is the monthly potential evapotranspiration (cm), L_d is the daytime length or time from sunrise to sunset in multiples of 12 hours, T is the monthly mean air temperature(°C),

$$a = 6.75 \times 10^{-7} I^3 - 7.71 \times 10^{-5} I^2 + 0.01791I^1 + 0.49239,$$

and I is the annual heat index, which is computed from the monthly heat indices.

$$I = \sum_{j=1}^{12} i_j, \quad i_j = \left(\frac{T_j}{5}\right)^{1.514} \quad (4-4)$$

T_j is the mean air temperature in °C for month j for $j = 1$ to 12.

To compare and partially validate the results obtained using Thornthwaite's method (1948), Penman's method (1948) having more variables, such as relative humidity, solar radiation, and wind speed as well as air temperature was used to calculate the potential evaporation using historical data and compared to Thornthwaite based predictions. The Penman model predicts potential evaporation as shown in the following equation,

$$PE = \frac{\Gamma Q_n + \eta E_a}{\Gamma + \eta} \quad (4-5)$$

where: PE is potential evaporation in m/day, E_a is flux, which is calculated in m/day using Equation 6-6, Q_n is net radiation at the water surface in m/day, Γ is slope of saturation vapor pressure vs. temperature curve in kPa/°C, η is the psychrometric constant equal to 0.06733 kPa/°C.

$$E_a = 0.35(1 + 0.146 W_w) C_f u_{v0}(1 - h_r) \quad (4-6)$$

where: W_w is wind speed in km/hr, C_f = conversion factor, u_{v0} is saturated vapor pressure in the mean air temperature with the units of kPa, and h_r is relative humidity in the air above the ground.

Evaporation associated with transpiration, which is a process of water migration through a plant results in evapotranspiration. The amount of water is controlled by transpiration through parameters such as bare soil potential evaporation, leaf-area index (LAI), plant limiting function (PLF), which is related to soil suction, and the root zone profile. Since these parameters were not routinely available for the sites considered, some assumptions were used to incorporate them in the numerical modeling.

There is an atmospheric moisture flux balance that must be satisfied at the ground surface when calculating actual evaporation. The water on the ground surface either infiltrates the soil (or runs off) or rises to the sky through the process called actual evaporation. Actual evaporation used in an atmospheric moisture flux balance for Thornthwaite (1948) method was assumed to be equal to potential evaporation, which is a maximum amount of evaporation. In contrast, a modified Wilson-Penman's method (1994) was used for calculation of actual evaporation in Penman's method (1948).

4.3 Predicting soil moisture changes using unsaturated seepage modeling

SVFLUX, developed by SoilVision Systems Ltd. (2012), is a finite element program used to model transient flow of water, heat, and vapor in unsaturated soil. The program has been built around fundamental equations governing the exchange of water between the soil and atmosphere at the ground surface (e.g. Penman 1948, Wilson et al. 1994)

and it can account for variations in the soil state (dry, frozen, saturated, unsaturated), soil type, soil temperature, extent, and type of vegetative cover among other things.

Basically, the user is required to input a number of different parameters that govern the movement and storage of water (in liquid and vapor forms) within a soil profile as well as information about the type and temporal variation of vegetative cover at the site. In addition, the initial soil moisture conditions in the profile are required. The output generated from the program provides predicted moisture (and suction) profiles as a function of time.

The parameters required for the analysis using the program are divided into four categories: precipitation data, evaporation data, vegetation data, and soil data. As for the output, the programs are used to provide variations in volumetric water content over time at specific depths in the soil profiles. A geometry similar to the southern embankment for the I-44 Bridge adopted for the purpose of seepage modeling is shown in Figure 4.5 including the soil foundation and backfill. While this 2-D representation of the embankment and abutment does not capture the three-dimensional features of the pavement and sloped vegetated embankment surfaces next to the pavement, it provides a starting point for examining unsaturated seepage in the embankment and backfill behind the abutment. In the model, the ground surface behind the abutment to the left side of pile axis in Figure 4.5 was treated as the flux boundary that was subjected to atmospheric conditions based on real local weather data.

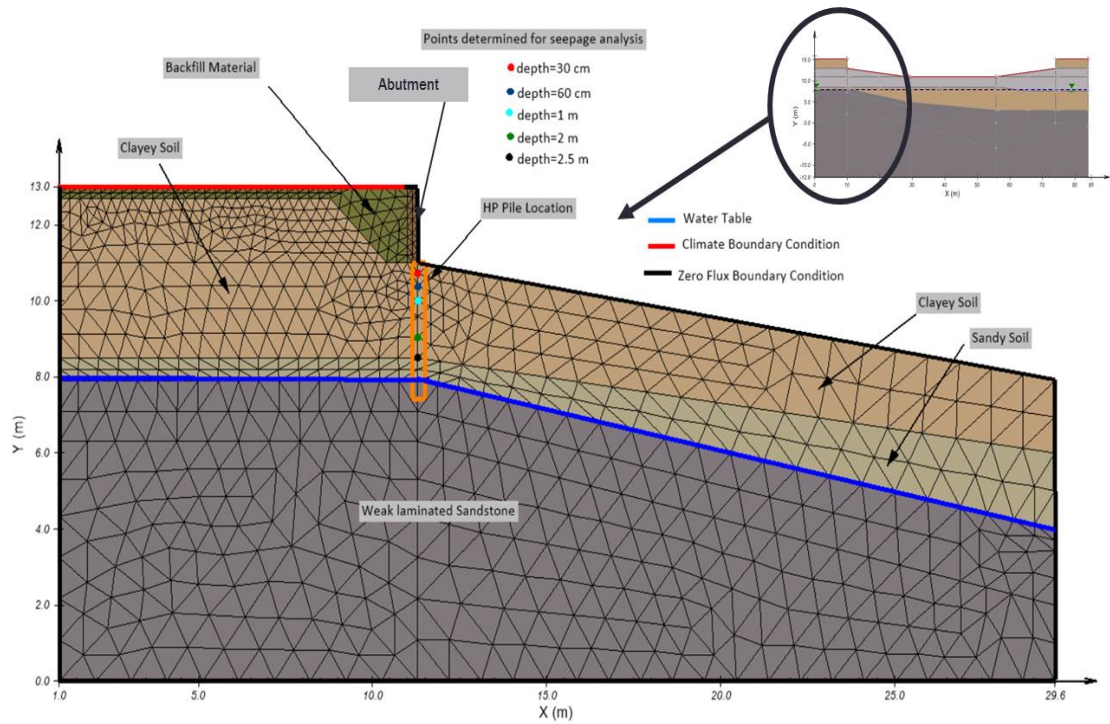


Figure 4.5. Geometry and initial condition of south abutment of I-44 Bridge

Historical weather data available from the Mesonet for 1994 to 2001 (7 years) at Comanche county, Medicine park, OK, which was close to the I-44 bridge was downloaded, to use as the atmospheric loading on the ground surface. As a starting point, the boundary condition on the sloped ground surface located at the right side of pile axis, under the bridge, was assumed to be impermeable. However, as this surface was under shaded condition due to the bridge deck location a modified atmospheric loading can be defined in the parametric study. The soil water characteristic curve (SWCC) was assumed using Zapata's model (1999), which was based on the grain size distribution (percent of passing #200) and plasticity index (PI) as shown in Figure 4.6 for clayey layer.

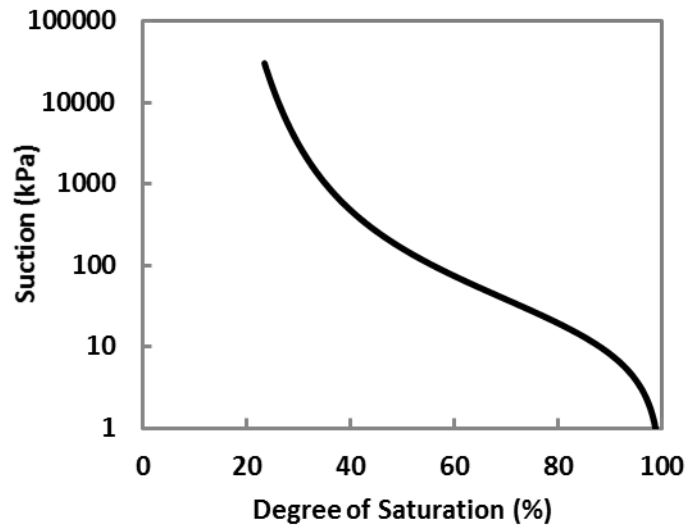


Figure 4.6. Soil Water Characteristic curve (SWCC) for clayey soil

The saturated permeability of backfill, sandy, and clayey layers were assumed to be 1×10^{-6} , 1×10^{-7} , and 1×10^{-8} m/s, respectively. The assumptions were made based on the classification of soils as low and very low degrees of permeability (Terzaghi and Peck, 1967). The infiltration and evaporation and transpiration components from the local weather station are shown in Figures 4.7, 4.8 and 4.9.

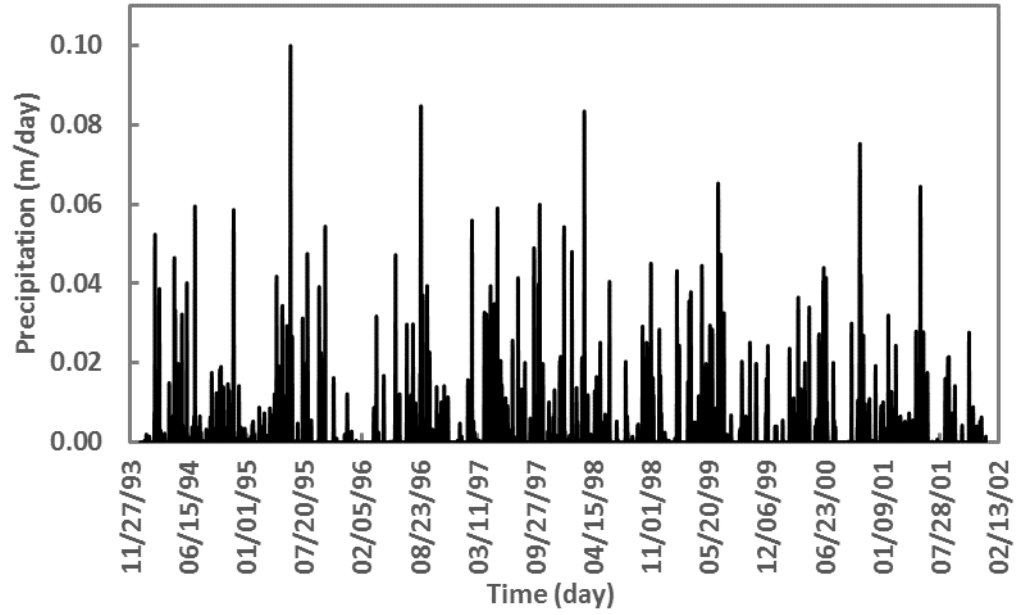


Figure 4.7. Daily Precipitation data from 1994 to 2001 (from Oklahoma Mesonet Station Medicine Park)

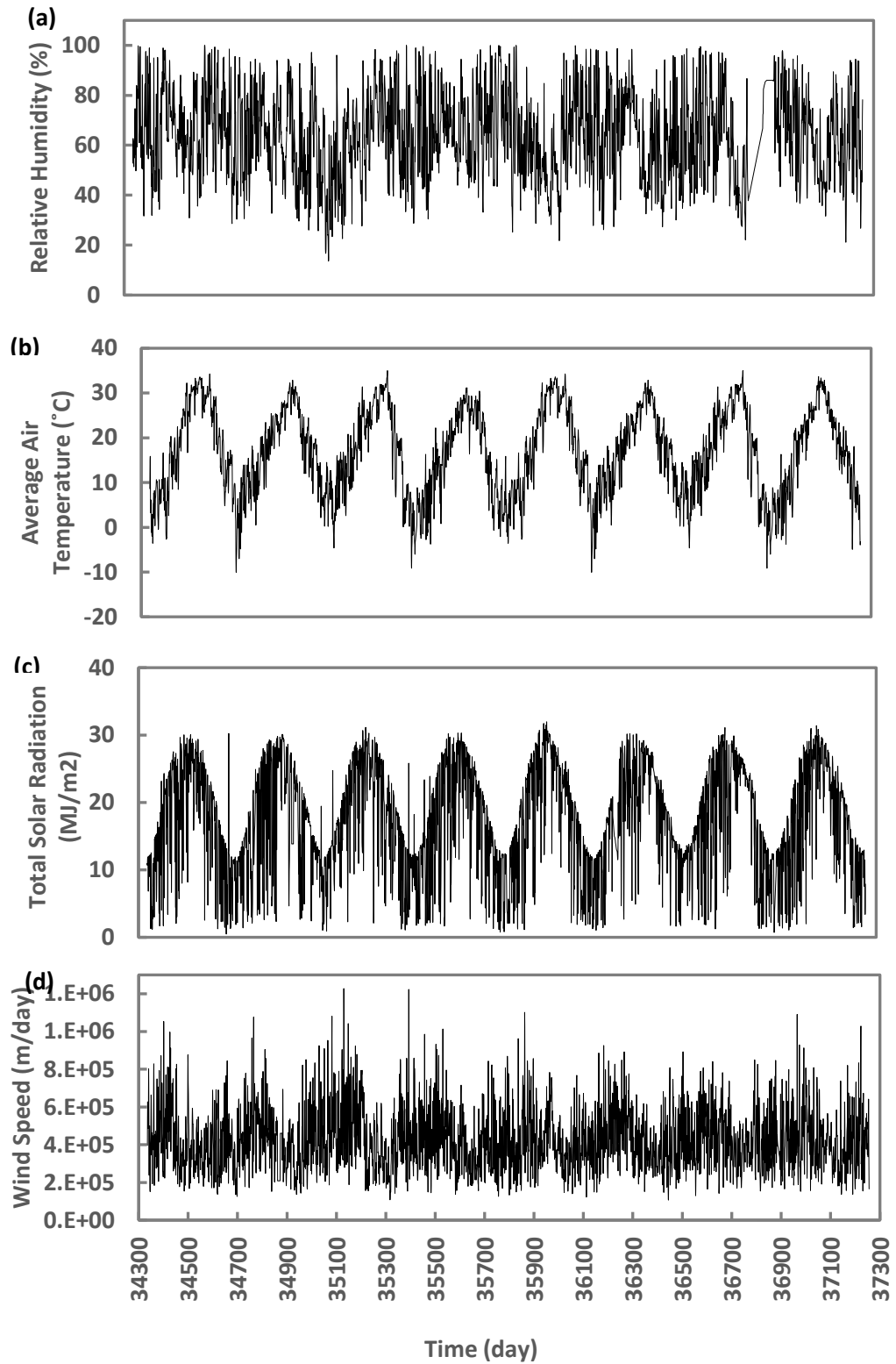


Figure 4.8. Daily Evaporation data from 1994 to 2001, (a) relative humidity, (b) average air temperature, (c) total solar radiation, (d) wind speed (from Oklahoma Mesonet Station Medicine Park)

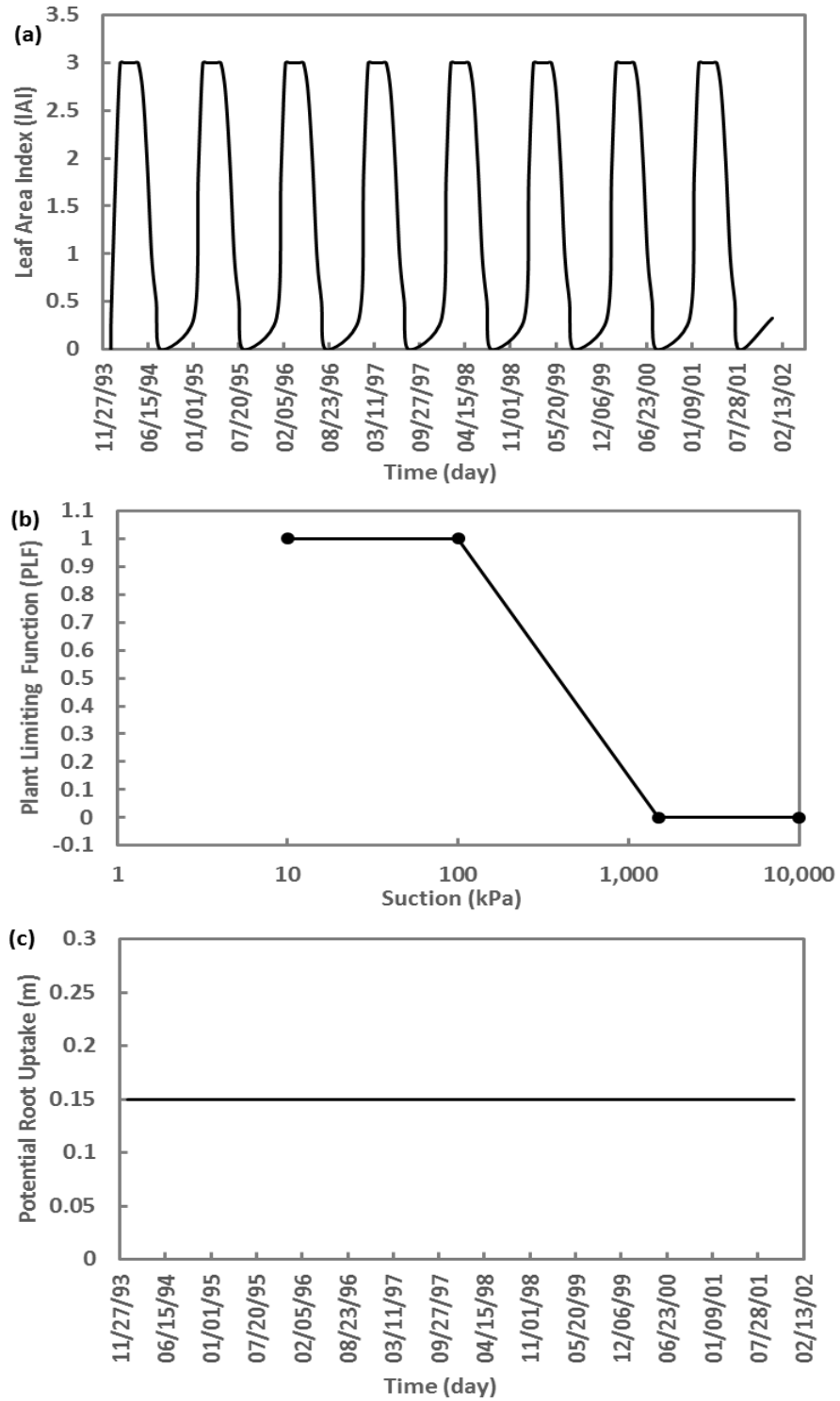


Figure 4.9. Daily Transpiration data from 1994 to 2001, (a) leaf area index, (b) plant limiting function, (c) potential root uptake

While it is possible to utilize the Penman method for historical climate data obtained from weather stations, the projected future climate data is limited to temperature and rainfall and does not include relative humidity, solar radiation, and wind speed. Thus, only the Thornthwaite method can be applied for future years. To overcome this limitation, finding logical ways to use historical data sets to develop a calibration procedure between the Penman and Thornthwaite methods is a primary purpose of this research.

4.4 Results and calibration of soil moisture prediction models

The potential evapotranspiration obtained from Thornthwaite equation is calibrated against the results derived from Penman equation. To calibrate the equations, the slope of the regression between potential evapotranspiration derived from two methods was forced to pass through the origin for each month for the calibration period. This calibration procedure was discussed by Moeletsi et al. (2013). The calibration coefficient was then obtained by calculating the product of the slope of the regression lines (forced to pass at 0, 0) and the original coefficient.

$$C_T = Slope \times 1.6 \quad (4-7)$$

Where, C_T is a new constant for the Thornthwaite equation, which is substituted for the constant number or 1.6 used in the equation. A monthly potential evapotranspiration estimated from two methods before calibration is shown in Figure 4.10 using the historical dataset from 1994 to 2001.

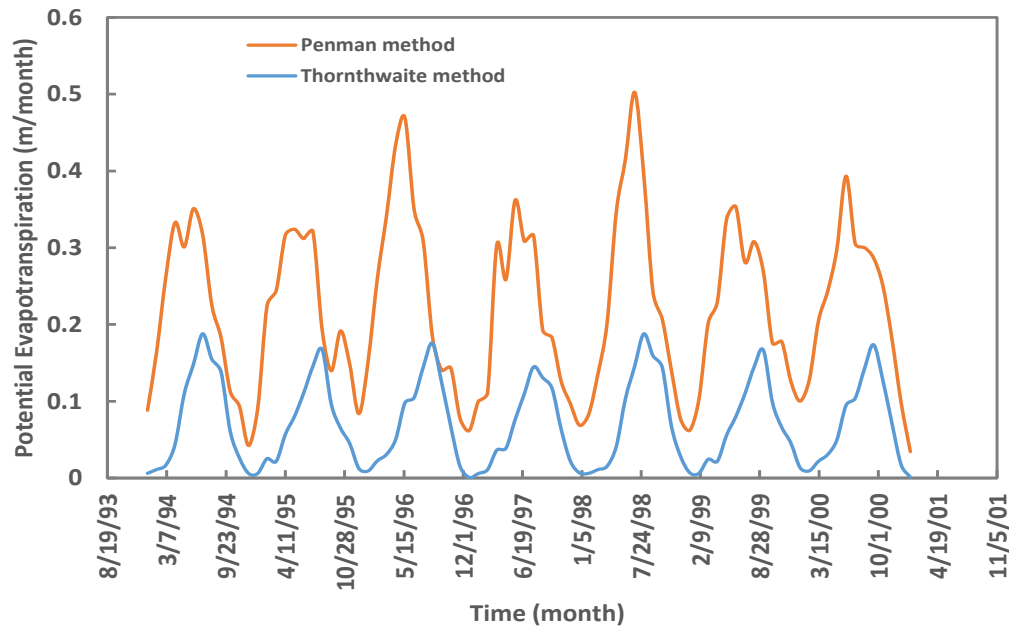


Figure 4.10. Thornthwaite potential evapotranspiration and Penman potential evapotranspiration from 1994-2001

The Thornthwaite potential evapotranspiration (TPET) calibrated with the slopes calculated from each month as shown in Figures 4.11 and 4.12 indicates a good agreement with Penman potential evapotranspiration (PPET) as shown in Figure 4.13.

The actual evapotranspiration, which is a modified potential evapotranspiration, is required to contribute to the net infiltration as a soil-atmosphere boundary condition. Wilson-penman (1994) equation was used for modifying Penman potential evapotranspiration. A method using transpiration (vegetation) parameters was proposed by the author of this research to calibrate the Thornthwaite actual evapotranspiration (TAET) with the Penman actual evapotranspiration (PAET). Three different Leaf Area Index (LAI) curves were designated as variables to obtain the actual evapotranspiration from the Thornthwaite potential evapotranspiration as shown in Figure 4.14. Three calibrated curves of the TAET resulted from three different LAI

alternatives are shown in Figure 4.15 and compared with the PAET. According to Figure 4.16, the results of pore water pressure changes around the pile head using the proposed method indicates that the Leaf Area Index can be a reasonable variable to calibrate the Thornthwaite actual evapotranspiration with the Penman actual evapotranspiration.

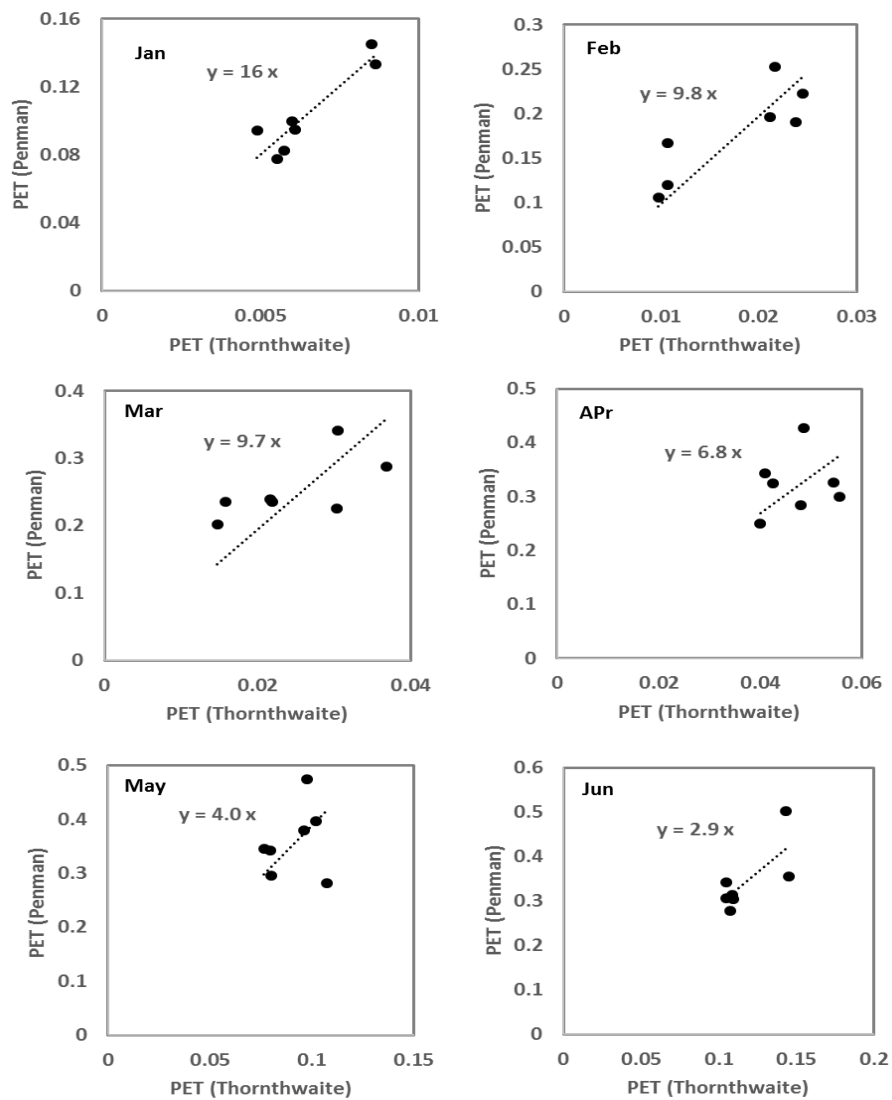


Figure 4.11. Calibration factor for monthly Thornthwaite potential evapotranspiration (m/month) from (a) January to (f) June

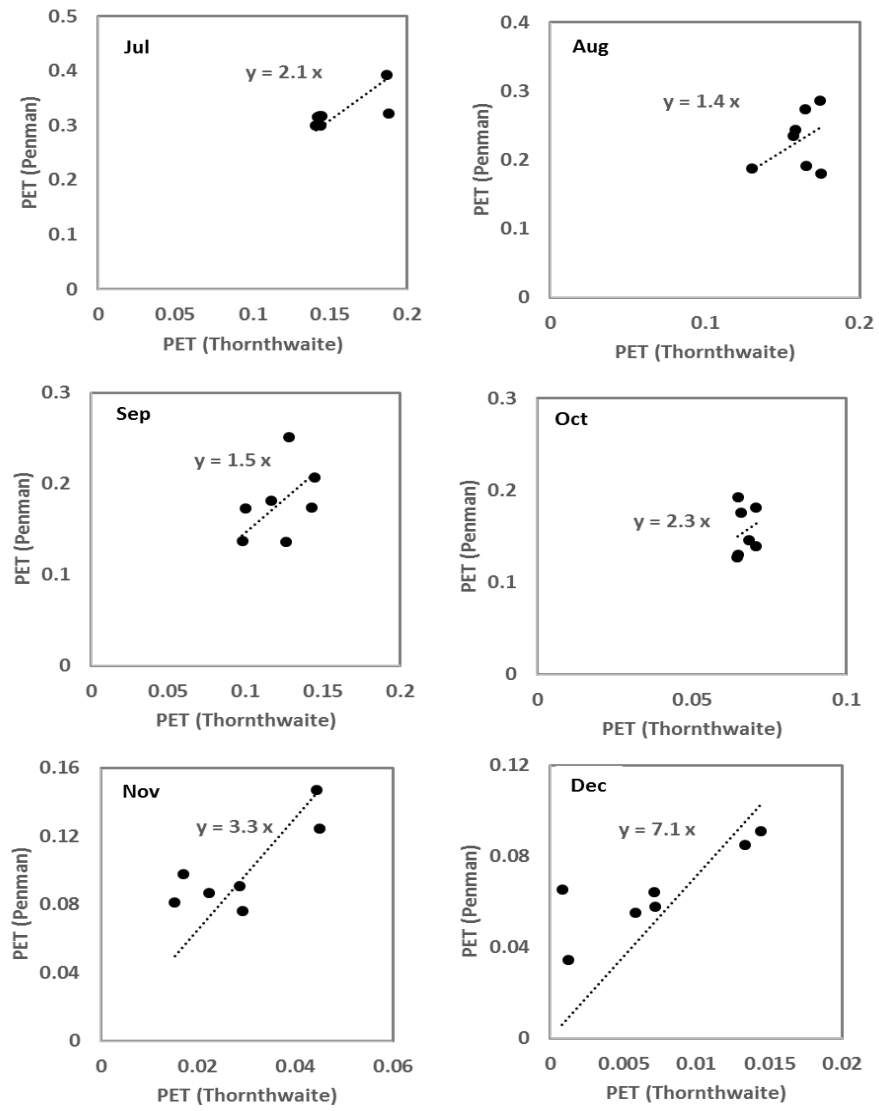


Figure 4.12. Calibration factor for monthly Thornthwaite potential evapotranspiration (m/month) from (g) July to (l) December

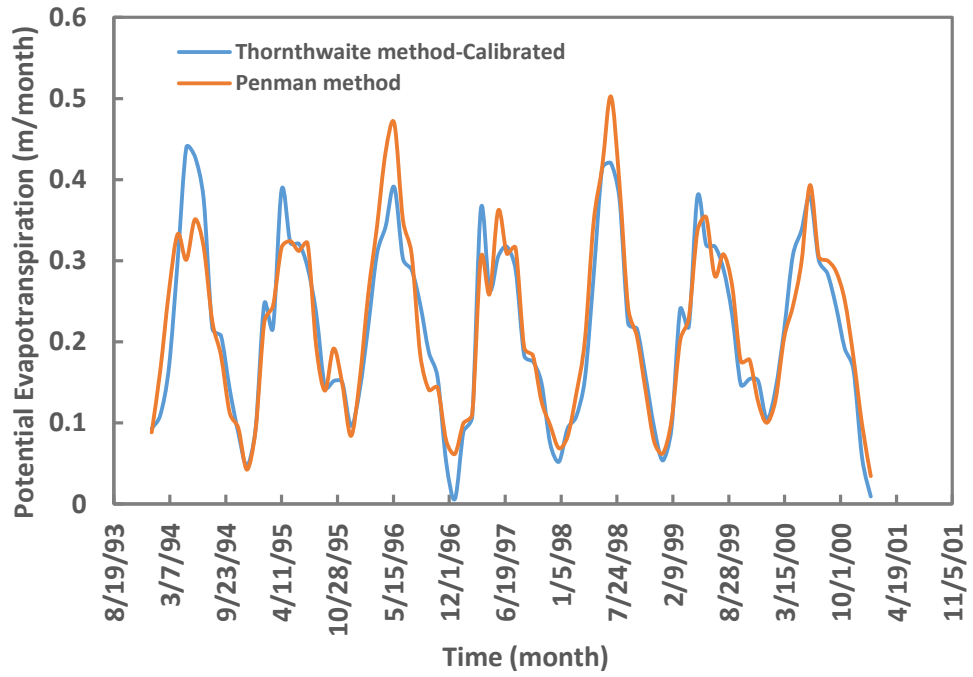


Figure 4.13. Calibrated Thornthwaite potential evapotranspiration and Penman potential evapotranspiration from 1994-2001

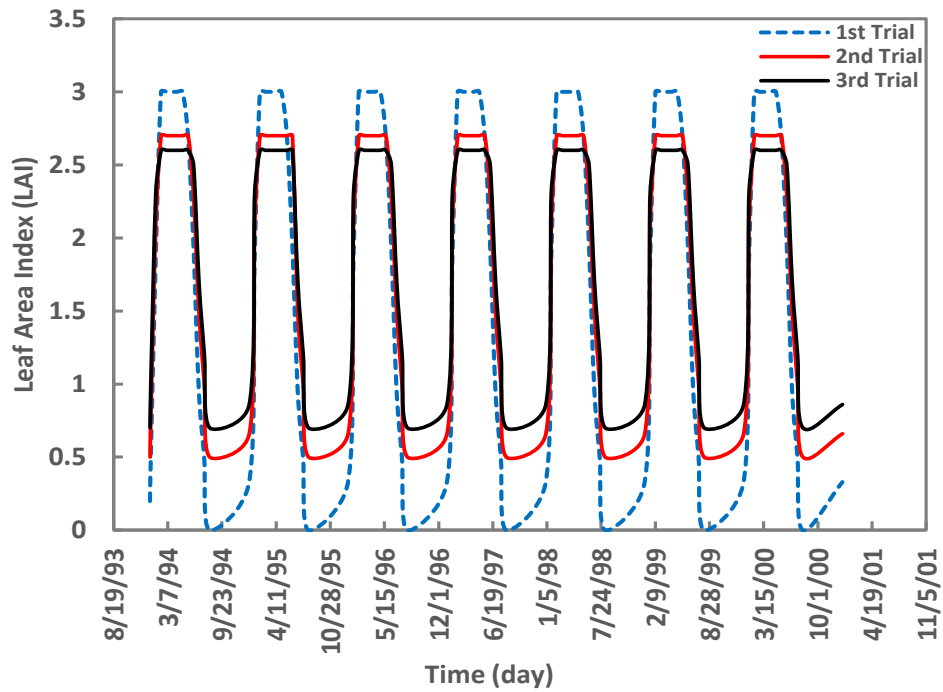


Figure 4.14. Leaf Area Index at different trials

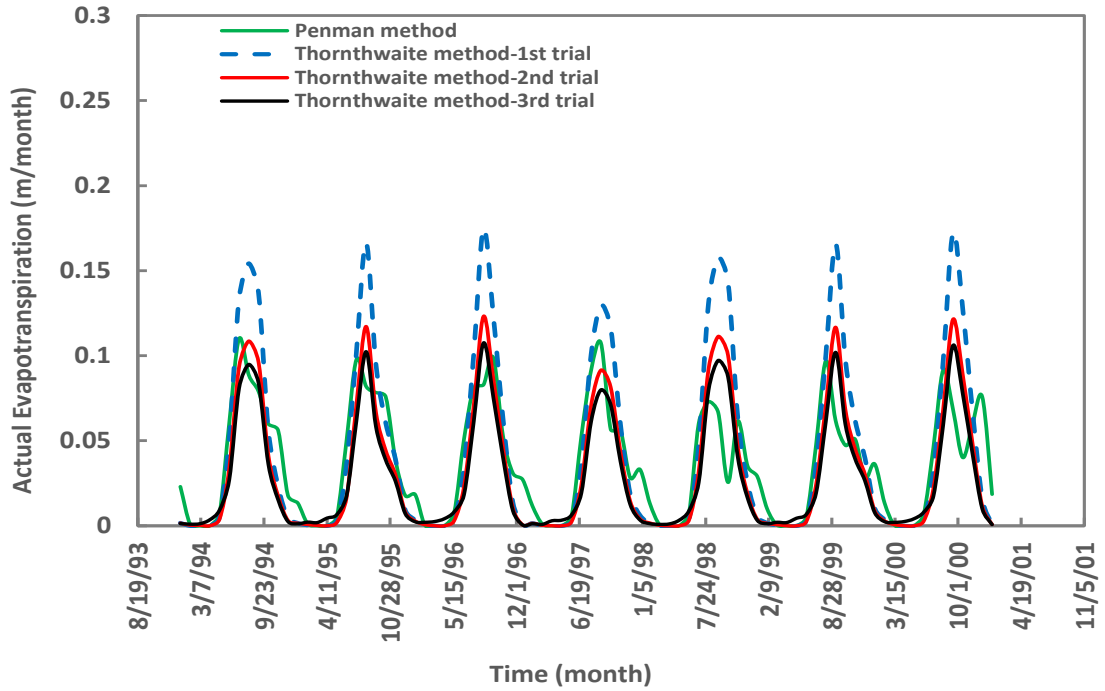


Figure 4.15. Calibrated Thornthwaite actual evapotranspiration and Penman actual evapotranspiration from 1994-2001

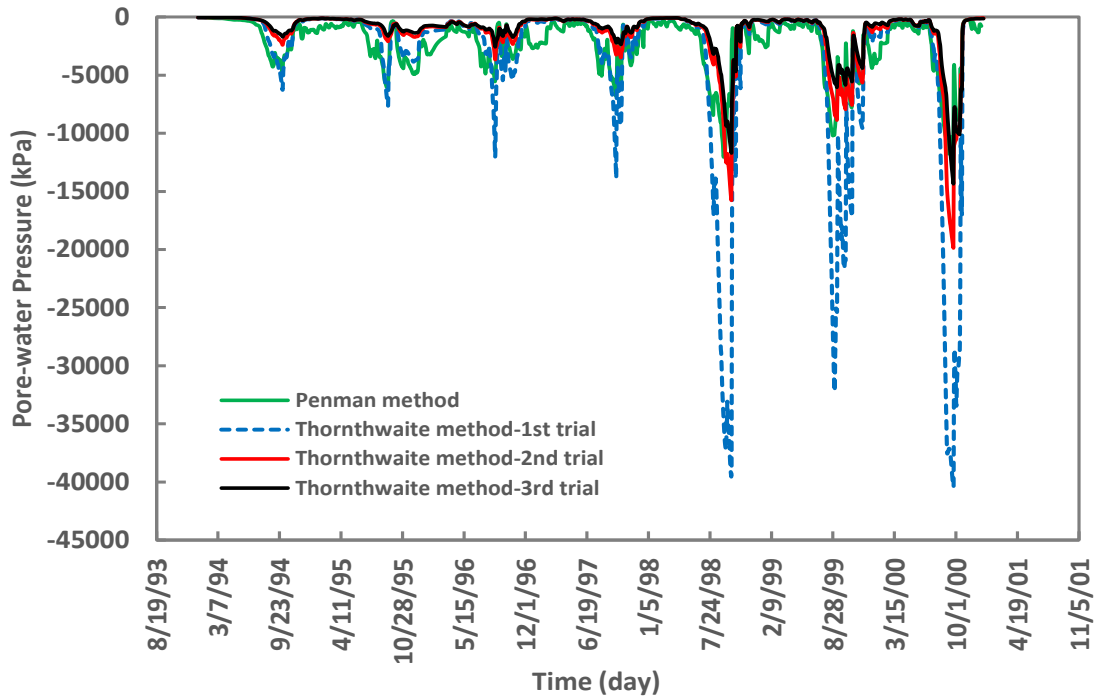


Figure 4.16. Pore water pressure change around soil surrounding pile head from 1994-2001

The pore water pressure variations shown in Figure 4.16 for the calibration period indicate that the calibrated method using the leaf area index is a reasonable method for adjustment of Thornthwaite method to match Penman method. Therefore, a pattern of leaf area index for 150 years from 1950 to 2099 analogous to the 3rd trial of calibration method was used to predict the pore water pressure changes at the top of the pile from past to future. It can be seen in Figure 4.17(a) that the negative pore water pressure (suction) increased with time and the calibrated suction were less than the original amounts of suction predicted with Thornthwaite method. In addition, it can be seen in Figure 4.17(b) that the maximum changes of the calibrated suction and the original one on the ground surface were 1,000 kPa and 35,000 kPa, respectively. These predictions based on the projected climate data shown in Figures 4.3 and 4.4 are consistent with the projected increases in temperature project during the 21st century under essentially constant project rainfall amounts for the same period as shown in Figures 4.3 and 4.4. While there is a great deal of uncertainty in climate projections, the preceding method provides a rational basis for examining the variations in soil moisture content, positive and negative pore water pressures, and hence soil stiffness resulting from different climate change scenarios. This allows for an analysis of changes in lateral loading behavior of the bridge abutment system due to projected variations in moisture conditions, as described in the next section.

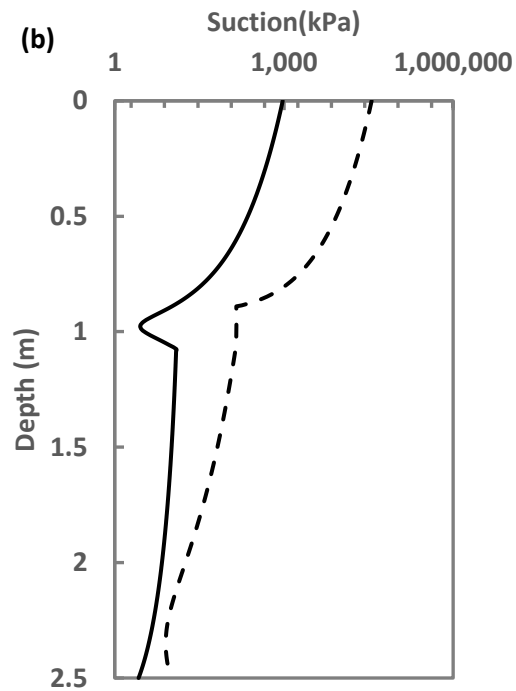
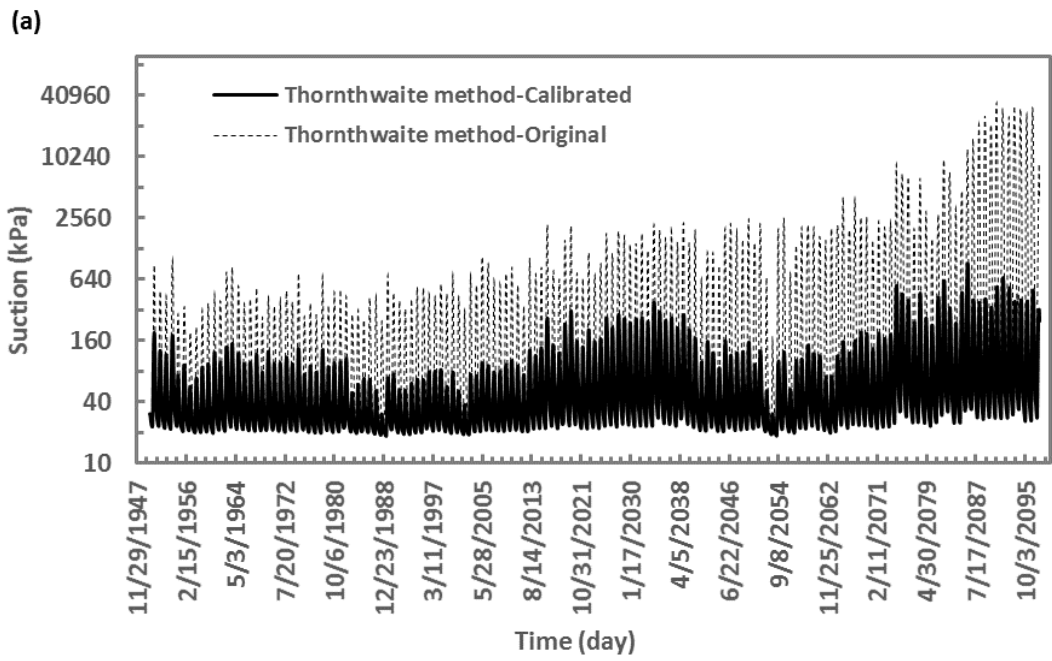


Figure 4.17. (a) Suction predictions from 1950 until 2099 around soil surrounding pile head
(b) Maximum suction profile in clayey soil layer

4.5 Numerical modeling of pile-soil interaction considering the soil moisture changes

4.5.1 Finite difference method

LPILE was utilized to investigate the pile-soil interaction in for abutment piles in soil under unsaturated conditions. Since LPILE was not designed for the unsaturated soil condition directly, the concept of apparent cohesion proposed by Fredlund and Rahardjo (1993) was used in LPILE model. Varying stiffness in soil around an abutment pile may result from changes in moisture content in the soil. To investigate the abutment pile behavior caused by soil moisture changes, the predicted suction corresponding to different moisture contents obtained from the unsaturated seepage analysis was used to determine the apparent cohesion used to define p-y curves in LPILE. Clayey soils are more vulnerable to the moisture change related property changes than sandy soils, so the second layer (clayey soil) of the south part of I-44 bridge was subjected to different suctions. The p-y curves were developed in LPILE using the equations proposed by Evans and Duncan (1982) and Mokwa et al. (2000) as shown in Figures 4.18 and 4.19. Both p-y curves exhibited a similar linear trend at very low displacements. Softening and hardening behaviors were captured using the former and the latter equations. These behaviors were more pronounced while applying high suction in the relevant equations (e.g. $u_a - u_w = 1000$ kPa). A simple linear extended Mohr-Coulomb failure model was used with these methods, and soil properties for the unsaturated clay were assumed based on experimental tests. For the purpose of developing p-y curves for the c- ϕ soil using the LPILE program, the effect of suction was incorporated into the cohesion intercept using the following equation:

$$c=c'+(u_a-u_w)\tan\phi^b \quad (4.8)$$

where: c' is the effective cohesion intercept, (u_a-u_w) is suction, and ϕ^b is the friction angle with respect to suction. The geotechnical properties of the soil layers obtained from SPT and CPT correlations and laboratory testing and compatible with typical soil properties available in LPILE are listed in Table 4.1 (Reese et al. 1974, 1976; Detournay and Cheng 1993).

Table 4.1. Properties of typical soli layers

Soil layer	Soil Thickness(m)	Total unit weight (kN/m ³)	Soil lateral Stiffness, k, (kN/m ³)	Effective Cohesion Intercept (kN/m ²)	Internal friction angle (°)	Friction angle with respect to suction (°)
Loose sand backfill-First layer	2.00	15.63	6790	-	30	-
Stiff lean clay-Second layer	2.00	21.5	136,000	0	-	10
Dense silty sand-Third layer	0.6	20.72	61,000	-	35	-
Weak laminated sandstone interbedded with shale seams	6.00	24.35	-	-	-	-

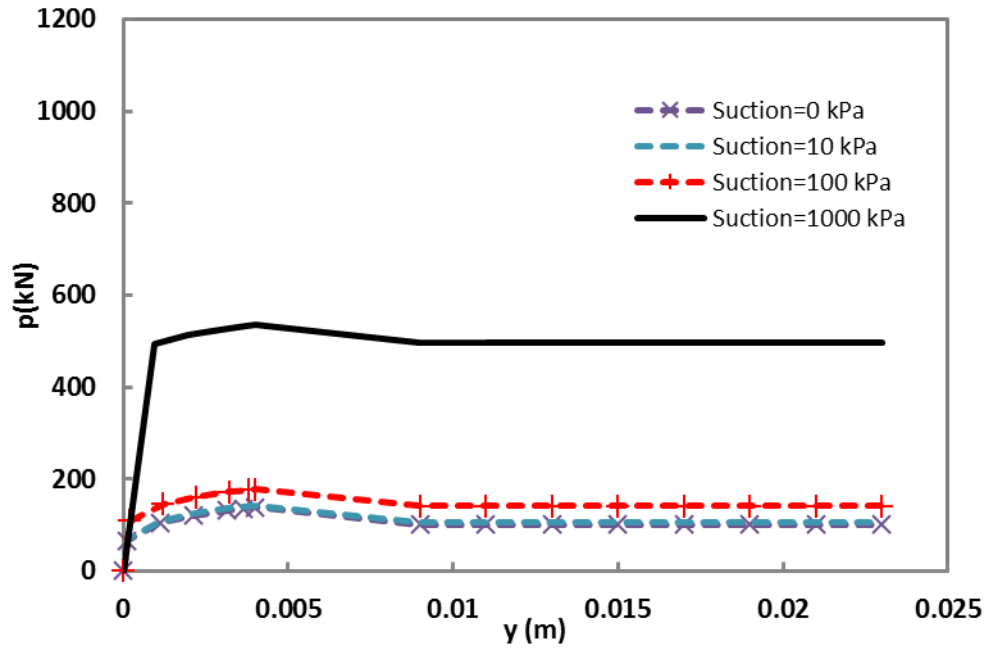


Figure 4.18. P-y curves obtained from Evans and Duncan (1982) equation

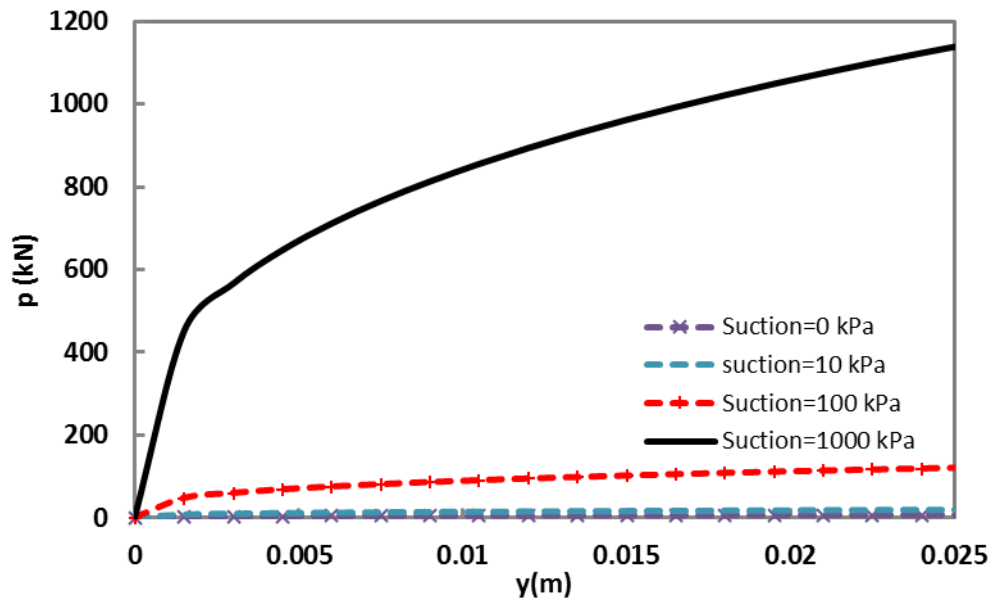


Figure 4.19. P-y curves obtained from Mokwa et al. (2000) equation

4.5.2 Comparison of pile response using Evans and Duncan (1982) and Mokwa et al. (2000) p-y curve methods

According to a study conducted by Kirupakaran (2013), the I-44 bridge deck was subjected to an average temperature variation of 95°F over a six-month period. Assuming the thermal deformation of the bridge was symmetric to the center of the bridge, the thermally induced deformation of the superstructure at the abutment due to the change in temperature of superstructure can be calculated by Equation 4.9.

$$\delta = \alpha \times \Delta T \times L / 2 \quad (4.9)$$

where, α is the coefficient of thermal expansion, ΔT is the change in temperature and L is the total length of the bridge. Thermal expansion coefficient of the reinforced concrete superstructure was considered as $6.23 \times 10^{-6} / ^\circ \text{F}$. Therefore, thermally induced deformation of the superstructure based on Equation 6.8 at the abutment was considered as 0.019 m. The average movement of the superstructure based on crack meter readings was 0.022 m. Since the calculated superstructure movement was in the range of the measured reading from crack meter, thermally induced deformation at the abutment was assumed to be 0.022 m. The displacement of the abutment was directly applied as the boundary condition at the top of abutment in LPILE modeling. The connection between the top of the abutment and the bridge deck was assumed to be fixed. The boundary condition of having a displacement without any rotation at the top of the abutment was compatible with the performance of IABs both in practice and theory. The axial load on the pile due to the superstructure was considered as 136.6 kN.

The results of the LPILE analysis revealed that bending moments obtained using the Evans and Duncan (1982) model were less than those obtained using the Mokwa et al. (2000) model. This difference was more noticeable when the amount of suction was higher (e.g. 1000 kPa). Mokwa et al. (2000) proposed a displacement-resistance curve for soil under high suction, which resulted in a soil layer with high stiffness. The response of a pile in a soil with high stiffness results in higher bending moments as shown in Figures 4.20 and 4.21. The lateral deflections at the pile head showed that a soil layer with higher suction and stiffness provides greater resistance against to lateral displacement at the top of the pile, which resulted more abrupt curvature and greater bending moment. According to Figures 4.22 and 4.23, the bending moments obtained from the Mokwa et al. (2000) p-y curve equation were less than those calculated by the Evans and Duncan (1982) equation at lower suctions.

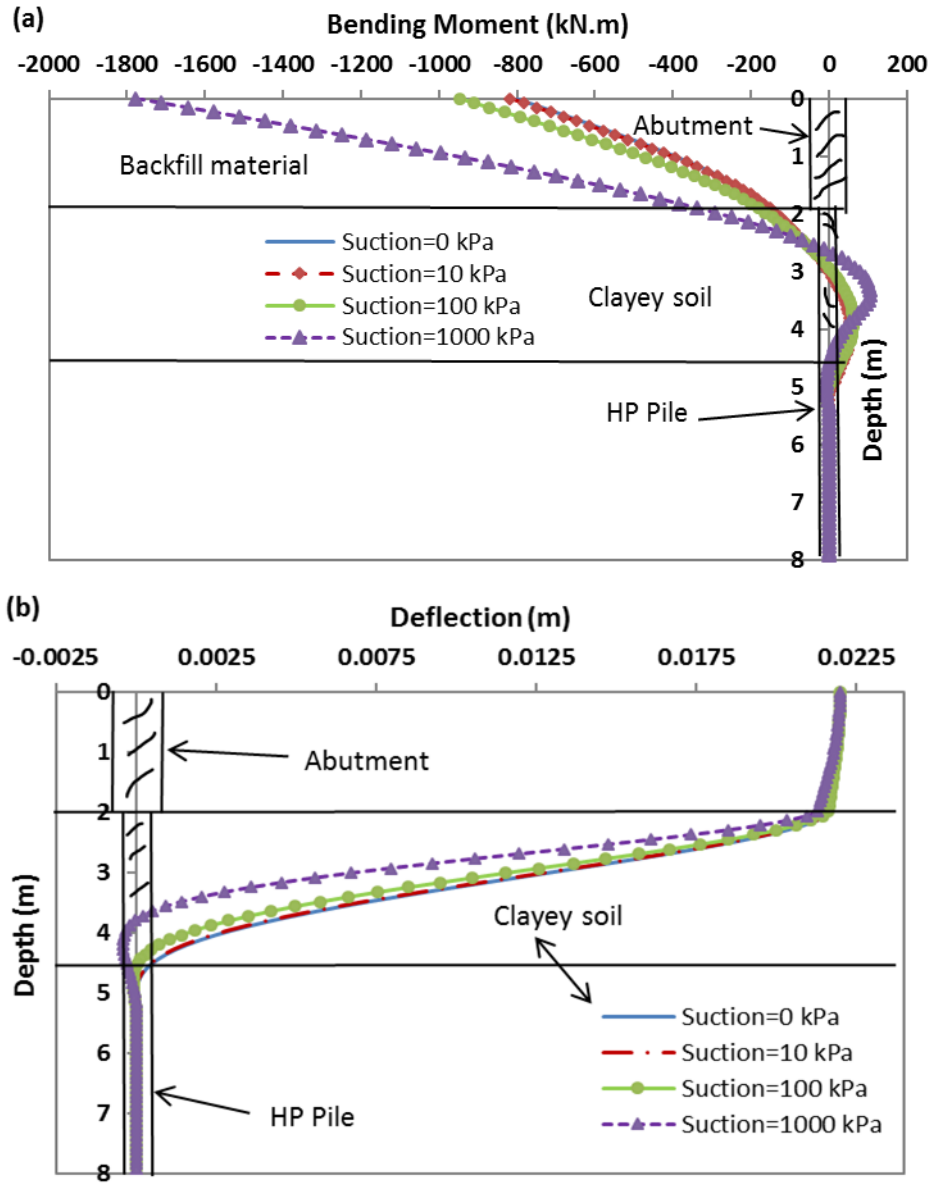


Figure 4.20. (a) Bending moment changes and (b) lateral deflection in the given abutment and pile using p-y curves from Evans and Duncan (1982)

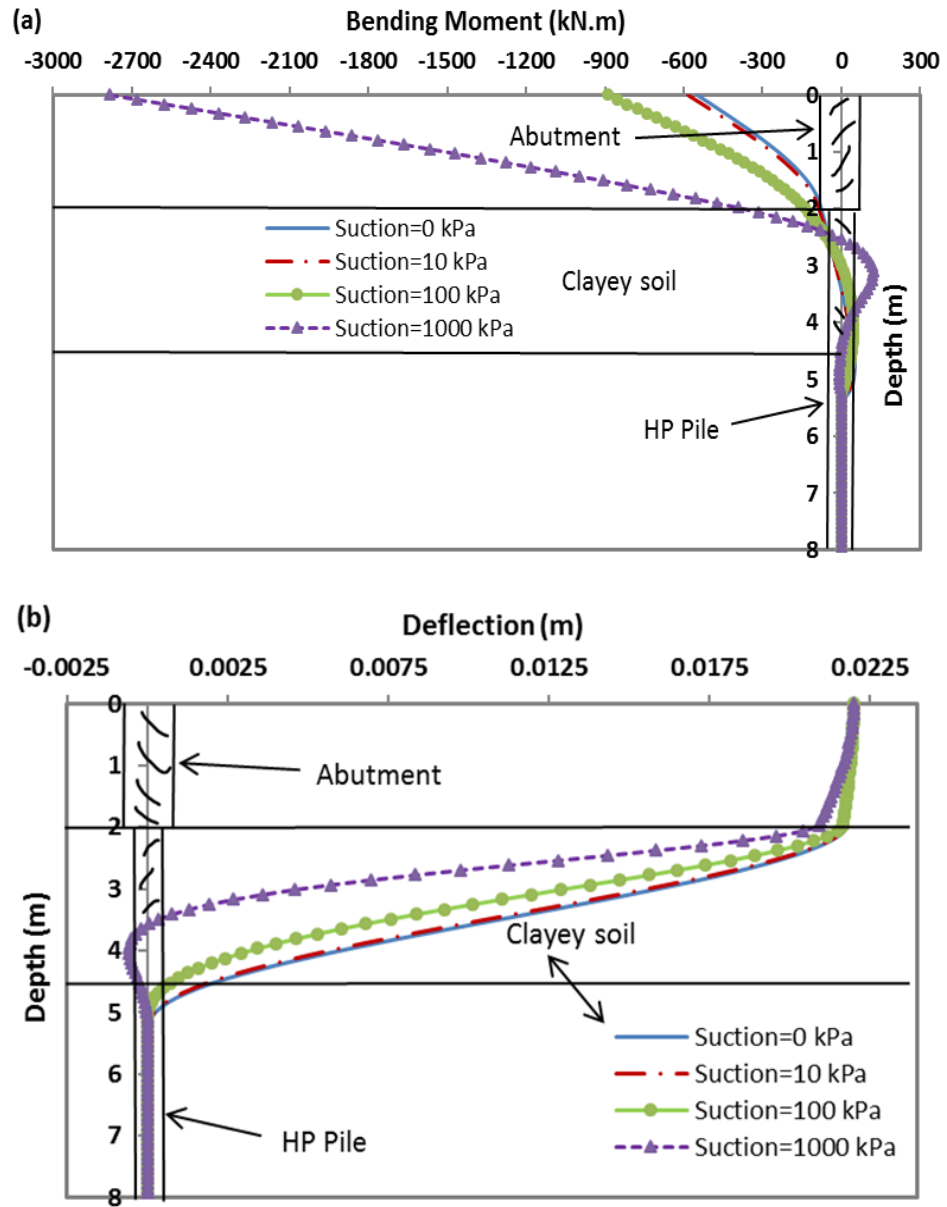


Figure 4.21. (a) Bending moment changes and (b) lateral deflection in the given abutment and pile using p-y curves from Mokwa et al. (2000)

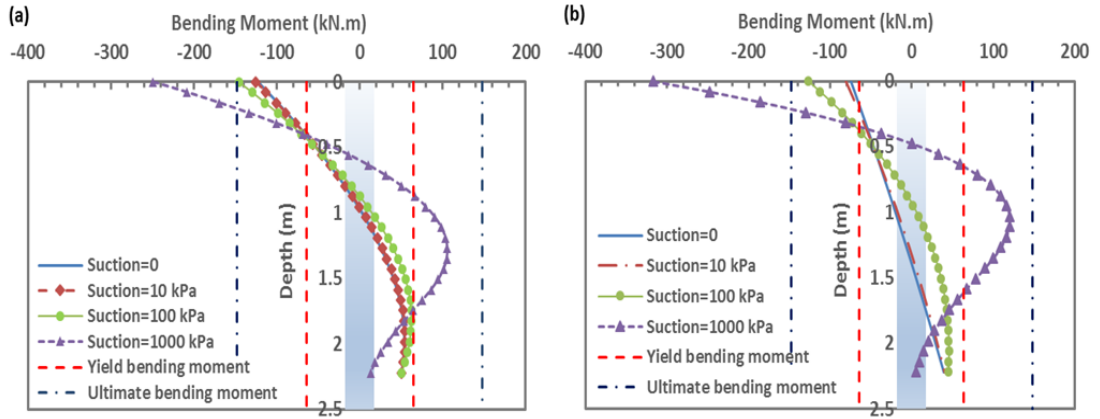


Figure 4.22. Bending moment variations in the given pile using (a) Evans and Duncan (1982) equation (b) Mokwa et al. (2000) equation

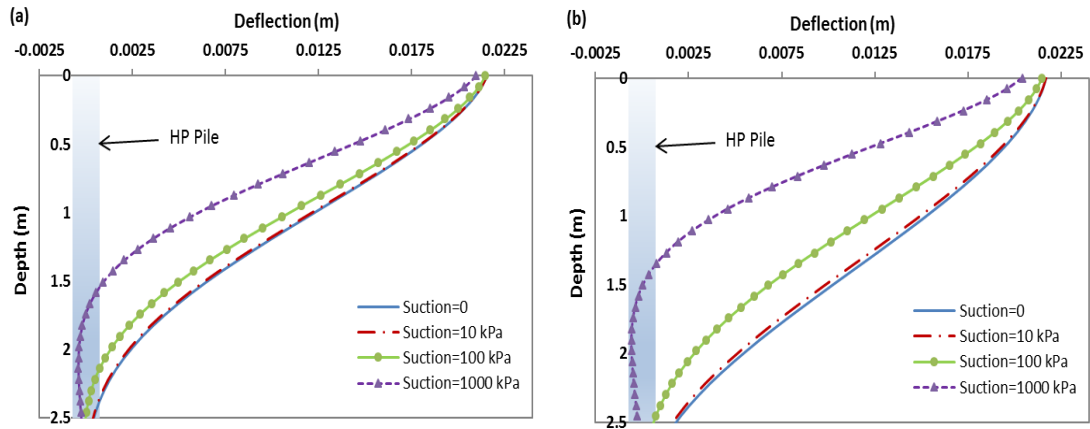


Figure 4.23. Lateral deflection variations in the given pile using (a) Evans and Duncan (1982) equation (b) Mokwa et al. (2000) equation

4.6 Parametric study of pile-soil interaction in IAB

L-Pile was used to perform a parametric study to extend the results of the Oklahoma IAB to general IABs. The parameters effective in the analysis include; pile types (different HP sections), pile orientation (weak axis vs. strong axis bending); different embankment soil and foundation soil; various abutment backfill materials such as Expandable Polystyrene (EPS) blocks, Controlled Low Strength Material (CLSM) and compacted and non-compacted granular fill; and combination of EPS and granular backfill that can

prevent ratcheting effects in backfill mentioned earlier. CLSM is being used as abutment backfill in many of the ODOTs newer non-integral bridges, but the use of this stiff material is prohibited in IABs by other states such as Pennsylvania. While CLSM is beneficial in reducing settlement of bridge approach slabs, it may restrict the movement of the abutments in IABs. A combination of EPS and CLSM may provide an ideal backfill for IABs.

4.6.1 Abutment pile type and orientation

In this parametric study, the interaction of different piles, which are common in IABs across the country with the soil were investigated for the given temporal temperature and soil moisture changes assuming constant changes in suction for the clayey layer (e.g. 1000 kPa). The sectional properties of the considered piles are as follows:

Table 4.2. Properties of typical abutment piles

Abutment Pile Type	Bending Axis	Elastic Section Modulus, $S_y(m^3)$	Plastic Section Modulus, $Z_y(m^3)$
HP 10x42	Weak	2.33×10^{-4}	3.57×10^{-4}
	Strong	7.11×10^{-4}	7.92×10^{-4}
HP 12x53	Weak	3.46×10^{-4}	5.28×10^{-4}
	Strong	10.93×10^{-4}	12.13×10^{-4}
HP 14x89	Weak	7.26×10^{-4}	11.09×10^{-4}
	Strong	21.47×10^{-4}	23.93×10^{-4}

*Yield strength of steel, $f_y=0.276 \text{ GPa}$ **Ultimate strength of steel, $f=0.414 \text{ GPa}$

HP 14x89 pile oriented in strong axis bending caused larger bending moments in the abutment piles than the other pile configurations considered in the modeling. The computed bending moment for HP 14x89 pile oriented in weak axis bending were larger than the bending moments for HP 10x42 pile oriented in both axes and HP 12x53 pile oriented in weak axis bending as shown in Figure 4.24 (a) and (b).

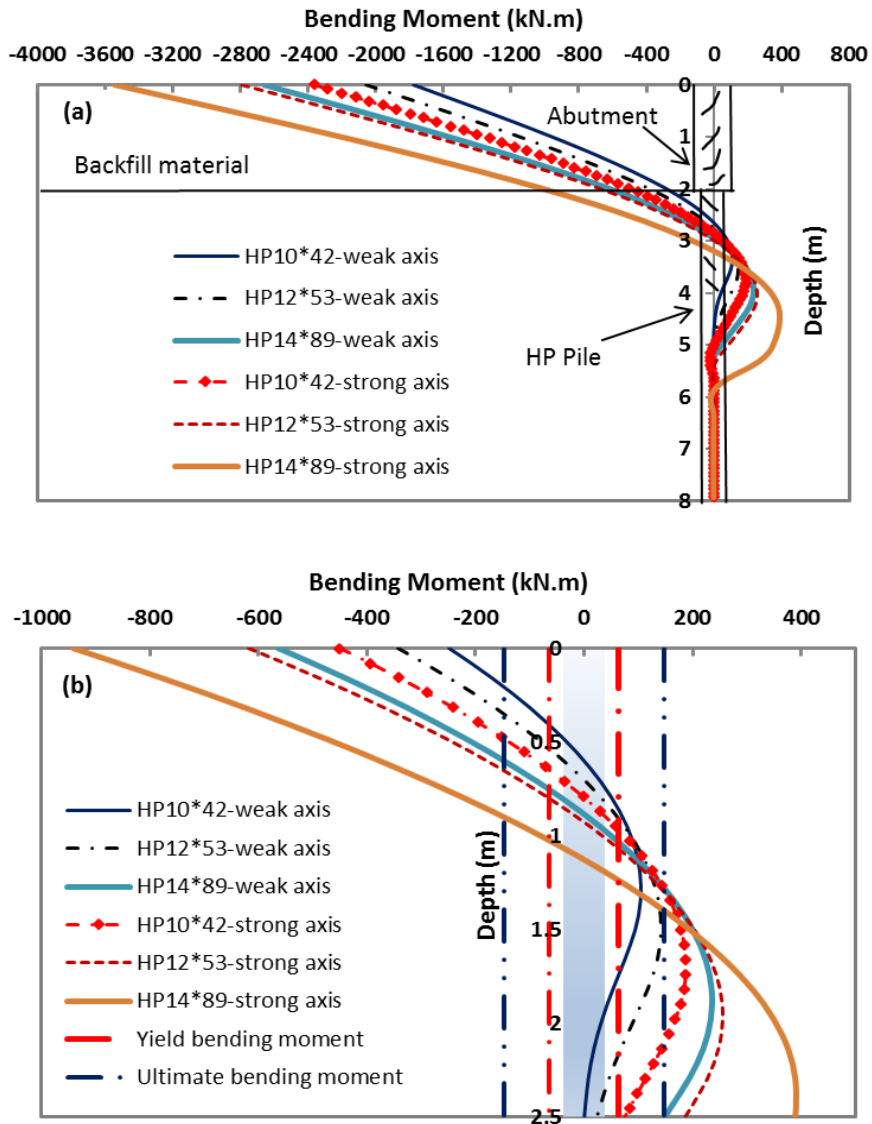


Figure 4.24. Bending moment variations for different pile configurations (a) in abutment pile (b) in pile surrounded by clay soil

The orientation of HP piles with reference to the bridge longitudinal axis affected the thermally induced deformation in the abutment piles since the stiffness of the HP piles varies according to the bending axis. The orientation of weak axis bending helped to reduce the bending moment that occurs in the abutment piles.

4.6.2 Type of soil surrounding the abutment piles

Varying stiffness in soil around a pile may result from changes in moisture content in the soil. To investigate the abutment pile behavior caused by soil moisture changes, the soil suction was estimated for different degrees of saturation. Clayey soils are more vulnerable to the moisture change than the sandy soils, so the second layer of the south abutment profile of I-44 bridge with different stiffness was considered in the parametric study. The different stiffness was defined using different friction angle with respect to constant suction (e.g. 1000 kPa).

The bending moments generated at the abutment were more than those in the pile when the stiffness of soil surrounding the pile increased. According to Figure 4.25 (a) and (b), soil with high friction angle with respect to suction, which is representative of a high clay-content layer, created the largest bending moment in the pile and abutment. Pre-drilled holes can be used as an alternative to improve the behavior of the abutment piles when a soil layer susceptible to pore water changes (e.g. clay soil) exist around the piles at shallow depth.

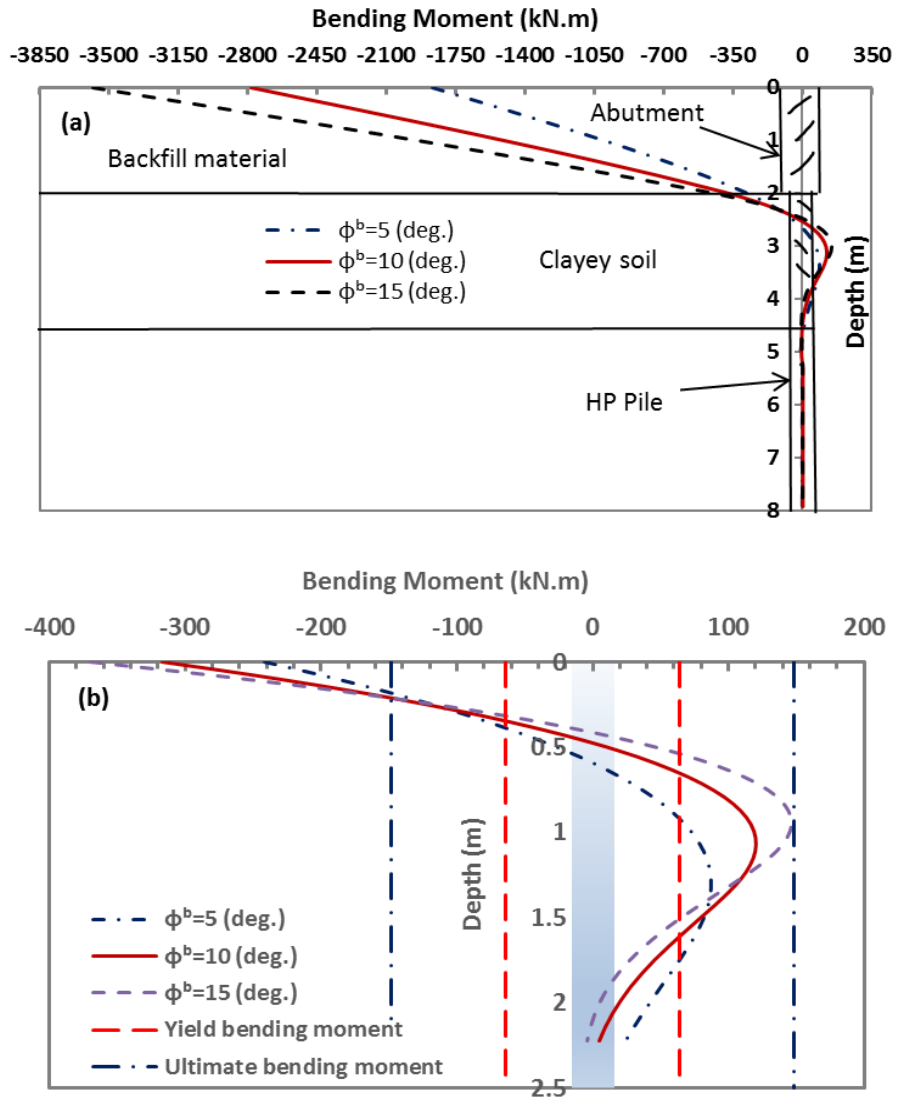


Figure 4.25. Variation in bending moments (a) in pile and abutment (b) in pile for different types of soil stiffness

4.6.3 Type of backfill material

To investigate the effect of backfill stiffness on the abutment pile behavior, extremely dense and loose sands were selected to see the behavior of the pile in comparison with the original backfill soil while the suction was constant in the clayey layer (e.g. 1000 kPa). According to Figure 4.26 (a) and (b), dense sand as a backfill material surrounding the

abutment created the largest bending moments in the abutment. The effect of backfill material on the pile below the abutment was negligible.

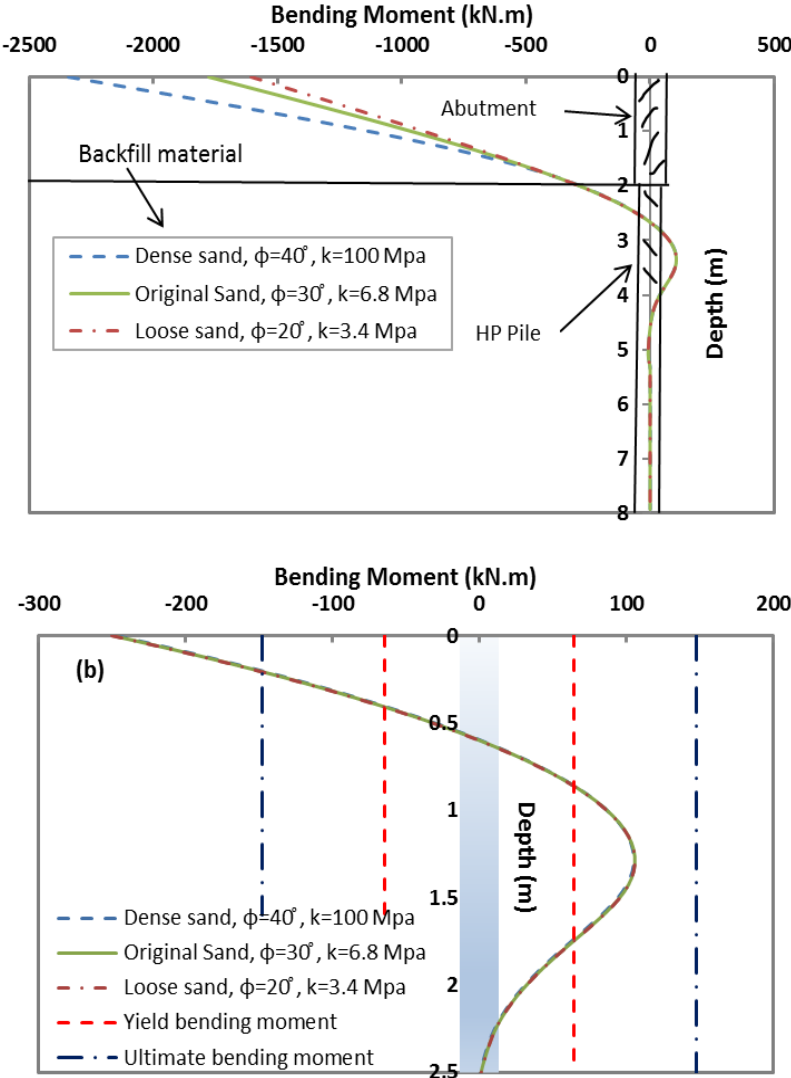


Figure 4.26. Variation in bending moments for different types of backfill materials (a) in abutment and pile (b) in pile surrounded by clayey soil

CHAPTER 5: Conclusions and recommendations

5.1 Summary: Impact of desiccation cracks on unsaturated soils

An extensive field and laboratory investigation and a mechanical and a hydraulic modeling of a slope was conducted to understand the effect of desiccation cracks on the slope stability. The research involved installing weather monitoring stations and soil moisture sensors at a test site where shallow slope failures had occurred. Laboratory testing was conducted to determine soil shear strength, soil water characteristic curves, and moisture flow properties. A new apparatus for measuring the tensile strength of desiccating soil was used to obtain the tensile strength of test soil. A laboratory box was designed to monitor the suction changes and desiccation crack depth for a period of time while drying. A simple analytical model was developed for predicting desiccation crack depth and compared with results of a numerical model using a finite element program and experimental observations.

The effect of spacing and width of desiccation cracks on the hydraulic conductivity of a cracked layer was investigated and compared with an enhanced or equivalent hydraulic conductivity model for a cracked layer using numerical modeling. In addition, numerical modeling was conducted using SVFLUX to predict moisture content changes in soil profiles using measured weather data as input for comparison to measured moisture contents during the monitoring period.

Limit equilibrium slope stability analyses were conducted using the program SVSLOPE. The slope stability analysis involved first predicting pore water pressures using an unsaturated seepage program, SVFLUX, with weather data used for input. Three

unsaturated seepage analyses were conducted for the slope. In the first case, the hydraulic conductivity was assumed to be uniform throughout the slope while in the second and third cases, an upper layer of soil with a set of cracks and enhanced hydraulic conductivity was assumed, respectively. The thickness of this layer was assumed to correspond to roughly the bottom of the slope failure surface and consistent with the depth of desiccation cracking obtained from the analytical and numerical analyses. Stability analyses were then performed using the predicted pore pressure distributions. Following are some of the important conclusions and recommendations from this study.

5.2 Conclusions: Impact of desiccation cracks on unsaturated soils

1. A simple analytical model, based on linear elastic theory, for predicting depth of desiccation cracks in compacted clayey soil was developed. The model was used to predict the change in suction required to produce cracking as a function of depth. Predicted changes in suction necessary to produce cracking at a particular depth were compared to maximum changes in suction measured from moisture sensors in the laboratory desiccation box test. The cracking depth is assumed to be the depth where the trend of predicted cracking suction changes and the trend of measured suction changes meet. The tensile strength of soil was also used to calculate the cracking depth through the tensile stress distribution over depth predicting using the finite element model. The cracking depths obtained from the analytical and numerical analyses were in a good agreement with the laboratory observations of cracking depth.

2. The depth of desiccation cracks predicted for the Chickasha slope using the simplified models (analytical and numerical models) and accounting for some uncertainty in the model parameters was in the range of 1.9 to 2.1 m with the best estimate around 2.0 m from the analytical model and 1.75 m from the numerical model (Appendix A). These estimations were consistent with observations of moisture changes with depth and the estimated depth of the failure surface at the site.
3. Tensile strength determined in the desiccation box was observed to generally increase with increasing initial water content. However, the study conducted by Varsei et al. (2016) showed that the tensile strength only increased up to a point where the water content was well beyond optimum and then it decreased with increasing water content.
4. Two methods including an equivalent permeability and discrete cracks models were used to consider the effect of desiccation cracks in seepage analyses of a slope. The efficiency of these methods was investigated using a simple seepage model considering a set of single cracks with given ratios of crack spacing to crack depth and corresponding equivalent permeabilities. The discrete cracks and equivalent permeability methods in the simple model showed that the interface between the cracked and intact layers considering time became saturated relatively quickly when the permeability of cracked layer compared to intact layer was relatively high.

5. Unsaturated strength parameters, ϕ' , ϕ^b , and c' determined with saturated/unsaturated direct shear testing of composite samples of compacted soil were 29.7°, 11.1°, and 7.6 kPa for the Chickasha slope.
6. Results of flexible wall hydraulic conductivity tests on two thin walled tube samples and one compacted sample from each site provided a range of saturated hydraulic conductivity of 2.82×10^{-6} cm/sec to 6.2×10^{-7} cm/sec for the Chickasha slope. Average value was assumed to represent the intact saturated hydraulic conductivity for use in unsaturated seepage analyses. Unsaturated hydraulic conductivity functions were determined using soil water characteristic curves and saturated hydraulic conductivities. Hydraulic conductivities determined in this manner seemed to provide reasonable results from unsaturated seepage analyses.
7. Trends of soil moisture variations observed with moisture sensors at the test site were predicted reasonably well using the software SVFLUX. However, predictions generally did not capture well the abrupt changes in moisture content recorded by the sensors for the intact slope. These abrupt changes occur mainly at the shallowest sensor location and may be partly the result of desiccation cracking that allows more rapid wetting and drying at the sensor location. Two proposed methods, especially the discrete cracks method for the modeling of desiccation cracks captured these abrupt changes of moisture contents at the upper layers of the slope when the ratio of crack spacing to crack depth was one.

8. Unsaturated seepage analyses using SVFLUX were performed using weather data as input to estimate worst case pore water pressure profiles in the slope. The pore pressure profiles were incorporated into a limit equilibrium slope stability analyses that used a linear unsaturated strength model. Unsaturated strength parameters presented previously were used. The analysis was run with and without considering the effective stress cohesion intercept, c' , for the intact and cracked slope, respectively. The influence of desiccation cracks was modeled by incorporating an upper layer of soil having an enhanced hydraulic conductivity. The upper layer thickness was equal to the calculated desiccation crack depth. Three cases were analyzed: The first case represented a slope with no cracks and the saturated hydraulic conductivity was the average value measured in the laboratory; the second and third cases represented a slope with cracks and the saturated hydraulic conductivity of the upper or cracked layer was obtained from the equivalent permeability and discrete cracks methods. Results of the stability analyses for the slope indicated a significant reduction in factor of safety for shallow slope failure as the hydraulic conductivity of the surface layer increased. Results showed that the factor of safety approached less than one when the permeability of the cracked layer was obtained using the equivalent method and the effective cohesion intercept was zero for the cracked layer. The equivalent permeability for the cracked layer was two orders of magnitude greater than the permeability of the underlying soil.

5.3 Recommendations: Impact of desiccation cracks on unsaturated soils

1. Unsaturated seepage prediction should be conducted using a reliable program and compared with related variations such as moisture contents at an instrumented site. The site should be equipped with proper instruments at a minimum of three different depths.
2. The depth of the upper cracked layer should be estimated using the simplified analysis presented in this study and/or based on field observations. The simplified analysis of predicting crack depth will require an estimate of the suction profile expected in the slope under drying conditions.
3. An upper layer of uniform thickness equal to the predicted depth of desiccation cracks with enhanced hydraulic conductivity at least two orders of magnitude greater than the permeability of intact soil, should be used in the unsaturated seepage model. If possible, the intact hydraulic conductivity should be based on flexible wall permeability tests conducted on thin-walled samples obtained from the slope site.
4. The effect of desiccation cracks on the permeability of the cracked layer and suction changes can be examined using the desiccation box after wetting for a period of time.
5. If possible, 3-D analysis for the seepage and slope stability should be conducted to compare with 2-D analysis conducted in this research. The effect of discrete cracks on the 3-D seepage analysis can be modeled as a network of single cracks with the equal spacing in two directions.

6. The effective stress cohesion intercept c' should be assumed equal to zero in the upper layer of slope for slope stability analysis to gain a result close to reality.

5.4 Summary: Unsaturated interface behavior between smooth or textured geomembranes and clayey soil

This study was carried out to investigate the shear response and preliminary constitutive modeling of unsaturated soil-geomembrane interfaces. Interface shear tests were carried out on unsaturated soil-geomembrane interfaces. Two types of geomembranes, smooth and textured HDPE, were involved in the interface shear tests. The interface shear tests were carried out at different suction (0 kPa, 200 kPa, and 400 kPa) and net normal stress (12.5 kPa, 25 kPa, 50 kPa and 75 kPa) values. The effect of displacement rate on the interface shear strength was investigated using two values: 0.0005 and 0.005 mm/min. A series of suction-controlled direct shear tests and saturated direct shear tests were carried out on the unsaturated clayey test soil to compare with the interface results. A constitutive model was used to simulate the mechanical behavior observed in the experimental results. Comparison with the experimental results presented in this study showed that the model is overall capable of reliably capturing the responses of unsaturated soil-geomembrane interfaces. Some of the conclusions of this study and recommendations for the future works are summarized below:

5.5 Conclusions: Unsaturated interface behavior between smooth or textured geomembranes and clayey soil

1. In general, the clayey soil-textured geomembrane interface exhibited higher amounts of dilation as compared to the clayey soil-smooth geomembrane

interface. Tendency for dilation was more pronounced when the displacement rate was high.

2. In general, small decreases in water content in clayey soil-textured geomembrane and clayey soil-smooth specimens were detected during the shearing process. This behavior was attributed to the disruption of the air-water menisci between soil particles resulting in increase of pore water pressure (i.e. decrease in suction).
3. Increasing net normal stress and suction in the soil-geomembrane interface tests resulted in an increase in the interface peak shear strength. The rate of increase was linear with respect to net normal stress and suction.
4. Increase in shear strength parameters: effective adhesion intercept and interface friction angle was detected for the textured geomembrane-clayey soil when the shear rate was relatively high. The shear strength parameters for smooth geomembrane-clayey soil were not dependent on the displacement rates considered in this study.
5. Increase in suction resulted in a reduction in the compression magnitude of vertical displacement and an increase in the dilation behavior for the interfaces.
6. Increase in suction of the geomembrane-clayey soil interface tests resulted in an increase in the effective adhesion. The interface friction angle with respect to net normal stress remained essentially constant at greater suction values. The interface friction angle with respect to suction was almost constant when suction increased.

7. The shear strength of clayey soil-geomembranes was less than that of the clayey soil alone for the all tests conducted in this study. However, the effective intercept adhesion for clayey soil was less than that of the interfaces.
8. The constitutive model was able to predict the peak shear strength responses of clayey soil-geomembrane interfaces subjected to different values of suction and net normal stress. In addition, the model trends of specimen volume change behavior in the interface shear tests were in a good agreement with the experimental results.

5.6 Recommendations: Unsaturated interface behavior between smooth or textured geomembranes and clayey soil

1. Study the effect of stress path through applying the net normal stress after the suction on the interface shear and volume change behavior.
2. Apply a greater range of suctions in the interface tests to determine the linearity or non-linearity behavior of shear strength with respect to suction.
3. Use the same direct shear device for the unsaturated and saturated conditions to reduce the systematic errors and the possible uncertainties.
4. Employ the constitutive model parameters into a finite element program to develop boundary value problem solutions. For example, lateral load behavior of pile surrounded by unsaturated soil under cyclic temperature loading or seepage/slope stability analysis of slope covered by geomembrane under weather changes.

5.7 Summary: Modeling lateral load behavior of piles in unsaturated soil due to seasonal moisture content changes

Research presented in this chapter explored the impact of variable soil saturation on the lateral load behavior of integral abutment piles. In particular, the research used unsaturated seepage modelling to predict the variations in soil moisture content using climate forecasts of weather through the end of this century. To do this, a technique for calibrating the future weather predictions was developed using historical weather data. Then, the calibrated weather information was used in the unsaturated seepage modeling to predict future moisture content variations and the associated matric suction profiles surrounding abutment piles. Next, techniques were used to incorporate matric suction into the lateral load analysis of abutment piles. In this way, the impact of suction variations over time on lateral load behavior of piles was investigated. Finally, a sensitivity analysis of other parameters affecting the lateral load behavior of integral abutment piles was conducted. The following sections present some conclusions and recommendations on lateral load analysis of integral abutment piles in unsaturated soils.

5.8 Conclusions: Modeling lateral load behavior of piles in unsaturated soil due to seasonal moisture content changes

1. Historical potential evapotranspiration obtained from Thornthwaite's equation was calibrated using correction factors from each month with Penman's equation. The correction factors were varied for each month.
2. Actual evapotranspiration was modified by Leaf Area Index (LAI) for Thornthwaite method. Variations of LAI from 0.8 for first and last quarter of the

year and 2.6 for the rest of the year created reasonable calibrated results in comparison with Penman method.

3. The maximum change of suction from past to future weather changes was less than 1000 kPa for the given example of soil surrounding the pile in IAB.
4. The pile-soil interaction analysis for an IAB subjected to temperature and moisture variations indicated that the pile bending behavior during lateral loading was sensitive to suction changes of the foundation soil. The bending moment increased when the suction increased due to increase of soil stiffness.
5. The parametric study showed that the pile orientations and soil foundation stiffness have a significant effect on the bending moment and lateral displacement behavior of abutment piles.

5.9 Recommendations: Modeling lateral load behavior of piles in unsaturated soil due to seasonal moisture content changes

1. The seepage analysis was conducted on the given Integral Abutment Bridge (IAB) located in Oklahoma. The change of location to apply other weather conditions would be useful to examine the effectiveness of the proposed method for the moisture content prediction.
2. The seepage analysis is dependent on the soil properties and boundary conditions. A soil stratum from very low to low permeability or vice versa with different SWCCs can be added to the parametric study.

3. The boundary condition of abutment-pile and abutment-bridge deck can be varied from fixed, partially restrained, and free rotational and translational movements.
4. The Winkler foundation finite difference solution incorporated in L-Pile for pile-soil interaction analysis in unsaturated conditions can be compared with a continuum mechanics based solution such as found in the finite element program Code Bright, which is able to solve hydro-mechanical coupling problems.
5. A pile group analysis considering suction changes of soil surrounding a pile group using 3-D seepage analysis needs to compare with a single pile analysis conducted in this research.

References

Anubhav, and Basudhar, P. K. (2010). "Modeling of soil-woven geotextile interface behavior from direct shear test results." *Geotextiles and Geomembranes*, 28(4), 403–408.

Arsoy, S., Barker, R. M., and Duncan, J. M., (2004). "Behavior of a semi-integral bridge abutment under static and temperature-induced cyclic loading." *Journal of Bridge Engineering*, 9(2), 193–199.

Aubeny, C., and Lytton, R., (2004). "Shallow slides in compacted high plasticity clay slopes." *Journal of Geotechnical and Geoenvironmental Engineering*, 130(7), 717–727.

Ayad, R., Konrad, J. M., Soulie, M. (1997). "Desiccation of sensitive clay: application of the model CRACK." *Canadian Geotechnical Journal*, 34(6), 943–951.

Barton, N., Bandis, S., and Bakhtar, K. (1985). "Strength, deformation and conductivity coupling of rock joints." *International Journal of Rock Mechanics and Mining Sciences & Geomechanics Abstracts*, 22, 121–140.

Brinch-Hansen, J. (1961). "The ultimate resistance of rigid piles against transversal forces." *Bulletin No. 12, Geoteknisk Institut (The Danish Geotechnical Institute), Copenhagen*, 5–9.

Chertkov, V. Y., Ravina I. (1999). "Analysis of geometrical characteristics of vertical and horizontal shrinkage cracks." *Journal of Agricultural Engineering Research*, 74, 13–19.

Clough, G. W. and Duncan, J. M. (1969). "Finite element analyses of port allen and old river locks." *Report Number TE 69-3, University of California, Berkeley, California, USA*.

Corte, A., and Higashi, A. (1964). "Experimental research on desiccation cracks in soil." *CRREL-RR-66 Final Report, U.S. Army Cold Regions Research and Engineering Laboratory*.

DIT-UPC (2015). "CODE_BRIGHT." *A 3-D Program for Thermo-hydro-mechanical Analysis in Geological Media, The Department of Geotechnical Engineering and Geosciences of the Universitat Politècnica de Catalunya*.

Edwards, W.M., Van der Ploeg, R.R. and Ehlers, W. (1979). "A numerical study of the effects of non-capillary-sized pores upon infiltration." *Soil Science Society America Journal* 43, 851–856.

Detournay, E. and Cheng, A.H.-D. (1993). "Fundamentals of poroelasticity." *Comprehensive rock engineering principles, practice and projects, analysis and design methods* (Fairhurst, C. ed), Pergamon, Oxford, 113–171 (Chapter 5).

Dove, J.E., Frost, J.D., Dove, P.M. (1996). "Geomembrane microtopography by atomic force microscopy." *Geosynth. Int.*, 3 (2), 227–245.

Elias, E. A., Salih, A. A. 2, and Alaily, F. (2001). "Cracking patterns in the vertisols of the Sudan Gezira at the end of dry season." *Int. Agrophysics*, 15, 151–155

Ensoft, Inc. (2007). "LPILE Plus Version 5.0." Computer Code, Austin, TX.

Esterhuizen, J., Filz, G., and Duncan, J. (2001). "Constitutive behavior of geosynthetic interfaces." *J. Geotech. Geoenviron. Eng.*, 127(10), 834–840

Evans, L. T., and Duncan, J. M. (1982). "Simplified analysis of laterally loaded piles." Report No. UCB/GT/82-04, Geotechnical Engineering, Department of Civil Engineering, University of California, Berkeley, USA.

Filz, G.M., Esterhuizen J.J.B., and J. Michael Duncan, J.M. (2001). "Progressive failure of lined waste impoundments." *Journal of Geotechnical and Geoenvironmental Engineering*, 127(10), 841–848.

Fishman, K. L., and Pal, S. (1994). Further study of geomembrane/cohesive soil interface shear behavior. *Geotextiles and Geomembranes*, 13(9), 571–590.

Fleming, I. R., Sharma, J. S., and Jogi, M. B. (2006). "Shear strength of geomembrane–soil interface under unsaturated conditions." *Geotextiles and Geomembranes*, 24(5), 274–284.

Fredlund, D. G., Houston, S. L., Nguyen, Q., and Fredlund, M. D. (2010). "Moisture movement through cracked clay soil profiles." *Geotechnical and Geological Engineering*, 28(6), 865–888.

Fredlund, D. G. and Rahardjo, H. (1993). "*Soil Mechanics for Unsaturated Soils.*" John Wiley & Sons, New York.

Georgiadis, K. (2003). "Development, implementation and application of partially saturated soil models in finite element analysis." Ph.D. thesis, Imperial College of Science, Technology and Medicine, University of London.

Georgiadis K, Potts DM, Zdravkovic L. (2003) "The influence of partial soil saturation pile behavior." *Géotechnique*, 53, 11–25.

Gilbert, R. b., and Byrne, R. j. (1996). "Strain-softening behavior of waste containment system interfaces." *Geosynthetics International*, 3(2), 181–203.

Ghiassian, H., Hryciw, R., and Gray, D. (1997). "A circular arc test for soil-geosynthetic interface strength." *Geotechnical Testing Journal*, 20(4), 407–413,

Gomez J.E. and Filz, G.M. (1999). "Effects of consolidation on strength of the interface between a clay liner and smooth geomembrane." Proceedings of Geosynthetics '99 Conference, Boston, USA, 681–696.

Hamid, T.B. (2005). "Testing and modeling of unsaturated interfaces." *Ph.D. Dissertation*, School of Civil Engineering and Environmental Science, University of Oklahoma, Norman, Oklahoma, USA.

Hamid, T.B., and Miller, G.A., (2009), "Shear strength of unsaturated soil interfaces." *Canadian Geotechnical Journal*, 46(5), 595–606.

Hamilton, Megan. (2014). "Pile-soil interaction in unsaturated soil conditions." *Honors Theses and Capstones*, University of New Hampshire, USA.

Hoogmoed, W. B., and J. Bouma. (1980). "A simulation model for predicting infiltration into a cracked clay soil." *Soil Sci. Sac. Am. J.*, 44, 458–461.

Hu, L., and Pu, J. L. (2003). "Application of damage model for soil–structure interface." *Computers and Geotechnics*, 30(2), 165–183.

Hu, L. and Pu, J. (2004). "Testing and modeling of soil-structure interface." *J. Geotech. Geoenviron. Eng.*, 130(8), 851–860.

Irmak, S., Irmak, A., Jones, J. W., Howell, T. A., Jacobs, J. M., Allen, R. G., et al. (2003). "Predicting daily net radiation using minimum climatological data." *Journal of Irrigation and Drainage Engineering*, 129, 256–269.

Jogi, M. (2005). "A method for measuring smooth geomembrane / soil interface shear behaviour under unsaturated conditions." *M.Sc. thesis*, Department of Civil Engineering, University of Saskatchewan, Saskatoon, SK, Canada.

Kayyal, M. K., Wright, S. G. (1991). "Investigation of long-term strength properties of paris and beaumont clays in earth embankments." Research Report 1195-2F, Center for Transportation Research, The University of Texas at Austin, November.

Khandelwal, S. (2011). "Effect of desiccation cracks on earth embankments." *M.Sc. thesis*, Texas A&M University, College Station, Texas, USA.

Khoury, C. N., Miller, G. A., and Hatami, K. (2011). "Unsaturated soil–geotextile interface behavior." *Geotextiles and Geomembranes*, 29(1), 17–28.

Kirupakaran, K. (2013). "Soil-structure interaction studies for understanding the behavior of integral abutment bridges." *Ph.D. dissertation*, School of Civil Engineering and Environmental Science, University of Oklahoma, Norman, Oklahoma, USA.

Knight, M. J. (1971). "Structural analysis of selected duplex soils." Doctoral Dissertation, University of Melbourne, Melbourne, Australia.

Koerner, R. M. and Daniel, D. E. (1997). "Final Covers for Solid Waste Landfills and Abandoned Dumps.", ASCE Press, Reston, VA.

Koerner, R. M., Martin, J. P. & Koerner, G. R. (1986). "Shear strength parameters between geomembranes and cohesive soils." *Geotextiles and Geomembranes*, 4(1), 21–30.

Koerner, R. and Soong, T. (2000). "Stability Assessment of Ten Large Landfill Failures." *Advances in Transportation and Geoenvironmental Systems Using Geosynthetics*, 1–38.

Konrad, J. M., Ayad, R. (1997). "An idealized framework for the analysis of cohesive soils undergoing desiccation." *Canadian Geotechnical Journal*, 34(4), 477-488.

Koutsourais, M. M., Sprague, C. J., and Pucetas, R. C. (1991). "Interfacial friction study of cap and liner components for landfill design." *Geotextiles and Geomembranes*, 10(5), 531–548.

Leong, E. and Rahardjo, H. (1997). "Permeability functions for unsaturated soils." *J. Geotech. Geoenviron. Eng.*, 123(12), 1118–1126.

Ling, H., Pamuk, A., Dechasakulsom, M., Mohri, Y., and Burke, C. (2001). "Interactions between pvc geomembranes and compacted clays." *J. Geotech. Geoenviron. Eng.*, 127(11), 950–954.

Lu, N., Godt, J. W., and Wu, D. T. (2010). "A closed-form equation for effective stress in unsaturated soil." *Water Resources Research*, 46, 1–14.

Matlock, H. (1970). "Correlations for design of laterally loaded piles in soft clay." Proceedings of 2nd Offshore Technology Conference, Houston, Texas, 1, 577–588.

Michalowski, R. L. (2013). "Stability assessment of slopes with cracks using limit analysis." *Canadian Geotechnical Journal*, 50(10), 1011–1021.

Miller C. J., Mi H., Yesiller N., (1998). "Experimental analysis of desiccation crack propagation in clay liners." *Journal of the American water resources association*, 34(3), 677–686.

Miller, G. A., Hassanikhah, A., Varsei, M. (2015). "Desiccation crack depth and tensile strength in compacted soil." *Unsaturated Soil Mechanics–From Theory to Practice: Proc., 6th Asia Pacific Conf. on Unsaturated Soils*.

Miller, G. A., Muraleetharan, K. K., Lim, Y. Y. (2001). "Wetting-induced settlement of compacted fill embankments." *Transportation Research Board*, 1755, *Geology and Properties of Earth Materials*.

Mitchell, J., Seed, R., and Seed, H. (1990). "Kettleman hills waste landfill slope failure. i: liner-system properties." *J. Geotech. Engrg.*, 116(4), 647–668.

Moeletsi M. E., Walker S., Hamandawana H., (2013). "Comparison of the hargreaves and samani equation and the thornthwaite equation for estimating dekadal evapotranspiration in the free state province." *South Africa. Phys Chem Earth*, 66, 4–15.

Mokwa, R., Duncan, J., and Helmers, M. (2000). "Development of p-y curves for partly saturated silts and clays." *New Technological and Design Developments in Deep Foundations*, 224–239.

Monteiro C. B., Araújo G. L. S., Palmeira E. M., and Cordão Neto M. P. (2013). "Soil-geosynthetic interface strength on smooth and texturized geomembranes under different test conditions." *Proceedings of the 18th International Conference on Soil Mechanics and Geotechnical Engineering*.

Morris, P. H., Graham, J., and Williams, D. J. 1992. "Cracking in drying soils." *Canadian Geotechnical Journal*, 29, 263–277.

Muraleetharan, K. K., Miller, G. A., (2015). "Design of integral abutment bridges in extreme climate." *Highlighting Developments at Southern Plains Transportation Center (SPTC)*.

Navayogarajah, N., 1990, "Constitutive modeling of static and cyclic behavior of interfaces and implementation in boundary value problems." Ph.D. Dissertation, Department of Civil and Engineering Mechanics, University of Arizona, Tucson, USA.

Ng, C., Springman, S. and Norrish, A. (1998). "Soil-structure interaction of spread-base integral bridge abutments." *Soils and Foundations*, 38(1), 145–162.

Penman, H. L. (1948). "Natural evapotranspiration from open water, bare soil and grass." *Proc. R. Soc. London Ser. A*. 193, 120–145.

Reddy, K. R., Kosgi, S., and Motan, E. S. (1996). "Interface shear behavior of landfill composite liner systems: A Finite Element Analysis." *Geosynthetics International*, 3(2), 247–275.

Reese, L. C., Cox, W. R. and Koop, F. D. (1974). "Analysis of lateral loaded piles in sand." Offshore technical conference, Dallas, Texas.

Reese, L. C., Touma, F. T. and O'Neill, M. W. (1976). "Behavior of driven piers under axial loading." *Journal of the geotechnical engineering division, proceedings of ASCE*, 102(GT5), 493–510.

Seed, R. B., and Boulanger, R. W. (1991). "Smooth HDPE-clay liner interface shear strengths: compaction effects." *Journal of Geotechnical Engineering*, 117(4).

Seo, M. W., Park, J. B., and Park, I. J. (2007). "Evaluation of interface shear strength between geosynthetics under wet condition." *Soils and Foundations*, 47(5), 845–856.

Stirk G. (1954). "Some aspects of soil shrinkage and the effect of cracking upon water entry into the soil." *Aus. J. Agric. Res.* 5, 279–290.

Swan, R. H., Bonaparte, R., Bachus, R. C., Rivette, C. A., & Spikula, D. R. (1991). "Effect of soil compaction conditions on geomembrane-soil interface strength." *Geotextiles and Geomembranes*, 10(5), 523–529.

SoilVision Systems Ltd. (2012). "SVFlux 2D Pro." Computer Code, Saskatoon, Saskatchewan, Canada.

SoilVision Systems Ltd. (2012). "SVSlope 2D Pro." Computer Code, Saskatoon, Saskatchewan, Canada.

Terzaghi, K., and Peck, R.B., (1967). "Soil Mechanics in Engineering Practice." 2nd Edition, John Wiley and Sons, New York, USA.

Thorntwaite, C. W. (1948). "An approach toward a rational classification of climate." *Geographical Review*, 38 (1), 55–94

Uesugi, M. and Kishida, H. (1986). "Frictional resistance at yield between dry sand and mild steel." *Soils and Foundations*, 26(4), 139–149.

van-Genuchten, M. T. (1980). "Closed-form equation for predicting the hydraulic conductivity of unsaturated soils." *Soil Science Society of America Journal*, 44(5), 892–898.

Varsei, M., Miller, G., and Hassanikhah, A. (2016). "Novel approach to measuring tensile strength of compacted clayey soil during desiccation." *Int. J. Geomechanics*.

Vogel, H. J., Hoffmann, H., Roth, K. (2005a). "Studies of crack dynamics in clay soil I. Experimental methods, results, and morphological quantification." *Geoderma*, 125, 203–211.

Vogel, H. J., Hofmann, H., Leopold, A., Roth, K. (2005b). "Studies of crack dynamics in clay soil: II. A physically based model for crack formation." *Geoderma*, 125, 213–223.

Wathugala, G. W., (1990). "Finite element dynamic analysis of nonlinear porous media with applications to piles in saturated clays." *Ph.D. Dissertation*, University of Arizona, Tucson, Arizona, USA.

Wang, J. S. Y., and Narasimhan, T. N., (1985). "Hydrologic mechanisms governing fluid flow in a partially saturated, fractured, porous medium." *Water Resour. Res.*, 21(12), 1861–1874.

Wang, Z. F., Li, J. H., and Zhang, L. M., (2011), "Influence of cracks on the stability of a cracked soil slope," 5th Asia-Pacific Conference on Unsaturated Soils, 2, 594–600.

Weaver, T. and Grandi, O. (2009). "Lateral load analysis of deep foundations in unsaturated soils." *Contemporary Topics in In Situ Testing, Analysis, and Reliability of Foundations*, 552–559.

Wilson, G. W., Fredlund, D.G., and Barbour, S. L. (1994). "Coupled soil-atmosphere modeling for soil evaporation", *Canadian Geotechnical Journal*, 31, 151–161.

Wu, H., and Shu, Y. (2012). "Stability of geomembrane surface barrier of earth dam considering strain-softening characteristic of geosynthetic interface." *KSCCE Journal of Civil Engineering*, 16(7), 1123–1131.

Zapata, C. E. (1999). "Uncertainty in soil–water characteristic curve and impacts on unsaturated shear strength predictions." *Ph.D. Dissertation*, Arizona State University, Tempe, USA.

Zhang, G., Wang, R., Qian, Jiyun, Zhang, J.-M., and Qian, Jiangu. (2012). "Effect study of cracks on behavior of soil slope under rainfall conditions." *Soils and Foundations*, 52(4), 634–643.

Zhou, A., and Lu, T. (2009). "Elasto-plastic constitutive model of soil-structure interface in consideration of strain softening and dilation." *Acta Mechanica Solida Sinica*, 22(2), 171–179.

Appendix A: Crack depth estimation for Chickasha slope

A summary of soil parameters and properties used for the analytical and numerical methods is shown in Tables A.1 and A.2. Initial lateral stresses are unknown; however, since compacted cohesive soils can experience lateral stress ratios approaching unity or greater (e.g. Duncan and Seed 1986) and the Chickasha soil was stiffer than the test soil, therefore a basic value of 1.0 was selected for the analytical model. The estimated ranges were based on $\pm 25\%$ of the basic values. The analytical and numerical results of desiccation crack depth are shown in Figure A.1 (a) and (b).

Table A.1. Analytical parameters and assumptions for Chickasha soil

Parameter	Value	Determined by:
γ (kN/m ³)	20.4	measured
ν	0.26-0.44	estimated
E/H	0.23-0.38	estimated
K_o	0.75-1.25	estimated
ϕ'	29.7	measured
σ'_i (kPa)	-27	measured

Table A.2. Numerical parameters and assumptions for Chickasha soil

Parameter		Value	Determined by:
Young modulus (MPa)	E	20	measured
Poisson's ratio	ν	0.35	estimated
Swelling coefficient for changes in suction (Mpa ⁻¹)	a_s	0.005	measured
Porosity	n	0.35	measured
Intrinsic permeability (m ²)	κ	2.82e-14	measured

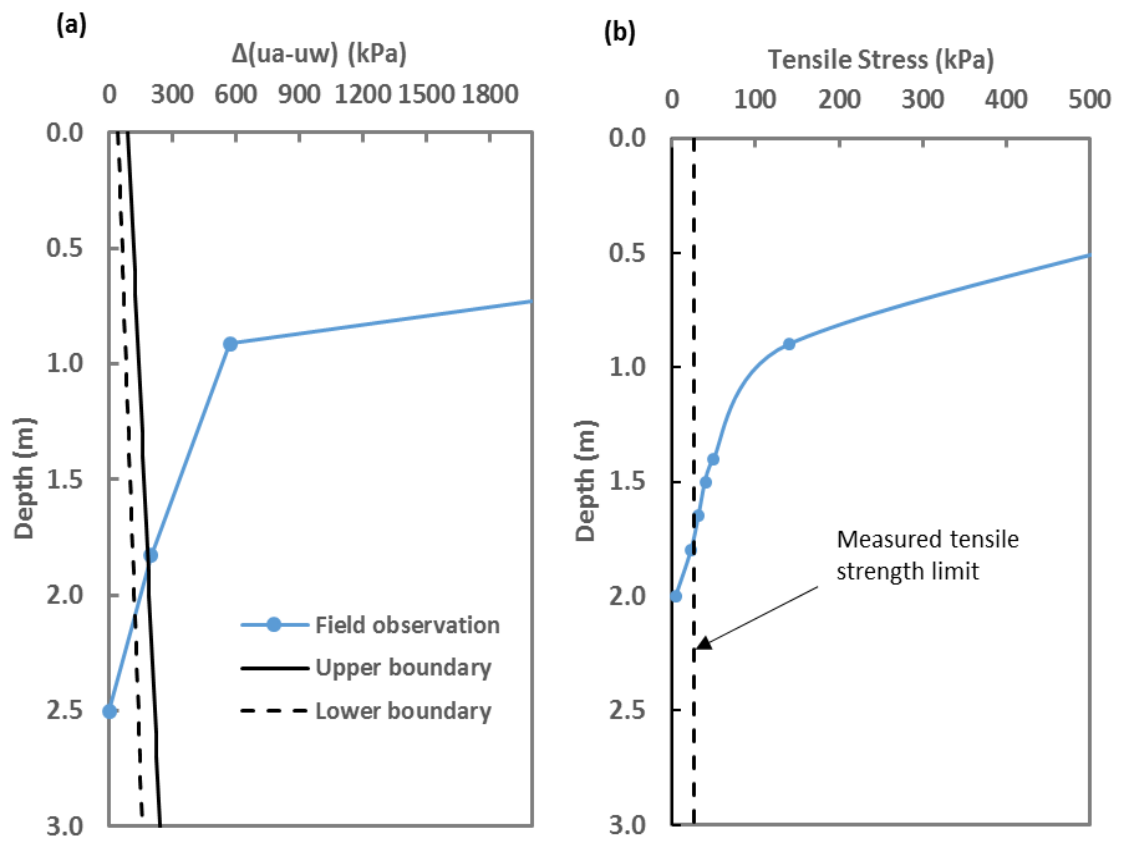


Figure A.1. (a) Analytical results (b) numerical results for desiccation crack depth